ANALYSIS AND OPTIMISATION OF SEMICONDUCTOR REFLECTIVE MODULATORS FOR OPTICAL NETWORKS

BY

ALAN NAUGHTON

A THESIS SUBMITTED TO
THE NATIONAL UNIVERSITY OF IRELAND, CORK
FOR THE DEGREE OF

DOCTOR OF PHILOSOPHY

PHOTONICS SYSTEMS GROUP
TYNDALL NATIONAL INSTITUTE, DEPARTMENT OF PHYSICS
NATIONAL UNIVERSITY OF IRELAND, CORK
IRELAND

APRIL 2014

RESEARCH SUPERVISOR: PROF. PAUL TOWNSEND
HEAD OF DEPARTMENT: PROF. JOHN MCINERNEY

TABLE OF CONTENTS

ACKNOWLEDGEMENTS

Firstly I would like to thank my supervisor Prof. Paul Townsend for giving me the opportunity to pursue my PhD and for providing me with technical guidance, advice and encouragement throughout my studies. Even during busy periods his door was always open if I needed to discuss any aspect of my work.

I would like to offer my special thanks to Dr. Giuseppe Talli who has been an invaluable source of assistance and advice on all aspects of my work. In particular the help provided with modelling and guidance during the thesis write-up. I would also like to thank Cleitus Antony, Peter Ossieur, Stefano Porto, Aisling Clarke and Caroline Lai all of whom I have spent many hours with in the lab and were always on hand to offer help or advice if required. I would like thank all the members of the Photonic Systems Group and I am also very grateful for the help provided by Martina Connolly on all administrative tasks. I would also like to acknowledge all external collaborators who I have worked with.

Over the past number of years I have made many good friends here in Tyndall. I would like to thank Stefano, Nicola and Dave G in particular for many enjoyable times both in Tyndall and on our many nights out in Cork or further afield. I would also like to thank DW, Steve, Liam, BK, Cristian, Shane, Daniel, Naoise, Mark and many more that have made my experience in Tyndall very enjoyable.

On a personal note I would like to sincerely thank my parents for the constant support, encouragement and assistance they have always provided. I would like to thank my sisters Claire and Elaine and my Grandmother “Mama” who has always believed in me. I would also like to thank Aileen for her support and encouragement, particularly during the final months of my PhD.

Finally I would like to acknowledge Science Foundation Ireland (SFI) and the European Union under the PIEMAN and C3PO projects for funding my PhD.

ABSTRACT

Reflective modulators based on the combination of an electroabsorption modulator (EAM) and semiconductor optical amplifier (SOA) are attractive devices for applications in long reach carrier distributed passive optical networks (PONs) due to the gain provided by the SOA and the high speed and low chirp modulation of the EAM. Integrated R-EAM-SOAs have experimentally shown two unexpected and unintuitive characteristics which are not observed in a single pass transmission SOA: the clamping of the output power of the device around a maximum value and low patterning distortion despite the SOA being in a regime of gain saturation.

In this thesis a detailed analysis is carried out using both experimental measurements and modelling in order to understand these phenomena. For the first time it is shown that both the internal loss between SOA and R-EAM and the SOA gain play an integral role in the behaviour of gain saturated R-EAM-SOAs. Internal loss and SOA gain are also optimised for use in a carrier distributed PONs in order to access both the positive effect of output power clamping, and hence upstream dynamic range reduction, combined with low patterning operation of the SOA

Reflective concepts are also gaining interest for metro transport networks and short reach, high bit rate, inter-datacentre links. Moving the optical carrier generation away from the transmitter also has potential advantages for these applications as it avoids the need for cooled photonics being placed directly on hot router line-cards. A detailed analysis is carried out in this thesis on a novel colourless reflective duobinary modulator, which would enable wavelength flexibility in a power-efficient reflective metro node.

STATEMENT OF ORIGINALITY

I hereby certify that I am the sole author of this thesis. Except where indicated, all the work presented in this thesis is solely attributed to the author. The author participated in the design and implementation of all experiments except where explicitly stated. Precise details of collaborators may be ascertained from the list of co-authors in the List of Publications.

I certify that, to the best of my knowledge, my thesis does not infringe upon anyone's copyright nor violate any proprietary rights and that any ideas, techniques, quotations, or any other material from the work of other people included in my thesis, published or otherwise, are fully acknowledged in accordance with the standard referencing practices.

I declare that this is a true copy of my thesis and has not been submitted for another degree to any other University or Institution.

1
INTRODUCTION

Today's world is becoming a much smaller place with each passing day due to the vast amounts of information which are available to the approximate 2.7 billion internet users around the globe [1]. This access to information and ease of communication between people in different corners of the word has changed the way both businesses and individuals operate on a daily basis. The global optical communications network has played a major part in arriving where we are today highlighting the significance of Charles Kao's discovery of low loss glass fibres [2] in 1966.

We are now experiencing a huge growth in the demand for bandwidth. This is driven by services such as YouTube [3], Netflix [4] and high definition television services for individuals and applications such as cloud computing for businesses. This increasing data traffic is putting extreme pressure on existing infrastructure and is driving the installation of optical fibres in the access network with fibre-to-the-home (FTTH) and fibre-to-the-business (FTTB) networks now emerging. Despite this access networks are still dominated by copper cable and the widespread introduction of optical fibre in access remains the final step in building all optical networks. Without the roll out of optical fibre networks very close or all the way to the users premises service providers will not be able to meet the bandwidth demands of residential and business customers.

1.1 BACKGROUND

Today's core and metro networks are dominated by optical fibre, however optical fibres have only started to be introduced in the access part of the network in recent

years. Figure 1.1 shows a high level representation of the typical network hierarchy today. Copper access networks still dominate in many parts of the world, with some fibre and wireless access also in use. If network operators are to meet the growing demand for high-bit rate, low latency services a significant optical fibre roll-out will be required in the access network.

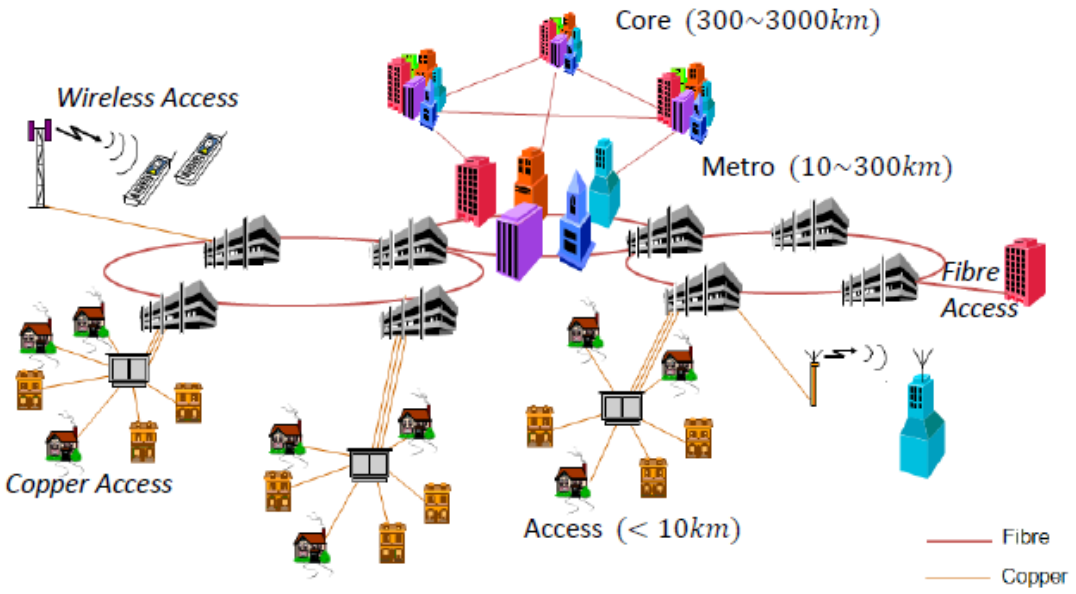

Figure 1.1. Network hierarchy today

One of the foremost questions for network operators is which fibre access solution to adopt. The passive optical network (PON) is the most widespread optical access solution currently deployed and is the most attractive for future deployments. However the state-of-the-art PONs, which are currently being deployed such as the gigabit passive optical network (G-PON) [5], might not be the ultimate solution. These PONs are already coming under pressure to meet the bandwidth demand, therefore network operators are now looking to the next generation of PONs.

One of the main reasons for the slow introduction of fibre services in the access part of the network is cost [6], [7]. The infrastructure of the access network is shared by a much smaller number of users than the metro and core networks. This

in turn means that the cost of installing, operating and maintaining the access network is also shared among a smaller number of users.

This cost sensitivity is also one of the fundamental reasons why the PON configuration is the most attractive solution for optical access networks. Because PONs use passive splitters to share bandwidth among users they have a significant cost advantage over alternative solutions [8], [9]. However next generation PONs will need to significantly increase data rates, user numbers and reach. To achieve this next generation PONs will need to evolve significantly from the PONs which are in deployment today.

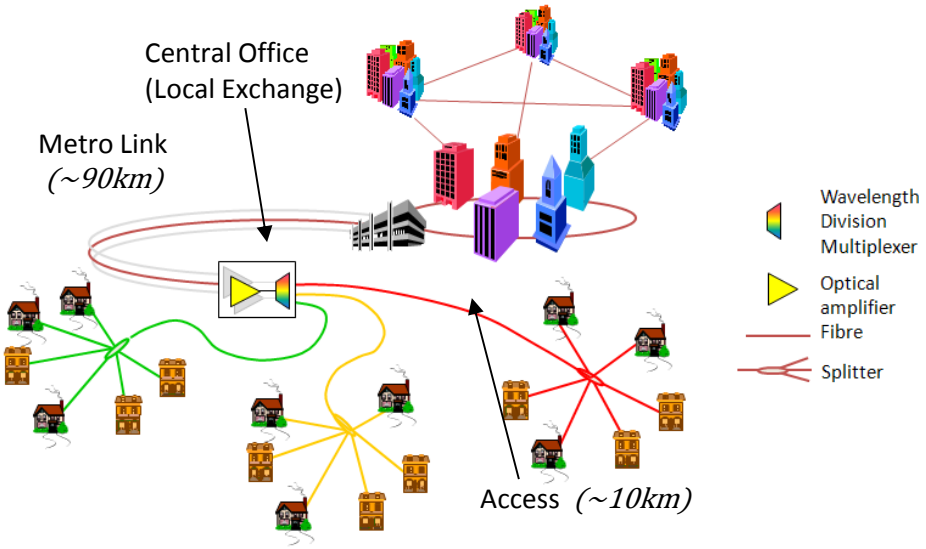

Figure 1.2. Next generation long-reach PON

Significant research interest is now aiming at optical access network concepts known as hybrid wavelength-division-multiplexed time-division multiple access passive optical networks (DWDM-TDMA PONs) [9]. These systems differ from today's PONs in three ways. Firstly, in order to dramatically increase capacity, dense WDM (DWDM) is used. Secondly, the reach is significantly increased from the maximum reach possible with today's PONs of 60km to over 100km. The combination of DWDM and long reach means that the number of users per PON will dramatically increase from the typical 32 today to many thousands. The data

rates will also be increased from the typical 2.5Gb/s downstream and 1.25Gb/s upstream in today's PONs to a symmetric 10Gb/s PON. Figure 1.2 shows a high level representation of the type of the hybrid DWDM-TDMA PON architecture proposed [10].

These new types of network potentially allow the metro and access network to be combined into one all optical network. This could significantly decrease the number of network elements, interfaces and optical/electrical/optical (O/E/O) conversations required to serve a given number of customers, thus saving on capital expenditure. This configuration also has the potential to reduce power consumption and network footprint, thus reducing operational expenditure. This network configuration does, however, come with significant challenges. One of the principal challenges arises from the introduction of DWDM into the access network. The upstream transmitter at each ONU must stay tuned to the chosen DWDM grid with an accuracy determined by the pass-band of the wavelength multiplexing device used. Because of the cost sensitivity of the access network the upstream transmitter must be able to achieve this accuracy at the lowest possible cost. The transmitter must also be capable of 10Gb/s modulation, have sufficient output power to overcome access losses and have low chirp in order to realise the intended reach.

One possibility is the use of fixed wavelength lasers and external modulators in each ONU. However network operators prefer not to keep a large stock of wavelength-specific sources as it brings additional inventory and management costs while also lacking flexibility. Instead a colourless transmitter is preferred, with the two most promising options being tuneable lasers and colourless reflective modulators. It was shown that a tuneable laser and external electroabsorption modulator can achieve the wavelength stability and required modulation characteristics [11] however it is still not known if the lasers can be produced in the required volume at a low enough cost for the access market.

An alternative approach is to move the laser source away from the ONUs to a central location higher in the network such as a service node in the metro network. This means that all wavelength management is now carried out in a controlled

environment and one laser source can serve all users on a particular PON. If all the ONUs are then equipped with colourless reflective modulators, an unmodulated carrier can be distributed to the ONUs in the network. The carrier is modulated with the upstream data and reflected back as the upstream signal. This configuration is known as carrier distributed PON [12], [13] and has the potential to be an extremely cost effective solution. The reflective transmitter which has demonstrated the most potential for use in this network configuration is the combination of a reflective electroabsorption modulator (R-EAM) and semiconductor optical amplifier (SOA) integrated together to form a single device (R-EAM-SOA) [14]. Using this device, it is possible in principle to achieve both sufficient net gain to overcome splitting loss in the network and sufficiently low-chirp modulation for 10Gb/s operation over extended distances in the order of 100km [12], [13], [15], [16].

1.2 THESIS MOTIVATION

There are, however, a number of major challenges associated with the carrier distributed PON configuration and with the use of the R-EAM-SOA in such a scheme which need to be addressed. In PONs, variations of splitter excess loss, non-uniform splitter deployment and fibre path length variations result in a differential loss (DL) between ONUs at different locations in the PON. This is a significant problem as it causes large burst-to-burst amplitude variations in the upstream signals from the different ONUs when they arrive at the upstream receiver. In a carrier distributed PON the impact of DL is multiplied due to the fact that the optical carrier also experiences the DL en-route to the ONUs. This can lead to a dynamic range at the upstream receiver which is beyond the design tolerance of current 10Gb/s burst-mode receiver (BMRx) technology.

Another issue which arises because of the DL is the variation in input carrier power to the R-EAM-SOA in the ONUs. This means that the SOA sections of the R-EAM-SOAs operate in different degrees of gain saturation depending on the ONU location. This is problematic as the gain recovery effects in a saturated SOA lead to significant distortion of the modulated signal, an effect commonly referred to as

patterning. Patterning effects need to be minimised as they can severely degrade the signal.

Integrated R-EAM-SOAs have experimentally shown two unexpected and unintuitive characteristics [12], which are not observed in a single pass transmission SOA. The first was the clamping of the output power of the device around a maximum value after which an increase in input carrier power produced no further increase in output power. The second unexpected result was that the device, despite clearly working in a regime of SOA gain saturation, showed no degradation of the performance due to patterning distortions. This behaviour was attributed to excess loss at the interface between the SOA and R-EAM sections.

However a detailed analysis is necessary in order to understand these phenomena. Both the internal loss between SOA and EAM and the SOA gain play an integral role in the behaviour of gain saturated R-EAM-SOAs [17], [18]. Internal loss and SOA gain can also be optimised for use in a carrier distributed PONs in order to be able to access both the positive effect of output power clamping, and hence upstream dynamic range reduction, combined with low patterning operation of the SOA.

The reflective architectures discussed are not confined to applications in WDM-PONs and recently European research project C3PO [19] has proposed extending the reflective concept outside WDM-PON into metro transport networks and short-reach, high bit rate, inter-datacentre links. Moving the optical carrier generation away from the transmitter also has potential advantages for these applications as it avoids the need for cooled photonics being placed directly on hot router line cards, while still maintaining wavelength flexibility by using power-efficient colourless reflective modulators [20], [21].

1.3 THESIS OVERVIEW

Chapter 2 introduces the passive optical network (PON) which is the corner stone of the work carried out in this thesis. The current PON configurations are reviewed before moving onto a number of proposed next generation PON architectures, where particular attention is devoted to long reach carrier distributed PONs which

are the configuration of most interest in this thesis. Chapter 2 also outlines various fibre optic system components and their performance.

Chapter 3 presents the background theory and operational principles behind the three key semiconductor devices which are studied in this thesis. The SOA, R-EAM and integrated R-EAM-SOA.

Chapter 4 presents a study carried out on the behaviour of reflective modulators based on R-EAM-SOAs. Experimental results are presented from both an integrated R-EAM-SOA and an R-EAM-SOA, which was emulated using discrete components. Then using both a simple analytical model and an accurate numerical model the output power clamping around a maximum value and also the patterning suppression effect are analysed and explained in detail. For the first time it is demonstrated that, counterintuitively, a high value of internal loss and a high gain SOA allow utilisation of these devices in the region where the output power is clamped around a maximum value for input carrier powers compatible with those present in carrier distributed optical access networks, while also mitigating patterning distortions. The noise reduction on the input carrier due to the noise squeezing in the SOA section is also studied and it is shown that using a correctly designed R-EAM-SOA the noise reduction effect is accessible without patterning distortion.

Chapter 5 concentrates on the optimisation of gain and internal loss of the R-EAM-SOA in a carrier distributed passive optical network (PON). The experimental analysis of the R-EAM-SOA was limited to devices which had fixed gain, therefore only changes to the loss could be studied. The numerical model validated in Chapter 4 is thus used to model R-EAM-SOA devices which have different gain SOA sections, while also adjusting the internal loss. A novel solution for minimising the dynamic range of the upstream signal in a carrier distributed PON is then demonstrated. It is shown that careful design of both the SOA gain and internal loss can provide an optimum balance between dynamic range compression, output power and patterning distortion reduction.

Chapter 6 moves the focus from reflective configurations for PON applications to a proposed reflective architecture for metro nodes. In this Chapter the motivation for moving towards a reflective solution in metro networks is first briefly discussed, followed by a description of the reflective metro node architecture. A detailed analysis is then carried out on the novel reflective modulator which is intended to operate as the transmitter in the metro node. Due to the high bit rate and long reach, which are present in metro node applications, NRZ modulation is not suitable. Therefore the reflective modulator is designed to generate duobinary modulation. Duobinary modulation is chosen due to its improved dispersion tolerance compared to NRZ while still maintaining the use of a simple and low cost direct detection receiver. To the best of our knowledge, the first demonstration of error-free 25Gb/s duobinary transmission using a reflective modulator is presented in this Chapter.

Chapter 7 concludes the thesis with a summary of the important achievements and some suggestions for future investigations.

2

PASSIVE OPTICAL NETWORKS, SYSTEM COMPONENTS AND PERFORMANCE

The access part of an optical telecommunications network denotes all parts of the network from the local exchange (LE) or central office to a customer or business premises. Access networks can be divided into three main categories: wireless, copper and fibre. Wireless access technology, such as WiMAX, is low cost and relatively simple to deploy however it has relatively low bandwidth (max ~1Gb/s at minimum reach) which will be insufficient to meet future growth in demand. Copper access networks are still dominant in most parts of the world with technologies such as digital subscriber line (DSL), asymmetric digital subscriber line (ADSL) and very high speed digital subscriber line (VDSL) enabling efficient use of the available transmission bandwidth offered by co-axial or twisted pair copper cables. However with demand for high bit rate services such as high definition (HD) television, cloud computing and voice-over-IP (VOIP) etc increasing, the bandwidth and/or physical reach of copper wires and wireless solutions are approaching their limitations due to physical media constraints. This is driving network operators to consider optical fibre access networks (or optical access networks) in an attempt to meet the growing demands from both business and private customers.

Figure 2.1 shows a plot of the regeneration free transmission distance versus data rate for a number of communication technologies. The regeneration free transmission distance is defined as the distance that can be bridged without detecting and retransmitting the digital information anywhere along the propagation path. Starting on the left of Figure 2.1 the limited data-rate and

transmission distance possible with mobile wireless and wireless LAN can be seen, wireless LAN is particularly limited in reach and is realistically only suitable within buildings or small campuses. Copper solutions of twisted pair and co-axial cable can offer a considerable improvement in either reach or data rates, however there is a considerable trade-off required with data-rates decreasing rapidly with increased transmission distance. Fixed wireless (or WIMAX) follows a similar trend to the copper solution, however it does offer an improvement in reach at similar data-rates. Satellite links offer a drastic increase in reach but the maximum data-rates are relatively low. Finally we look at optical fibre. The significant difference in the combination of transmission distance and achievable data-rates can be clearly seen. The achievable data-rates considerably exceed those possible with all other technologies while there is only a small trade-off required between transmission distance and data-rate.

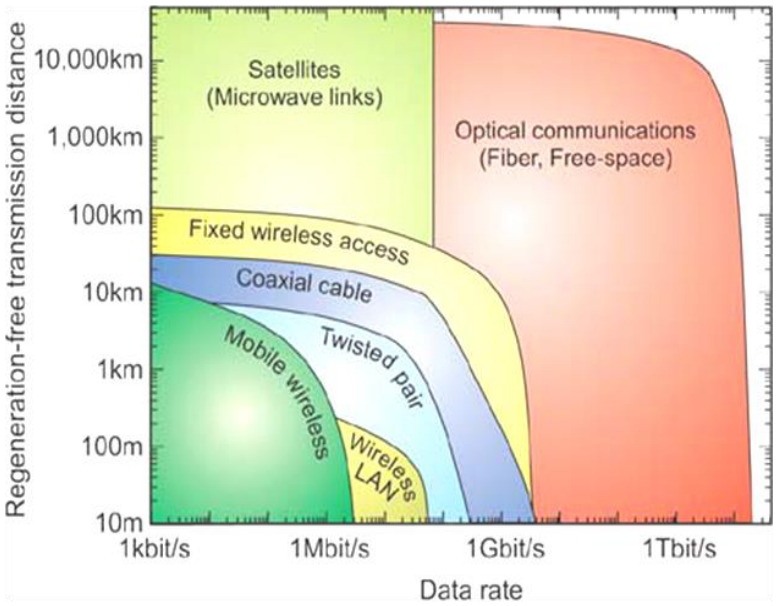

Figure 2.1. Regeneration-free transmission distance versus data rate for communication technologies [22].

2.1 OPTICAL ACCESS NETWORKS

Despite the metro and core networks being dominated by optical fibres, it is only in recent years that fibre has begun to move into the access part of the network. The

reduction in optical component costs due to the widespread use of optical technologies in the metro and core network have made the transition from copper based access networks to fibre access networks more appealing for operators. Both capital and operation costs are extremely important as the access part of the network is the most cost sensitive due to the component and infrastructure costs being shared by a much smaller number of users compared to the metro and core networks. There are a number of different levels of fibre deployment in the access network which refer to how far the optical fibre reaches: fibre-to-the-curb (FTTC), fibre-to-the-building (FTTB), and fibre-to-the-home (FTTH) are the most common. The term FTTx (where "x" depends on the fibre transmission point) is also used when speaking in general about fibre deployment in the access network.

There are also a number of options available to network operators for their FTTx network deployment strategy. The three main solutions are passive optical networks (PONs), active Ethernet (AE) and point-to-point Ethernet (P2P). There are a number of technical and economic reasons for network operators to consider before choosing the appropriate technology. Figure 2.2 shows a simple schematic diagram of the three solutions.

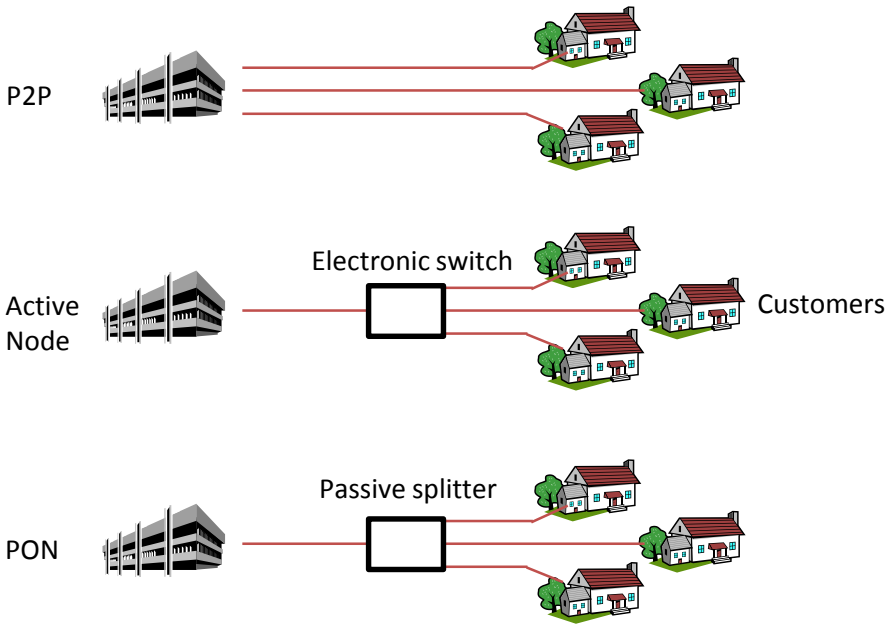

Figure 2.2. Different FTTx deployment options

The P2P solution uses Ethernet switching and aggregation, however all Ethernet switches are located in the local exchange (LE) and each customer requires a dedicated optical fibre from the LE to their premises. This has the advantage of being able to deliver high bandwidth to customers however it is expensive to deploy and operate. The AE is a point to multipoint approach which moves the Ethernet switches to a remote location closer to the customer premises, thus meaning a single fibre can run from the LE to the remote cabinet for all customers, then after the cabinet a dedicated fibre is required for each customer. While this reduces the fibre requirements it adds the need for a hardened cabinet and remote power supply to power the Ethernet switches.

The use of a PON configuration in optical access networks is very attractive due to its many advantages over the other optical access configurations. One of the main benefits of a PON is cost. The use of low cost passive splitters in the optical distribution network (ODN) and the use of a single fibre to the passive splitter reduce investment costs while the low maintenance and lack of powered network elements reduce operating costs. PONs also offer greater flexibility and scalability compared with alternative optical access network configurations.

PONs have a similar layout to the AE approach and again use a point to multipoint approach except the electronic switch at the remote location is replaced with a passive splitter. This provides bandwidth aggregation but requires less maintenance and does not have any power requirements like the active elements in AE. PONs account for the majority of currently deployed optical access networks and in this thesis are the optical access network solution of most interest. Therefore PONs will be discussed in detail in the following sections.

2.1.1 Passive Optical Networks

Figure 2.3 shows a simple block diagram of a typical PON architecture. A PON uses a point-to-multipoint network configuration which starts at the optical line termination (OLT) located in the LE. Each OLT is connected to multiple optical network units (ONUs) via the ODN. The OLT controls the flow of data traffic in the downstream and upstream directions. Sharing of the capacity among all users in the PON is done by time division multiplexing (TDM). In the downstream the OLT takes

voice, data and video from the metro network and delivers it to all ONUs in the PON. In the upstream direction the OLT receives the data traffic from all ONUs in the PON and distributes it to the metro network. In a PON configuration downstream and upstream traffic use separate wavelengths.

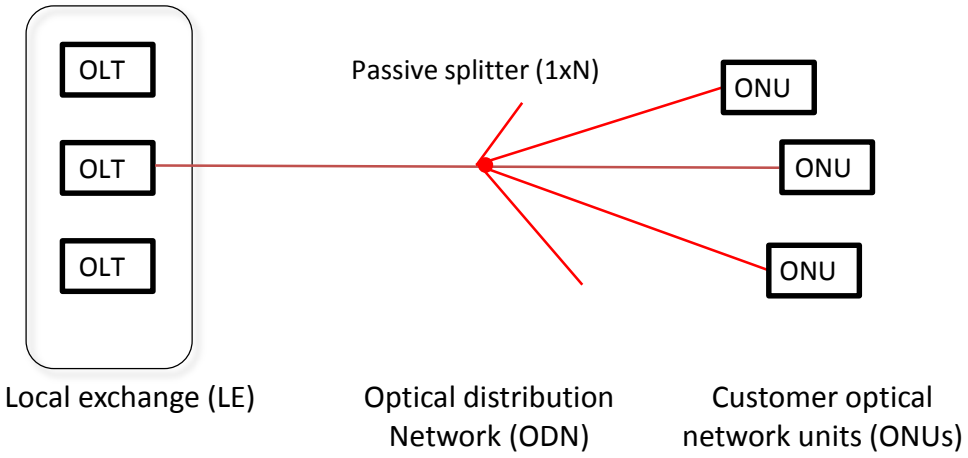

Figure 2.3. Block diagram of basic PON configuration.

The ONU is placed at the customer premises in a FTTH scenario or at intermediate location close to the customer's premises if an alternative FTTx solution is being employed (FTTC, FTTB etc). Of these options FTTH is the ultimate solution for delivering the highest bandwidths to the customer. The ONU acts as the interface between the end user and the PON. The ONU must contain an optical receiver to convert the downstream optical signals from the PON to electrical signals for the user's equipment. It must also do the reverse and convert electrical signals into optical signals so that the user can send data in the upstream direction. The ODN is the link between the OLT and ONU and consists of distribution fibres and passive splitters [23]. The splitter divides the downstream signals among all ONUs in the PON and also multiplexes the upstream signals from all the ONUs travelling to the OLT. As can be seen in Figure 2.3 the passive splitter means that only a single fibre is required between the OLT and passive splitter for all ONUs in the PON, then from the splitter each ONU has its own dedicated fibre.

In the downstream direction a basic PON operates in a broadcast mode with optical traffic from the OLT being split among all users in the PON. However in the upstream direction data traffic from different ONUs is multiplexed so that a single fibre can be shared enroute to the OLT. In the OLT the same upstream receiver is also shared by all ONUs, therefore a PON is essentially a multipoint-to-point network in the upstream direction. If upstream data packets are sent randomly from different ONUs there is a danger of packets colliding and information being lost. Therefore the PON must employ a specific type of TDM known as time division multiple access (TDMA) in the upstream direction. Using TDMA the upstream data from different ONUs is sent in a different time interval. This means that at any given time only one ONU is transmitting data and therefore no collisions can occur.

Another challenge faced by the upstream section of a PON is the variation of ODN loss which can occur between the LE and different ONUs. This loss is known as the differential loss. The differential loss comes about from variations in upstream transmitter output power, variations in path length between the splitter and different ONUs, variations in splitter excess loss and non-uniform splitter deployment. PON specifications allow this loss to be as much as 15dB [5]. This differential loss in combination with the burst nature of the upstream signal, due to the use of TDMA, results in large amplitude variations in data packets from different ONUs. Therefore the upstream receiver must be able to handle a wide dynamic range and for this reason burst mode receivers (BMRxs) must be employed.

A number of PON configurations have now been standardised and are commercially available and being deployed around the world. The most advanced PONs currently in widespread deployment are the ITU-T standardised gigabit passive optical network (G-PON) [5] and the IEEE standardised gigabit Ethernet passive optical network (GE-PON) [24]. The most advanced configurations currently standardised are the ITU-T standardised XG-PON [25] and the IEEE standardised 10G-EPON [26]. Both the ITU-T and the IEEE standardised networks offer similar configurations therefore for simplicity only the ITU-T configurations will be discussed in detail.

G-PON:

Table 2.1 lists the main features of G-PON. The G-PON network [5] is designed in the same way as the earlier B-PON [27] offering a number of FFTx solutions (FTTC, FTTB, and FTTH). The typical bit rates supported by G-PON are 2.4Gb/s downstream and 1.2Gb/s upstream, the standards also define a symmetrical 2.4Gb/s scheme and a number of lower upstream bit rates. G-PON operates in two separate wavelength regions with downstream operating in the "S-band" while upstream uses the "O-band". G-PON can have split ratios from 1:16 to 1:64, with a typical G-PON using a 1:32 split and therefore serving 32 customers. The maximum reach for a standard G-PON is 20km and the typical reach is 10km there is, however, a trade-off required between split ratio and transmission distance due to the maximum allowable ODN losses which can be supported. G-PON also has had an updated standard which allows a reach of up to 60km, which involves the addition of either optical amplification or optical/electronic/optical (O/E/O) regeneration at an intermediate location between the OLT and passive splitter. There are three ODN loss ranges defined for G-PON, Class A, B and C.

Features	G-PON
Standard	ITU-T G.984.x
Transmission rate	Downstream: 1244, 2488Mb/s Upstream: 155, 622, 1244, 2488Mb/s
Operating wavelengths:	Downstream: 1480-1500nm Upstream: 1260-1360nm Video: 1550-1560nm
Maximum number of splits	64
Maximum reach	Standard: 20km Extended: 60km
ODN loss range	Class A: 5-20dB Class B: 10-25dB Class C: 15-30dB
Transmission structure	Symmetric or asymmetric

Table 2.1. G-PON features.

Table 2.1 shows the range of losses specified for G-PON. Class C G-PON is the most attractive as its high range of allowed ODN loss allows the best combination of high splits (therefore maximising customers per PON) while also maximising reach. G-PON allows for a maximum differential ODN loss of 15dB and specifies that the upstream BMRx must be able to handle a dynamic range of approximately 20dB [5]. However despite the advantages of G-PON, bandwidth demand is quickly exceeding that which G-PON can meet and therefore a more advanced configuration has been standardised which offers even better performance than G-PON.

XG-PON:

The XG-PON standard was introduced due to the increasing demand for bandwidth, particularly in the downstream direction. XG-PON is essentially an upgrade of G-PON bringing data rates up to 10Gb/s downstream and maintaining 2.5Gb/s upstream. XG-PON is designed to co-exist with G-PON.

Features	**XG-PON**
Standard	ITU-T G.987
Transmission rate	Downstream: 10Gb/s Upstream: 2.5Gb/s
Operating wavelengths:	Downstream: 1575-1581nm Upstream: 1260-1280nm Video: 1550-1560nm
Maximum number of splits	64
Maximum reach	Standard: 20km Extended: 60km
ODN loss range	N1 class: 14-29dB N2 class: 16-31dB E1 class: 18-31dB E2 class: 20-35dB
Transmission structure	Asymmetric

Table 2.2. XG-PON features.

Table 2.2 lists the main features of XG-PON. XG-PON retains the same upstream wavelength range as G-PON in the "O-band", although the range is reduced while the downstream uses a separate range of wavelengths moving to longer wavelengths in the "L-band". There is also a slight change in the ODN loss ranges for XG-PON. The split and reach specifications remain the same as those set by G-PON.

2.2 WDM–PON

The PON configurations outlined above have operated on the basis of sharing a single wavelength among all users on that particular PON. Another possibility is the use of wavelength division multiplexing (WDM) in PONs. In a pure WDM-PON there is an OLT for each ONU in the PON and each ONU has its own dedicated wavelength. Figure 2.4 shows a basic layout of a WDM-PON. In the downstream direction each OLT transmits data at a different wavelength. The signals from all OLTs are then multiplexed using a wavelength multiplexing device such as an arrayed waveguide grating (AWG) and the multiplexed signals are launched into the ODN. In the ODN the passive splitter used in a standard PON is replaced with a second AWG which de-multiplexes the separate wavelengths which then travel to their designated ONU. In the upstream direction a second set of wavelengths are used, again each ONU has its own wavelength. All wavelengths from the different ONUs are multiplexed using an AWG and sent upstream to the local exchange where the AWG de-multiplexes the different wavelengths.

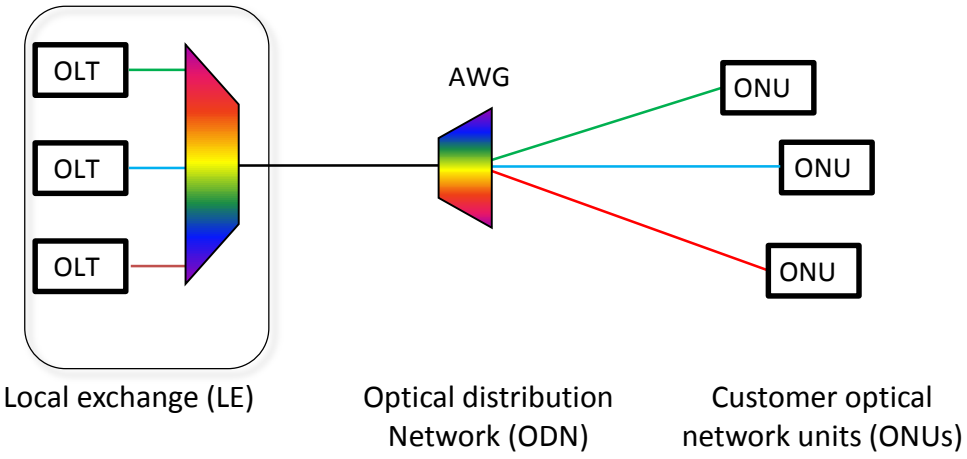

Figure 2.4. Block diagram of basic WDM-PON configuration (downstream section).

A WDM-PON allows much greater bandwidth per customer than that available in a TDM-PON as each customer has their own dedicated wavelength and due to the lower insertion loss possible with an AWG they also allow a higher number of users. However, one major disadvantage of WDM-PON is that the OLT equipment is no longer shared by a large number of customers as each customer requires their own OLT at the LE this significantly increases costs.

CWDM and DWDM:

There are two major wavelength options for WDM-PON, coarse WDM (CWDM-PON) and dense WDM (DWDM-PON). Typically CWDM [28] has a wavelength spacing of 20nm or more meaning systems can only use a limited number of channels (normally four or eight channels). The nominal wavelength range is from 1310nm to 1610nm. The wide wavelength spacing means components are cheaper due to more relaxed specifications and cross talk between adjacent channels is low. However the wide wavelength spacing severely limits the number of channels therefore CWDM lacks scalability, also due to the use of short wavelengths the transmission distances are limited by the loss [29].

DWDM [30] is a more attractive solution for the development of WDM-PONs. A typical DWDM wavelength plan has channel spacing of 0.8nm (100GHz), but narrower spacings of 12.5GHz, 25GHz and 50GHz are also possible. This makes much more efficient use of the available bandwidth by allowing a large number of channels in a narrow wavelength range [29] and can therefore provide high bandwidth to a much larger number of users than is possible with CWDM. The reference frequency for DWDM has been fixed at 193.10THz (1552.5nm) [30] and all other optical channel frequencies refer to this reference. The narrow channel spacing also means that a large number of channels can be packed into the limited spectral region where Erbium doped fibre amplifiers (EDFAs) can be used thus allowing simultaneous amplification of all channels with one amplifier. The very narrow channel spacing with DWDM does, however, mean that components such as the optical source must stay tuned to a specific wavelength in order to avoid cross talk issues with neighbouring channels.

2.3 NEXT GENERATION OPTICAL ACCESS NETWORKS

While the PONs discussed in the previous section offer significant bandwidth increases compared to copper-based approaches, they may not provide the ultimate solution for service providers seeking to significantly reduce the cost of delivering future broadband services to private or business customers. The full service access networks group (FSAN) has been investigating the options for the next generation of PONs with the next set of standards known as NG-PON2 now being discussed and nearing publication.

NG-PON2 is the most likely candidate to supersede XG-PON. One of the key challenges of NG-PON2 is to provide a significant increase in the downstream bandwidth while allowing co-existence with legacy G-PON and XG-PON systems on the same ODN. The targeted bit rates for NG-PON2 are 40Gb/s in the downstream direction and 10Gb/s in the upstream direction. In order to achieve this at low cost and maintain compatibility with legacy systems a hybrid version of WDM-PON and TDMA-PON is the chosen configuration. NG-PON2 uses the name TWDM-PON for this configuration.

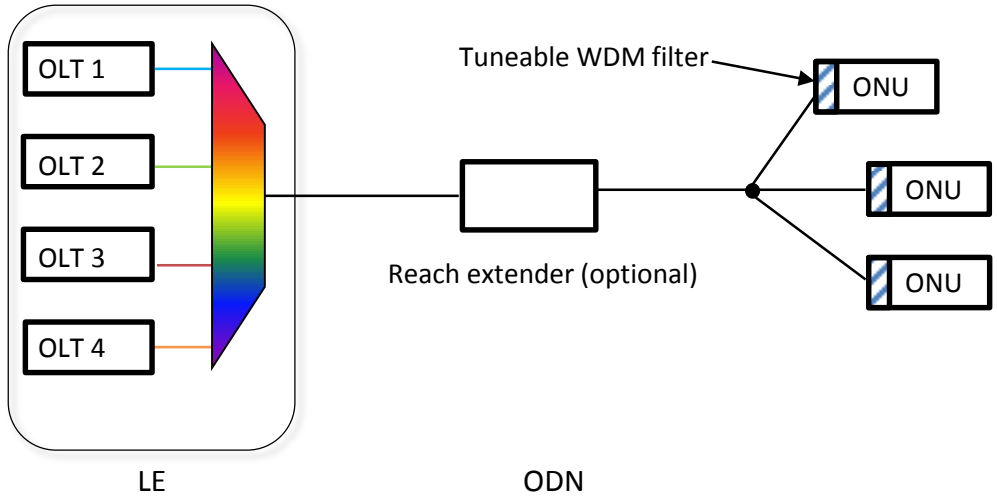

Figure 2.5. Simplified NG-PON2 architecture (downstream section).

In this architecture there are four wavelengths pairs, four wavelengths for downstream and four for upstream. Each downstream wavelength will carry data at

10Gb/s while each upstream wavelength will carry data at 2.5Gb/s. This will give an aggregated rate of 40Gb/s in the downstream and 10Gb/s in the upstream thus achieving the targeted bit rates whilst retaining the relatively low cost electronic components developed for XG-PON. For the downstream wavelengths a 100GHz based DWDM grid is defined from 1596.34nm to 1603nm, while the upstream has a DWDM grid from 1524nm to 1544nm with channel spacing between 50GHz and 100GHz allowed. A C-band wavelength plan was chosen for the NG-PON2 upstream in order to take advantage of the readily available DWDM optical components at these wavelengths such as DWDM multiplexers. To enable interoperability it also avoids the wavelength range already in use by G-PON and XG-PON.

A simple schematic of the NG-PON2 architecture is shown in Figure 2.5. The four downstream wavelengths are multiplexed and launched into the ODN where the multiplexed signal is passively split to all ONUs in the PON. At each ONU a tuneable filter can then select the wavelength of choice. In the upstream direction a tuneable DFB laser is the most likely solution for the ONU transmitter.

Features	**NG-PON2**
Standard	Not yet standardised
Transmission rate	Downstream: 40Gb/s (aggregate) Upstream: 10Gb/s (aggregate)
Operating wavelengths:	Downstream: 1596-1603nm Upstream: 1524-1544nm Video: 1550-1560nm
Maximum number of splits	64
Maximum reach	Standard: 20km Extended: 60km
ODN loss range	N1 class: 14-29dB N2 class: 16-31dB E1 class: 18-33dB E2 class: 20-35dB
Transmission structure	Asymmetric

Table 2.3. Probable NG-PON2 features.

The upstream path will use TDMA in order to prevent collisions between data packets from different ONUs. The ability of the upstream transmitter to lock on to the correct wavelength and remain stable is, however, one of the major challenges faced in realising this type of network configuration and will be discussed later in this section. As with G-PON and XG-PON the preliminary information on NGPON2 also indicates that there is provision for an extend reach configuration as shown in Figure 2.5. This will enable an increase in reach from the OLT to ONU from 20km to 60km. Further reach extension to distances greater than 60km are unlikely to be provided for under the NG-PON2 standards. The ODN loss budgets are similar to XG-PON and are outlined in Table 2.3, the maximum differential loss of 15dB is again maintained for NG-PON2.

The proposed NG-PON2 configuration will offer a significant advance on G-PON and XG-PON, however it will still be an incremental upgrade of the previous standards. Recently there has been much research attention on more radical changes to the PON architectures [31], [32], [10] than being proposed in NG-PON2. These would involve a more extensive re-organisation of the architectures which have been described in previous sections and the addition of new components and concepts.

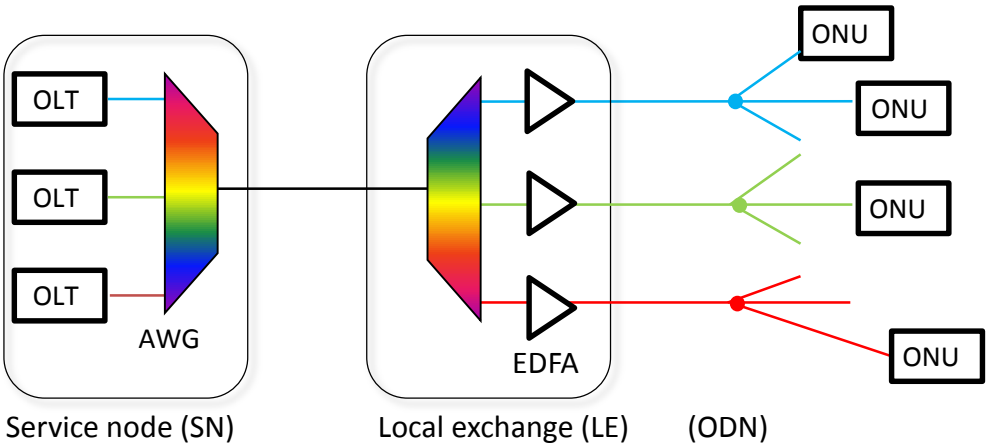

Figure 2.6. Long reach DWDM PON architecture.

One of the main changes proposed in these configurations is moving of the OLT equipment from the LE to a location at a higher level in the network known as the service node (SN) which is part of today's metro network. This long reach integrated

metro and access network [33] would require a significant increase in distance between the OLT and ONUs, with transmission distances between the SN and ONU of the order of 100km anticipated for these schemes [34]. Extending the reach to distances of 100km or more would also enable considerable node consolidation, where a small number of core nodes would handle many thousands of customers. Simplifying the network in this way has the potential to offer significant cost savings in both capital and operational expenditure.

Similar to extended reach G-PON [35] the increase in transmission distance means that amplification is required between the OLT and ONU. This equipment would be housed at the LE. As it is highly desirable to maintain an all-optical network, optical amplifiers are the preferred solution and O/E/O repeaters are not considered. The move toward the C-band and L-band, especially in the forthcoming NG-PON2 standards is very advantageous as it means working in the low attenuation region of the optical fibre and also in the region where EDFAs can be used for amplification. EDFAs are the preferred choice to act as the LE amplifiers due to their low noise figure, high gain, high saturation power and ability to amplify multiple DWDM channels simultaneously.

A dramatic increase in the number of users per PON is also highly desirable and one of the most attractive ways of doing this is through a hybrid scheme combining DWDM and TDMA and known as DWDM-TDMA PON [31], [32], [10], this is similar to the TWDM-PON configuration discussed previously. Figure 2.6 shows a block diagram of the downstream section of a hybrid DWDM-TDMA PON. At the OLT each wavelength channel has its own dedicated OLT which generates 10Gb/s data, the wavelengths from the OLTs are multiplexed and send along the backhaul fibre similar to NG-PON2. However, unlike NG-PON2 these schemes propose to utilise a large number of wavelengths (e.g. 32 wavelength pairs). Each downstream wavelength would serve its own individual PON, while all users on a particular PON would also use a single allocated wavelength for upstream transmission.

At the LE an EDFA pre-amplifies the multiplexed downstream signal before an AWG de-multiplexes out the separate wavelengths for each PON. This differs from NG-PON2 in that the wavelength selective element for the downstream is placed at the

LE rather than the ONU. In contrast to pure WDM-PON where each wavelength only supports one customer, the hybrid scheme incorporates passive splitters for each wavelength therefore the wavelength channel can be shared by multiple users. To overcome the loss introduced by the splitters and AWG each wavelength is amplified by an EDFA before launching into the ODN. This hybrid scheme has the potential to serve many thousands of customers compared to the typical 32 customers served by todays PONs [11], [13].

2.3.1 Upstream Transmitter

Similar to other PON configurations the downstream section is relatively straightforward to design. However the introduction of DWDM into the access network comes with significant challenges for the upstream transmitter in the ONU. The upstream transmitter must stay tuned to the chosen DWDM grid with an accuracy determined by the pass-band of the wavelength multiplexing device used and this must be achieved at the lowest possible cost. For this reason network operators do not want to keep a large stock of wavelength specific lasers as this brings additional inventory and management costs. Therefore a colourless transmitter is the preferred choice [29], [36].

A number of different solutions have been proposed for colourless transmitters such as spectrum sliced LEDs [37], [38] and spectrum sliced amplified spontaneous emission (ASE) seeded reflective semiconductor optical amplifiers (RSOAs) [39], [40]. However these solutions usually do not have sufficient bandwidths to support the 10Gb/s bit rates over extended distances which are required in the network configuration of interest. Another option is spectrum-sliced ASE injection-locked Fabry-Perot laser diodes (FP-LDs) [41], [42] and wavelength reuse with injection-locked FP-LDs [43]. The directly modulated injection locked FP-LDs are unsuitable for the targeted transmission distances (approximately 100km) due to their chirp characteristics. The spectrum slicing techniques are also limited in terms of optical budget which limits transmission distances and the number of possible splits and therefore the number of customers.

One solution which meets the required output power and bandwidth requirements is the use of a tuneable laser and external electroabsorption modulator (EAM). It

was shown in [11] that a low cost tuneable laser and integrated EAM-SOA could support the required transmission distances and bit rates however there are still open questions on the low cost volume production of such devices.

2.3.2 Carrier–Distributed PON

Despite the possibility of low-cost tuneable lasers being available, another scheme has been proposed which could offer even greater cost saving while also removing the need for wavelength control from the ONUs. This is done by distributing the upstream carrier from a central location and using colourless reflective transmitters in the ONU to modulate the carrier with the upstream data before reflecting it back as the upstream signal [34], [44], [12], [45], [15]. This approach is known as carrier distributed PON.

Figure 2.7 shows the basic architecture of a carrier distributed PON. In this scheme the upstream carrier is distributed from a centrally located DWDM source to colourless reflective modulators placed at the customer ONUs. This dramatically reduces the number of laser sources required as now one laser source provides the upstream carrier for all ONUs on a particular PON. The customer modulator with the most potential for use in this type of scheme is based on a semiconductor optical amplifier (SOA) and a reflective electroabsorption modulator (R-EAM) integrated together in a single monolithic device [14].

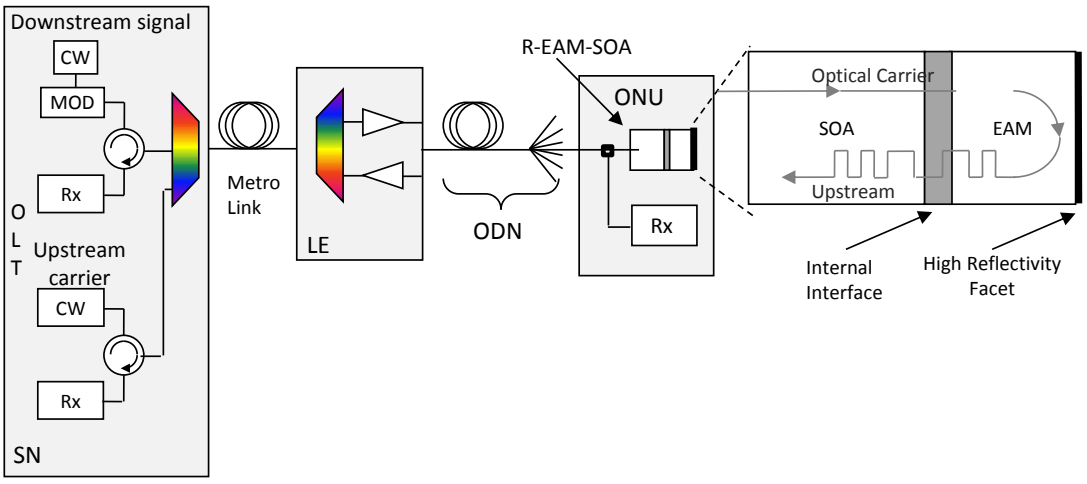

Figure 2.7. Carrier distributed PON using R-EAM-SOA as the upstream transmitter.

The upstream carrier travels together with the downstream signal to the ONU where it can be separated using a CWDM diplexer if the upstream and downstream wavelengths are on different sides of the C-band (red/blue) [11], [13]. The downstream signal is then detected while the upstream carrier is amplified by the SOA. The amplified carrier is then modulated with the upstream signal in the EAM section before being reflected, amplified again and travelling back to the LE as the upstream signal. This process is shown in the block diagram to the right of Figure 2.7. It has been demonstrated that, in principle, the R-EAM-SOA can achieve both sufficient net gain to overcome splitting loss in the network and sufficiently low chirp modulation for 10Gb/s operation over extended distances in the order of 100km [13], [12], [15], [46].

Two of the major problems associated with the use of the R-EAM-SOA as the upstream transmitter in a long reach carrier distributed PON are the large burst to burst dynamic range in the upstream signal and gain recovery effects in the SOA section of the device. Both problems arise from the differential access loss which was outlined in Section 2.1.1. In a Class C GPON, for example, the standardised value of differential loss is 15dB, with 15dB minimum and 30dB maximum ODN loss as shown in Figure 2.8. If we now consider a scenario in which a deployed Class C G-PON is being upgraded to a carrier-distributed hybrid DWDM-TDMA PON, the impact of DL is multiplied due to the fact that the optical carrier also experiences the DL en-route to the ONUs. If variations in modulator gain and input/output coupling losses are included, this implies a total dynamic range at the input of the upstream receiver which could be beyond 30dB.

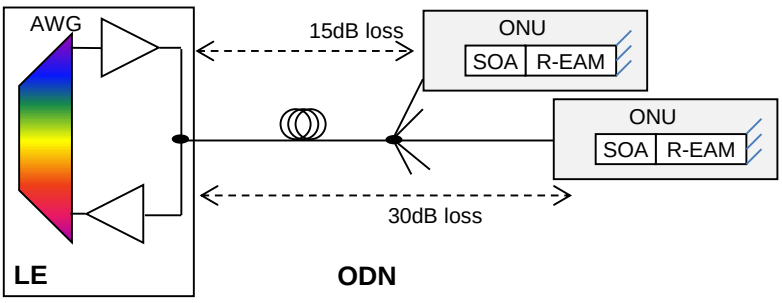

Figure 2.8. Access section of a carrier distributed PON.

This is beyond the design tolerance of current 10Gb/s BMRx technology. The large variation of ONU input power due to the DL experienced by the carrier is also of concern, since it will typically lead to the SOA sections in different ONUs operating with different degrees of gain saturation. This is an issue as the gain recovery effects in a saturated SOA lead to significant distortion of the modulated signal, an effect commonly referred to as patterning. Patterning effects must be minimised as they can severely degrade the signal.

2.4 FIBRE OPTIC COMMUNICATION SYSTEMS: COMPONENTS AND PERFORMANCE

In this Section a number of the important components associated with transmission over optical fibre and the impairments which they introduce will be discussed. Measuring the system performance of fibre optic networks is another important consideration and therefore some methods for estimating system performance will also be presented in this Section.

2.4.1 OPTICAL FIBRE

The use of glass fibre in communications systems was first proposed by *Kao and Hockhan* in 1966 [2] and today optical fibre is used for the vast majority of long distance optical communication. Single mode optical fibre is the most suitable for applications in long reach optical communications. In single mode fibre the core has a small cross sectional area which only allows one mode to propagate. Single mode fibres have lower scattering losses and lower dispersion than multi-mode fibre.

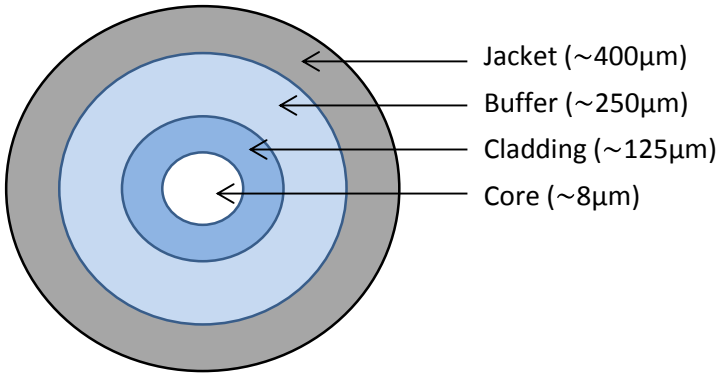

Figure 2.9. Cross section of single mode optical fibre

Multi-mode fibres have a much larger core diameter which results in the propagation of multiple modes. They are convenient for short reach applications but, due to increased attenuation and higher dispersion because of the multiple modes, they are unsuitable for systems requiring long transmission distances.

Figure 2.9 shows the cross section of a single mode optical fibre. An optical fibre is a cylindrical dielectric waveguide made of low loss materials such as silica glass. It has a high refractive index inner glass core in which the light is guided, surrounded by a lower refractive index outer cladding. This is covered with a protective buffer and outer jacket. The light is guided within the glass core and cladding by total internal reflection.

Attenuation in optical fibres:

Due to absorption and scattering effects [2] in the optical fibre a signal travelling along the fibre is subject to a loss of optical power. The attenuation depends on the wavelength of light travelling within the fibre and is normally measured in dB/km. The wavelength bands standardised by the telecoms industry are found in "windows" where the attenuation is at its lowest.

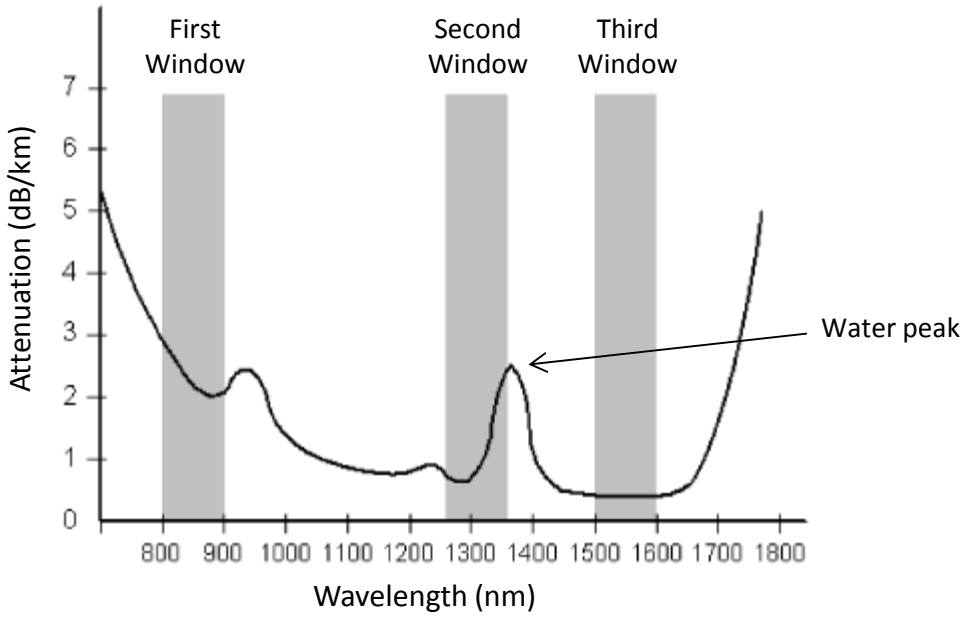

Figure 2.10. Fibre loss versus wavelength, showing the low loss transmission windows.

At a wavelength of 1310nm (O-band) for example the attenuation is approximately 0.5dB/km while at 1550nm (C-band) the attenuation can be as low as 0.2dB/km for commercially available single mode fibres. All work in this thesis was carried out in the "C-band" (1530-1565nm). In this region the fibre loss is low, while it is also the region where erbium doped fibre amplifiers operate (EDFAs). Figure 2.10 shows a plot of attenuation versus wavelength for standard single mode fibre (SSMF). The minimum attenuation level which can be achieved across the majority of the transmission wavelength range is set by Rayleigh scattering. A number of peaks can also be seen which are above the scattering level. These peaks are caused by water absorption, and can be seen as two small peaks in the attenuation between the first and second windows and as a significant peak between the second and third windows. The rapid increase in attenuation at long wavelengths is caused by infrared absorption.

The signal power in an optical fibre decreases exponentially with fibre length, and is given by

$$P_s(z) = P_s(0)e^{-\alpha z} \tag{2.1}$$

where $P_s(z)$ is the signal power (in watts), $P_s(0)$ is the power launched into the fibre and α is the attenuation coefficient in Neper/km. As the Neper is a logarithmic unit that uses the base e, fibre attenuation is normally defined in dB/km

$$\alpha_{dB} = 10.\log_{10}(e^{\alpha}) \tag{2.2}$$

Dispersion in optical fibres:

Chromatic dispersion in optical fibres is caused the frequency dependence of the fibre's refractive index. As a signal propagates along a length of fibre the frequency dependence results in different spectral components of the pulse travelling at slightly different group velocities and is therefore also known as group velocity dispersion (GVD). Chromatic dispersion results in pulse broadening of optical signals as they propagate through the fibre, which creates inter-symbol-interference (ISI)

at the receiver. This imposes a limitation on the data rate and distance for a transmission system. This is characterised by the dispersion parameter, D, which is given by [47]

$$D = \frac{d}{d\lambda}\left(\frac{1}{v_g}\right) = -\frac{2\pi c}{\lambda^2}\beta_2 = \frac{\lambda}{c}\frac{d^2 n}{d\lambda^2} \qquad 2.3$$

where β is the propagation constant and $\beta_2 = d^2\beta/d\omega^2$ which is known as the GVD parameter. The parameter D is expressed in units of ps/nm.km.

Rayleigh scattering:

Rayleigh scattering of light is an elastic scattering process which is a fundamental phenomenon in optical fibre propagation. During the fabrication of fibre Silica molecules move randomly in the molten state and then freeze in place. These density fluctuations lead to random changes in the refractive index which in turn result in Rayleigh backscattering (RB) [47]. The power of the backscattered light increases with transmission distance and reaches a maximum value of 31dB to 33dB below the signal power after approximately 20km (for fibre with a loss of 0.2dB/km). As Rayleigh scattering is a linear process there is no change in frequency on scattering and therefore the backscattered power is at the same wavelength as the incident optical signal. The RB light is partially polarised.

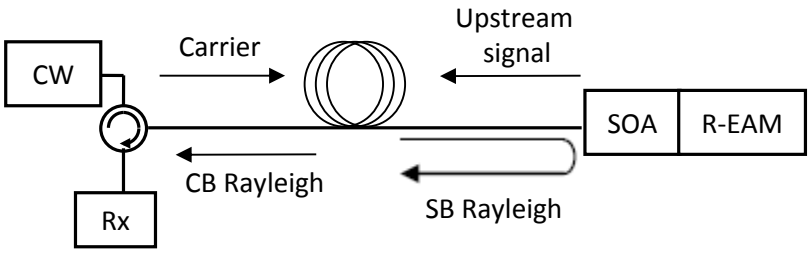

Figure 2.11. Two Rayleigh contributions in a carrier distributed PON.

The interferometic noise caused by the backscattering is of particular concern in a carrier distributed PON if a single backhaul fibre is shared for both the unmodulated upstream carrier and the upstream signal. The multiple reflections along the fibre path result in interferometic conversion of laser phase noise to intensity noise at

the receiver, which degrades performance [48], [49]. Figure 2.11 shows a diagram of the two Rayleigh contributions in a carrier distributed PON, carrier backscatter (CB) and signal backscatter (SB).

CB is caused by backscatter from the unmodulated carrier travelling into the network and SB is caused by the upstream signal. The RB from the signal starts out in the direction of the ONU but it is amplified and reflected back upstream by the R-EAM-SOA and therefore SB can contribute to noise at the upstream receiver.

As RB can cause significant performance degradation a number of RB mitigation scheme have been studied. For example, in [50] SB was supressed by an R-EAM-SOA operating in a regime of gain saturation, while in [51] and [52] advanced modulation formats are used to mitigate the effects of both CB and SB. Another approach used to mitigate the effects of CB is to use a dual-feeder fibre in the back-haul section [13].

Stimulated Brillouin scattering:

As proposed next generation PONs are targeting considerable increases in both physical reach and number of splits the power being launch into the fibre will need to increase in order to overcome the loss associated with fibre attenuation and splitter losses. One of the most significant impairments, which results from this increase in power launched into the fibre, is the inelastic scattering process known as stimulated Brillion scattering (SBS). The physical process behind SBS is the tendency of materials to become compressed in the presence of an electric field. When an intense optical signal travels through an optical fibre it generates an acoustic wave, which modulates the refractive index of the fibre in a periodic manner. The variation of the refractive index scatters the light through Bragg diffraction. This in turn generates a backward travelling wave in the opposite direction of the optical signal. The Bragg grating moves with certain acoustic velocity, depending on the material of the medium, and causes a Doppler shift of approximately 11.25GHz between the reflected wave and the original forward travelling optical signal (in silica glass fibre) [53]. For a single short pulse that has a width much smaller than the phonon lifetime there is very little SBS generation. However, for high speed bit streams successive pulses lead to a build-up of the

acoustic wave, similar to what occurs with a CW beam. The power reflected by SBS increases exponentially when the power is above the SBS threshold, which ultimately limits the optical power which can be launched into a fibre. The exact power level of the SBS threshold varies with modulation format.

SBS is a narrow band effect and the Brillouin gain has an intrinsic bandwidth of $\Delta v_b \sim$ 50MHz. Commercially available narrow band DFB lasers have linewidths of $\Delta v_{DFB} \sim$10MHz which is well inside the SBS gain bandwidth. The data format used for a significant amount of work in this thesis is non-return-to-zero on-off keying (NRZ-OOK) generated using an external modulator and a CW source with narrow linewidth. Therefore the resulting signal is very susceptible to SBS as half of signal energy is contained in the carrier component. SBS can be significantly supressed in these situations by applying a low frequency sinusoidal modulation to the laser [54]. This will cause the laser to be phase modulated resulting in a large effective laser linewidth which is outside the SBS gain bandwidth.

Other Non-linear processes:

Stimulated Raman scattering (SRS) is similar to SBS except that a high frequency optical phonon rather than an acoustic phonon is generated in the scattering process. SRS occurs when a photon collides with a silica molecule and gives up its energy to produce another photon of reduced energy at a lower frequency, while the remaining energy is absorbed by the silica molecule which ends up in an excited vibrational state [55].

There are also a number of non-linear processes which occur, where there is no energy transfer between the optical field and the dielectric medium. Such processes originate from intensity dependent variations in the refractive index of the silica fibre. This change in refractive index is known as the Kerr effect. The non-linear change in refractive index causes an intensity dependent non-linear phase shift which is referred to as carrier-induced phase modulation (CIP). This is called self-phase modulation (SPM) in single channel configurations, SPM converts optical power fluctuations in a light wave to phase fluctuations in the same wave. In WDM systems cross phase modulation (XPM) is also present which converts power fluctuations in one channel to phase fluctuations in other channels. Another effect

which occurs is known as four wave mixing (FWM). This occurs when the beating between light at different frequencies in multichannel fibre transmission causes phase modulation of the channels and hence the generation of modulation sidebands at new frequencies.

2.4.2 Optical Transmitters

The three basic modulator technologies which are widely used in today's optical communication systems are directly modulated lasers (DMLs), Mach-Zehnder modulators (MZMs) and electroabsorption modulators (EAMs). DMLs and MZMs will be discussed in this section while EAMs will be discussed in detail in Chapter 3.

Directly modulated lasers:

One of the most straightforward ways of encoding data onto an optical carrier is through the direct modulation of lasers. The laser drive current is modulated with the desired data, this turns on and off the output light from the laser resulting in binary intensity modulation (IM-OOK). Due to their compact size and low cost directly modulated lasers (DMLs) are ideal for use in optical access networks. DMLs are widely available at modulation speeds of 2.5Gb/s with some also available at 10Gb/s. The main drawback of DMLs for high bit rate transmission beyond short-reach applications is the residual phase modulation which accompanies the desired IM, this is known as chirp. Chirp arises because the direct modulation of a laser results in variations to the carrier concentration, this leads to changes in the refractive index with in turn affect the frequency of the optical signal. The frequency chirp broadens the optical spectrum which leads to increased signal distortions caused by chromatic dispersion and fibre non-linearity [56]. It can also lead to cross talk distortions among tightly packed DWDM channels.

The most common type of DMLs used for telecommunication applications are distributed feedback lasers (DFBs). In contrast to Fabry-Perot (FP) lasers where the facets provide the optical feedback in the laser cavity, DFB lasers contain gratings which provide the optical feedback along the length of the laser structure. This is achieved through an internal built-in grating that leads to a periodic variation of the

mode index. Feedback occurs by means of Bragg diffraction, a phenomenon that couples the waves propagating in the forward and backward directions [47].

DMLs are commonly used as transmitters in today's PONs. However, because of the issues caused by chirp in systems with bit rates of 10Gb/s or above the direct modulation of lasers is rarely used.

Mach-Zehnder modulator:

The Mach-Zehnder modulator (MZM) most widely used in communication systems today uses a waveguide based Mach-Zehnder (MZ) interferometer fabricated from the material $LiNbO_3$ (Lithium Niobate) for intensity modulation.

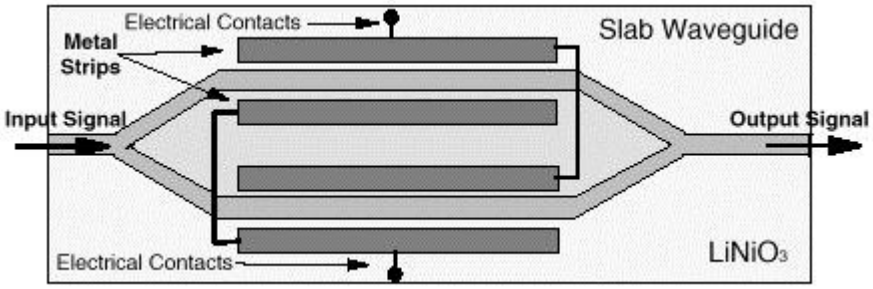

Figure 2.12. $LiNbO_3$ Mach-Zehnder modulator.

To make the modulator two titanium diffused $LiNbO_3$ waveguides form the two arms of the MZ interferometer as shown in Figure 2.12, with both arms of the interferometer also having electrical contacts. Using the Pockels effect the refractive index of $LiNbO_3$ can be changed by applying an external voltage. An incoming light beam is split into two paths at an input coupler. If no voltage is applied to the arms of the interferometer, the phase shift in both arms is identical and the optical signals in the two arms interfere constructively at the output. On the other hand if there is an applied voltage then the refractive of the interferometer arms is altered, resulting in a change to the interference condition of the beams at the output of the modulator. If a voltage is applied such that the arms of the interferometer have a π phase difference between them then there is total destructive interference and no light is transmitted. Therefore depending on the applied voltage, the interference varies between destructive and constructive,

thereby producing IM [56]. A MZM can operate without chirp if it is driven with equal but opposite voltage in each arm of the interferometer, this is known as push-pull operation.

2.4.3 Optical Amplifiers

One major problem associated with the realisation of long reach PONs is overcoming the losses experienced by optical signals from both fibre attenuation and losses from passive splitters, splices and connectors. Inline optical amplification is the preferred method of combatting these losses compared to the alternative option of O/E/O regeneration. The two types of amplifier which are of most interest in the PON configurations discussed in this thesis are semiconductor optical amplifiers (SOAs) and erbium doped fibre amplifiers (EDFAs). EDFAs will be discussed later in this section while SOAs, which are of particular interest for use as part of the upstream transmitter in carrier distributed PONs, will be discussed in detail in Chapter 3. A more detailed description of issues such as gain saturation will also be presented in Chapter 3.

The main degradation associated with the use of optical amplification arises from the generation of amplified spontaneous emission (ASE). This is especially problematic if optical amplifiers are cascaded at different locations on a fibre link as the ASE builds up in the system. ASE at wavelengths outside that of the signal wavelength can be supressed using optical filtering. However ASE that is present in the region at or close to the signal wavelength cannot be removed and establishes the minimum added noise of the amplifier. The optical signal to noise ratio (OSNR) is used to capture this noise build-up and the OSNR degrades with every amplifier along the path [57]. The OSNR is given by

$$OSNR = \frac{P_{sig}}{P_{ASE}}, \tag{2.4}$$

where P_{sig} is the average optical signal power in watts [W] and P_{ASE} is the ASE power [W] (formulas expressed in linear units unless stated). This power is measured in both polarisations and within a reference bandwidth (B_{ref}) of 12.5GHz

or 0.1nm (at 1550nm). The measured ASE is related to the ASE spectral density S_{ASE} [W/Hz] in the signal polarisation as

$$S_{ASE} = \frac{P_{ASE}}{2.B_{ref}}, \tag{2.5}$$

the factor of two comes about because of the two orthogonal polarisation dimensions in the fibre. Even though the ASE is assumed to be unpolarised, it is only the ASE polarised parallel to the signal which results in signal-spontaneous beat noise at the photodiode. The ASE in the orthogonal polarisation is added to the signal upon detection with the photodiode, however as the orthogonal ASE does not interfere coherently with the signal there is no signal-spontaneous beat noise contribution. For this reason S_{ASE} is defined as the spectral density in one polarisation.

The noise figure (NF) is used to quantify the degradation of the OSNR due to the amplifier being placed in the signal path. The NF is given by [57]

$$NF = \frac{P_{ASE}}{hv.B_{ref}G} + \frac{1}{G}, \tag{2.6}$$

where G is the gain of the signal at a frequency v [Hz], P_{ASE} is the ASE power at the output of the amplifier and hv is the energy of one photon at the signal frequency. If Equations 2.4 and 2.6 are combined, the expression for the OSNR at the output of an amplifier as a function of NF and input power is given by

$$OSNR = \frac{GP_{in}}{(GNF-1)hv.B_{ref}} \approx \frac{P_{in}}{NF.hv.B_{ref}}. \tag{2.7}$$

Erbium doped fibre amplifier (EDFA):

EDFAs are currently in widespread deployment for long-haul telecoms applications operating in the 1550nm wavelength region. They offer very high gain, low noise figures and can amplify multiple signals simultaneously. The biggest disadvantage of EDFAs is their limited wavelength operating range. EDFAs are constructed using an erbium-doped fibre, which has a silica glass host core doped with active Er^{3+} ions, as the gain medium [58], [59]. The erbium-doped fibre is then optically pumped at

either 980nm or 1480nm using a semiconductor laser in the 10mW to 100mW output power range. The signal and pump beams are combined using a WDM coupler and they co-propagate along the doped section of fibre. The pump beam excites the Er^{3+} ions which can then amplify the signal in the 1550nm region via stimulated emission. The amplification is limited to the 1550nm region as the transition of the Er^{3+} ions to the ground level result in emission in this region. It is also possible to counter-propagate the pump beam, where a second coupler at the output removes any residual pump beam.

2.4.4 Receiver Noise

Optical receivers are used in optical communications systems to convert the transmitted optical signals to electrical signals using a photodiode. The photocurrent i_p is proportional to the number of photons received per second of the optical signal P_{sig}

$$\langle i_{sig}(t)\rangle = R_\lambda P_{sig}, \tag{2.8}$$

where R_λ[A/W] is the responsivity of the photodetector and the angled brackets refers to the time averaged current. The responsivity changes as a function of the wavelength incident signal and from the detector properties such as the material which was used to make the detector. A simple expression for the responsivity of a photodetector is given by

$$R_\lambda = \frac{\eta q}{hv} \approx \frac{\eta\lambda[\mu m]}{1.24}, \tag{2.9}$$

where η is the quantum efficiency. The responsivity of a photodetector increases as the wavelength is increased because there are more photons present for the same optical power. This improvement in R does not continue for very long wavelengths however as the photon energy becomes too small to generate electrons and η drops to zero. This occurs when the photon energy is less than the energy bandgap ($hv < E_g$). The performance of an optical receiver depends on the signal to noise ratio (SNR) and is calculated as follows in terms of the received signal photocurrent for the 1-bit

$$SNR = \frac{\langle i_{sig}(t)\rangle^2}{\sigma_n^2}, \tag{2.10}$$

where σ_n^2 is the variance of the received photocurrent noise. The SNR is a ratio of electrical power levels rather than optical power levels. For noise processes approximated by Gaussian statistics, the mean is always zero so that the variance is equal to the mean-square value $\sigma_n^2 = \langle i_n^2(t)\rangle$. The autocorrelation function of $i_n(t)$ is related to the noise spectral density $S_n(f)$ by the Wiener-Khinchin theorem and a special case of this theorem gives [60].

$$\sigma_n^2 = \langle i_n^2(t)\rangle = \int_{-\infty}^{\infty} S_n(f)df. \tag{2.11}$$

Thermal noise and shot noise are two fundamental noise mechanisms which lead to fluctuations in the current even when the input optical signal has a constant power [47]. These current fluctuations result in electrical noise which degrades the receiver's performance.

Thermal noise:

Thermal noise, also called Johnson noise or Nyquist noise, is the electronic noise generated by the thermal agitation of the electrons inside an electrical conductor at equilibrium regardless of any applied voltage [47]. This noise is a consequence of Brownian motion [61]. The load resistor in the front end of an optical receiver adds such fluctuations to the current generated by the photodiode. The current fluctuation is modelled as a stationary Gaussian random process with spectral density that is independent of frequency (up to $f \sim 1THz$), this is given by

$$S_t(f) = \frac{2k_BT}{R_L}, \tag{2.12}$$

where k_B is the Boltzmann constant, T is the absolute temperature and R_L is the load resistor. Using Equation 2.11 the thermal noise variance is given by

$$\sigma_T^2 = \langle i_t(t)\rangle^2 = \int_{-\infty}^{\infty} S_t(f)df = \left(\frac{4K_BT}{R_L}\right)\Delta f, \tag{2.13}$$

where Δf is the effective noise bandwidth. Equation 2.13 includes thermal noise generated in the load resister only. To account for thermal noise added by other circuitry a quantity F_n is introduced known as the amplifier noise figure which gives

$$\sigma_T^2 = \left(\frac{4K_B T}{R_L}\right) F_n \Delta f. \quad 2.14$$

The SNR of the receiver taking only thermal noise into account is given by

$$SNR = \frac{\langle i_{sig}(t)\rangle^2}{\sigma_{thermal}^2} = \frac{R_L R_\lambda^2 P_{sig}^2}{4kTF_n\Delta f}. \quad 2.15$$

In a thermal noise limited system the SNR varies with P_{sig}^2. Increasing R_L can also improve the SNR.

Shot noise:

Since photons arrive at the photodiode in a random fashion, there is a statistical nature to the production of electron-hole pairs. This fluctuation in the generation of electron-hole pairs results in a fluctuation in the photocurrent. This is known as shot noise. The spectral density of the current fluctuations from shot noise is given by

$$S_{sh}(f) = 2q\langle i_{sig}(t)\rangle. \quad 2.16$$

Using Equation 2.11 to calculate the variance, the SNR for a shot noise limited system is given by

$$SNR = \frac{\langle i_{sig}(t)\rangle^2}{\sigma_{sh}^2} = \frac{\langle i_{sig}(t)\rangle}{2qB_e} = \frac{\eta P_{sig}}{2h\nu B_e}. \quad 2.17$$

The SNR increases linearly with P_{sig} in the shot noise limited regime and depends only on the photodiodes quantum efficiency, the receiver bandwidth and the photon energy.

ASE beat noise:

The ASE noise [62] generated by optical amplifiers can contribute significantly to the noise at the receiver, especially if multiple amplifiers are cascaded as the ASE

build up degrades the OSNR. When the optical signal is converted into an electrical signal by a square-law receiver the ASE field beats with the field of the optical signal. The electrical signal is therefore given by

$$\begin{aligned} i_p(t) &= R\left|E_{sig}(t) + N_{ASE}(t)\right|^2 \\ &= R\left|E_{sig}(t)^2\right| + 2R.Re\left\{E_{sig}(t).N^*_{ASE}(t)\right\} \\ &+ R|N_{ASE}(t)^2| \end{aligned} \quad 2.18$$

where * is the complex conjugate, R is the responsivity of the photodiode, N_{ASE} is the ASE noise field and E_{sig} is the optical signal field. There are three terms which make up the electrical signal. The first term is the signal, the second term is the beating of the signal with the ASE noise referred to as signal-ASE beat noise. This term depends strongly on the power of the optical signal. The final term represents the beating of the different ASE frequencies with each other and is known as ASE-ASE beat noise. As narrow optical filters can be used to filter out ASE which is outside the signal frequency the effect of ASE-ASE beating can usually be minimised.

Assuming the optical filter bandwidth at the receiver significantly exceeds the optical signal bandwidth and the receiver's electrical bandwidth, the beat noise variances can be written as [63]

$$< i^2_{sig-ASE} >= \sigma^2_{sig-ASE} = 4R^2 S_{ASE} P_{sig,1} B_e \,, \quad 2.19$$

$$< i^2_{ASE-ASE} >= \sigma^2_{ASE-ASE} = 4R^2 S_{ASE} B_{opt} B_e \,, \quad 2.20$$

where P_{sig} is the optical power, B_e is the receivers noise equivalent bandwidth, S_{ASE} is the ASE power spectral density in the signal polarisation and B_{opt} is the bandwidth of the optical filter. The overall current is a sum of all the Gaussian random variables and can therefore be considered Gaussian also. The total noise variance is given by

$$\sigma^2_{TOT} = \sigma^2_{sig-shot} + \sigma^2_{Thermal} + \sigma^2_{sig-ASE} + \sigma^2_{ASE-ASE}. \quad 2.21$$

The overall SNR is then given by

$$SNR = \frac{\langle i_{sig}(t)\rangle^2}{\sigma_{TOT}^2} = \frac{R^2 P_{sig,1}^2}{\sigma_{sig-shot}^2 + \sigma_{Thermal}^2 + \sigma_{sig-ASE}^2 + \sigma_{ASE-ASE}^2}. \quad 2.22$$

As the signal-ASE beat noise is proportional to the optical power of the signal and optical noise detected by the receiver the thermal noise will dominate if the OSNR of the system is kept sufficiently high. On the other hand if OSNR is degraded the signal-ASE beat noise term increases and will eventually rise above the thermal noise floor of the receiver when the OSNR is sufficiently reduced. In this scenario the system is beat noise limited. In the case of optical noise limited systems the SNR is related to the OSNR as follows

$$SNR = \frac{\langle i_{sig}(t)\rangle^2}{\sigma_{sig-ASE}^2} = \frac{R^2 P_{sig,1}^2}{4R^2 S_{ASE} P_{sig} B_e} = OSNR.\frac{B_{ref}}{B_e}. \quad 2.23$$

where the expression for OSNR is derived from Equations 2.4 and 2.5 and is given by

$$OSNR = \frac{P_{sig,avg}}{2.S_{ASE}B_{ref}} = \frac{P_{sig,1}}{4.S_{ASE}B_{ref}} \quad 2.24$$

2.4.5 System Performance

In optical communications systems the bit error rate (BER) is used to measure the overall performance of the system. The bit error rate is given by the total number of errors divided by the total number of transmitted bits during a defined time interval. For short time intervals the BER is only an estimate but over long time intervals the number of bits transmitted increases and the BER approaches the true probability of a bit error occurring.

$$BER = \left\{\frac{bits\ in\ error}{total\ transmitted\ bits}\right\}_{AVG} \xrightarrow{long\ averaging\ time} P[bit\ error]. \quad 2.25$$

In order for the measured BER to give a true representation of the probability of an error occurring it is important to ensure that enough bits have been transmitted. In order to achieve an accurate result in as short a time as possible it is important to know the minimum number of bits required for a statistically valid test [64]. The

target BER for laboratory experiments is in the range of 10^{-9} to 10^{-12} where forward error correction (FEC) will not be employed and 10^{-3} where FEC will be deployed. In order to get an accurate BER at least 10 or preferably 100 errors should be counted at each interval [64]. The majority of work in this thesis is carried out at 10Gb/s and therefore BERs of 10^{-9} or 10^{-10} are used in most instances to allow measurements be carried out in reasonable time scales.

The system performance can also be described using a parameter known as Q-factor [65]. The Q-factor is given by

$$Q = \frac{i_1 - i_0}{\sigma_1 + \sigma_0} \tag{2.26}$$

where i_1 and i_0 are the noise-free electrical signals for logical 1-bits and 0-bits respectively and σ_1 and σ_0 are the associated noise standard deviations. The Q-factor is related to the BER as follows [66]

$$BER = 0.5erfc\left(\frac{Q}{\sqrt{2}}\right) \tag{2.27}$$

where erfc is the complementary error function. Q-factor is specified in dB and it is convenient to convert Q from linear units to dB using $Q_{dB} = 20\log_{10}(Q_{linear})$ due to the relationship between Q and SNR [66]. Substituting Equation 2.26 into Equation 2.27 gives a rough approximation of the BER expected for a system [66]. If the assumption is made that the signal has a good extinction ratio ($i_1 \gg i_0$) and the 1-bit noise dominates over the 0-bit noise then the Q can be written as,

$$Thermal\ noise\ limited, Q = \frac{\sqrt{SNR}}{2} \tag{2.28}$$

$$Beat - noise\ limited, Q = \sqrt{SNR} \tag{2.29}$$

Equation 2.28 is for the thermal noise limited regime, while Equation 2.29 is for the beat-noise limited regime. The BER can then be written in terms of SNR as follows for a beat noise limited system,

$$BER = 0.5erfc\left(\sqrt{\frac{SNR}{2}}\right), \quad 2.30$$

and in a thermal noise limited system it can be expressed as

$$BER = 0.5erfc\left(\frac{1}{2}\sqrt{\frac{SNR}{2}}\right). \quad 2.31$$

The two most common methods of measuring system performance using BER are to either limit the optical power falling on the receiver in order to operate in the thermal noise limit regime or else to fix the power falling on the receiver at a sufficiently high level to stay above the thermal noise floor and degrade the OSNR of the signal in order to operate in the beat-noise limited regime.

2.5 CONCLUSION

With the demand for high bit rate services increasing, the bandwidth and/or physical reach of copper wires and wireless solutions are approaching their limitations due to physical media constraints. This is driving network operators to consider optical access networks in order to meet these ever increasing requirements. PONs are the most attractive optical access solution for network operators and have many advantages over the alternative optical access configurations, with cost being one of the most important factors. In this Chapter the operational principles of a basic PON were first explained and the most advanced PONs in current deployment were discussed.

However, the most advanced PONs deployed are currently beginning to struggle with the bandwidth demands being placed on them and this has resulted in huge interest in the next generation of PONs. A new standard for PONs is nearing publication known as NG-PON2, which hopes to address the demands for increased bit rates in both the upstream and downstream directions but even this may not offer sufficient advancement. This has resulted in more radical network configurations being proposed which would offer even greater improvements in performance than what NG-PON2 may provide.

The carrier distributed long reach PON is the configuration of most interest in this thesis. This type of PON configuration has the potential to significantly increase the number of users through the use of DWDM and offer much greater reach by integrating the metro and access networks and using optical amplification. One particular challenge of PONs operating on a tight DWDM grid is the upstream transmitter, which must stay tuned to a very strict wavelength grid. Using fixed wavelength sources at each ONU lacks flexibility, while there are still open questions on the low cost volume production of suitable tuneable lasers. By distributing the carrier from a central location and using colourless reflective modulators at the customer premises, the wavelength control is moved to a controlled environment leaving all ONUs colourless. This makes carrier distributed PON a very attractive solution for future optical access networks.

The integrated R-EAM-SOA is the most promising device to act as the upstream transmitter in a carrier distributed PON as it can achieve both the required net gain and low chirp modulation needed for 10Gb/s operation over distances in the order of 100km. In this thesis the performance and optimisation of the R-EAM-SOA is the central theme. The analysis will first concentrate on the behaviour of the device itself, where it will be studied using both an integrated device and discrete devices. Then a more network oriented analysis will demonstrate how the device can be configured to have optimal performance for use as the upstream transmitter in a carrier distributed PON. Before starting the device analysis, Chapter 3 will first address the background theory and operational principles of the three key devices in this thesis, the SOA, R-EAM and R-EAM-SOA.

3

Semiconductor-Based Devices for Carrier Distributed DWDM-PONs

The colourless reflective transmitter discussed in Chapter 2, for use in a carrier distributed DWDM-PON, requires both an optical amplifier and a high speed optical modulator. Semiconductor devices are the most attractive solution for building the reflective transmitter due to their relatively low cost, small size and the possibility to integrate amplifiers and modulators together in a single package. For this reason the upstream reflective transmitter is fabricated using a semiconductor optical amplifier (SOA) and electroabsorption modulator (EAM). The SOA can provide the gain required to overcome losses in the network while the EAM can provide the high speed (10Gb/s) and low chirp modulation needed to realise the long transmission reach which is proposed for next generation PONs. The SOA and EAM can be monolithically integrated to form an integrated R-EAM-SOA which allows the production of a very compact and low cost transmitter.

Before starting a detailed analysis of the R-EAM-SOA performance it is important to understand the operational principles behind the semiconductor devices used to fabricate it, in particular the SOA. Therefore, in this Chapter some important SOA design and operational concepts will be discussed in detail. The EAM will also be discussed before moving to the integrated R-EAM-SOA. The design and important performance metrics of the experimental devices, used in the following Chapters, are also briefly outlined in this Chapter.

3.1 SEMICONDUCTOR OPTICAL AMPLIFIERS

Figure 3.1 shows a simple schematic diagram of an SOA. The diagram shows the main parts of the SOA: the input and output facets, where a signal enters and leaves the device; the active region of the device where gain is provided to the signal; and the waveguide which confines the propagating signal to the active region.

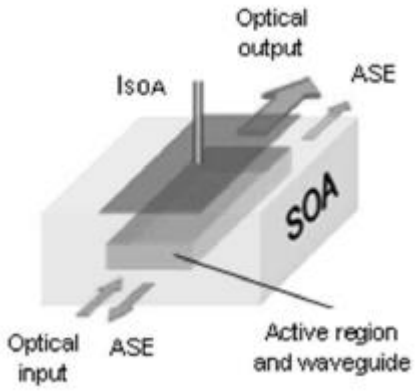

Figure 3.1. Schematic diagram of an SOA

The first step in the amplification process is the injection of electrons (carriers), into the active region of the SOA, from an external current. The energised carriers occupy energy states in the conduction band (CB) of the active region material, this leaves holes in the valence band (VB). There are three radiative mechanisms which are possible in the semiconductor. In Figure 3.2 [67] the three processes are shown, for a material with an energy band structure consisting of two discrete energy levels. Stimulated absorption occurs when an incident photon with sufficient energy stimulates a carrier from the VB to the CB. This is a loss process and results in the incident photon being absorbed by the material. If a photon with suitable energy is incident on the semiconductor, it can cause stimulated recombination of a CB carrier with a VB hole. The energy of the recombining carrier is lost as a photon of light. The new stimulated photon is identical to the photon which induced the process and will have the same frequency, phase and direction, i.e. it will be a coherent interaction. More stimulated transitions can be initiated from both the stimulated and original photons. If the injected current is high enough then a population inversion is created when the carrier population in the CB exceeds that

in the VB. In this case stimulated emission is more likely to occur than stimulated absorption and therefore the semiconductor will provide gain.

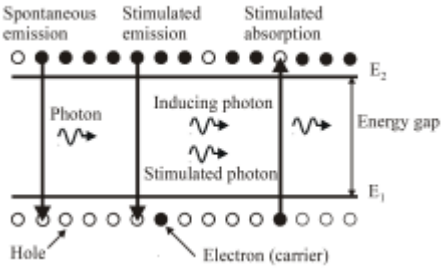

Figure 3.2. Spontaneous and stimulated processes in a two level system.

In the spontaneous emission process, a CB carrier spontaneously recombines with a VB hole and emits a photon with random phase and direction. Spontaneously emitted photons are a source of noise and cause a reduction in the available carrier population, thus reducing the available gain. Spontaneous emission is an unavoidable aspect of the amplification process. Stimulated processes are proportional to the intensity of the inducing radiation but spontaneous emission is independent of it. SOAs are used mainly in the 1.3µm and 1.55µm wavelength regions and are therefore fabricated from the same materials used to fabricate laser sources in these regions. III-V semiconductors are used to fabricate SOAs with some of the common materials being InP, InGaAs, AlGaAs and InAlGaAs. SOAs are essentially semiconductor lasers where the reflectivity of the end facets is low enough that lasing does not take place.

The basic SOA structure, as with a semiconductor laser is based on a double-hetrostructure (DH) design. A DH is made up of an active region which is sandwiched between p-type and n-type cladding regions, where there is a bandgap difference between the active region and cladding regions. Figure 3.3 shows the structure of a simple DH. Carriers are injected into the active region from the bias current and the DH confines the carriers to the active region. Without the DH the carriers would diffuse throughout the device and would require much greater injected current to achieve population inversion.

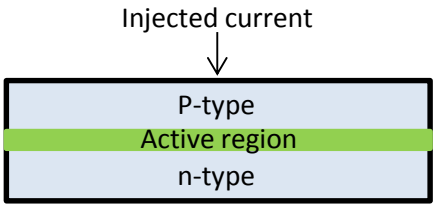

Figure 3.3. Basic DH SOA structure.

The carrier confinement in a DH is shown in the energy band diagram in Figure 3.4. The propagating light wave must also be confined to the active region since the carrier density is high enough to provide gain only in the central active region. If the waveguide is sufficiently narrow, it will only support one mode with two possible polarisations the transverse electric (TE) and transverse magnetic (TM) [67]. The DH is also beneficial for optical confinement as the active region has a slightly higher refractive index compared to the surrounding cladding regions. This helps to vertically confine the beam travelling through the device. However this simple DH structure does not provide lateral confinement of the propagating beam. Some confinement is provided by the injected current but it is inefficient. This device structure is known as gain-guided.

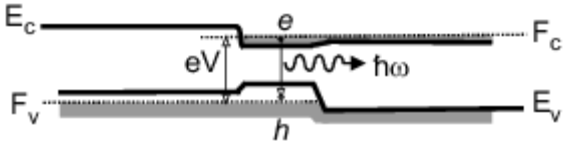

Figure 3.4. Energy band diagram of a DH

In order to improve the carrier injection efficiency and optical confinement there are two alternative structures used, these are weakly index guided structures and strongly index guided structures [68]. In Figure 3.5 (a) one of the possible weakly guided structures is shown, known as a ridge waveguide. In this design most of the p-type cladding is etched away to leave a mesa, only the mesa is contacted and this improves carrier injection by forcing the carriers through the ridge to the active region [69].

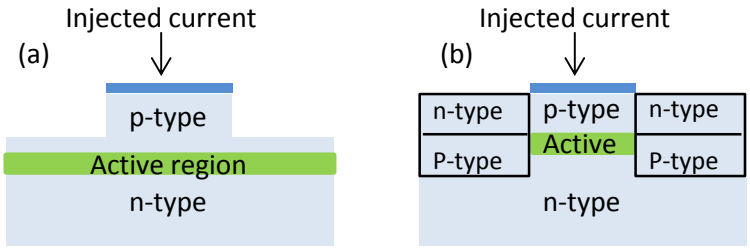

Figure 3.5. (a) Ridge waveguide, (b) buried heterostructure

The lateral optical confinement is also improved by effective changes in the refractive index from variations in the cladding thickness. Figure 3.5 (b) shows a buried heterostructure (BH), which is a strongly index guided structure. A BH gives further improvement in lateral mode confinement compared to the ridge waveguide. In a BH, the etch extends all the way to the n-type region and then a p-n junction is grown either side of the active region, therefore the active region is totally surrounded by cladding giving tight optical confinement. When a forward bias is applied to the device, the p-n junctions either side of the active region are reversed biased this forces carriers into the active regions and therefore increases carrier injection efficiency. BH SOAs have superior performance and are more efficient, however they are more difficult to produce than weakly guided or gain guided structures.

SOA active material:

The three types of active material used in SOAs are bulk, quantum well and quantum dot material, but for the purposes of this thesis the materials of most interest are bulk and quantum well. If the active region of an SOA has a dimension thickness which is significantly greater than the de-Broglie wavelength of carriers then it is called a bulk SOA [67]. If the active region thickness is reduced to a value approximately equal to the de-Broglie wavelength, the resulting extremely thin active layer is known as a quantum well (QW). A multi-quantum well (MQW) SOA can be fabricated by stacking well and barrier layers. The quantisation of energy levels that results from carrier confinement in the QWs generates sub-bands within the semiconductor bands, with step-like quasi-2-dimensional densities of states, which can lead to improvement in the active region performance. A MQW SOA can

be produced by stacking several layers and barriers using molecular beam epitaxy (MBE) and/or metal organic vapour deposition (MOCVD) techniques [67]. MQW SOAs can offer increased differential gain, larger gain bandwidths, improved saturation output powers and reduced noise figure.

Polarisation sensitivity:

An important consideration when using an SOA is the polarisation sensitivity of the gain. Because of the difference in the optical confinement between the lateral and vertical directions, differences in the waveguide symmetry and differences in the material gain in MQWs, the gain of the amplifier is different for the two polarisation states TM and TE. The polarisation dependant gain (PDG) is undesirable and is a source of impairment in systems employing SOAs.

The PDG of a bulk SOA can be reduced by using a BH structure and by ensuring the width and thickness of the active region are the same. However, as it is preferable to use MQW SOAs due to the advantages outlined above, a number of techniques are used to reduce the PDG. One technique is the use of a separate confinement heterostructure (SCH). In this structure, the active layer is sandwiched between an additional layer of material with a refractive index value between that of the active and cladding. This increases optical confinement in the vertical direction. Another method for reducing the polarisation sensitivity is the use of strained quantum wells or barriers [67] to reduce the difference in gain between the TM and TE polarisations.

3.1.1 Small Signal Gain and Gain Bandwidth

The gain spectrum of an SOA depends on its structure, materials and operational parameters with high gain and wide bandwidth being highly desirable [67]. Fabry-Perot (FP) SOAs are essentially FP-lasers biased below threshold. The end facet reflectivity is much lower than that of a FP-laser. The general equation for the cavity gain *G* of a Fabry-Perot (FP) SOA as a function of optical frequency *v* is

$$G_{FP}(v) = \frac{(1-R_1)(1-R_2)G(v)}{(1-G\sqrt{R_1R_2})^2 + 4G\sqrt{R_1R_2}\sin^2[\pi(v-v_m)/\Delta v_L]}, \quad 3.1$$

where R_1 and R_2 are the facet reflectivities, and Δv_L is the longitudinal-mode spacing also known as the free spectral range of the FP cavity given by

$$\Delta v_L = \frac{c}{2Ln_r}. \tag{3.2}$$

n_r is the material refractive index and v_m represents the cavity-resonance frequencies, which occur at integer multiples of Δv_L. The single pass amplification factor G is given by

$$G = \exp[gL], \tag{3.3}$$

when the amplifier is operating in an unsaturated regime. G_{FP} reduces to G when $R_1 = R_2 = 0$. $G_{FP}(v)$ peaks whenever v corresponds with v_m and therefore the amplifier bandwidth is determined by the sharpness of the cavity resonance. The bandwidth can be calculated from the cavity detuning $v - v_m$ for which G_{FP} drops 3dB from its peak value [47]. This is given by

$$\Delta v_A = \frac{2\Delta v_L}{\pi} \sin^{-1}\left(\frac{1 - G\sqrt{R_1R_2}}{4G\sqrt{R_1R_2})^{1/2}}\right). \tag{3.4}$$

In order to achieve a high amplification factor $G\sqrt{R_1R_2}$ should be close to 1. However, according to Equation 3.4 this will result in a small amplifier bandwidth, meaning FP amplifiers are not useful for most optical communication systems. Instead travelling wave SOAs (TW-SOAs) are preferred, where the signal only makes a single pass through the SOA. In order to design TW-SOAs the reflectivity of the end facets (R_1 and R_2) must be suppressed. The reflectivity must be extremely small (<0.1%) if the SOA is to act as a TW amplifier. The tolerance to facet reflectivity can be estimated by considering the max and min values of G_{FP} from Equation 3.1 near a cavity resonance [47]

$$\Delta G = \frac{G_{FP}^{max}}{G_{FP}^{min}} = \left(\frac{1 + G\sqrt{R_1R_2}}{1 - G\sqrt{R_1R_2}}\right)^2, \tag{3.5}$$

If ΔG exceeds 3dB, then the bandwidth is set by the cavity resonances rather than by the gain spectrum. Therefore the 3dB gain bandwidth of a TW-SOA is close to that given by the active material. To keep ΔG < 2, the facet reflectivities must satisfy

$$G\sqrt{R_1 R_2} < 0.17. \qquad 3.6$$

If Equation 3.6 is satisfied then the SOA can be characterised as a TW amplifier. For an SOA designed to provide 30dB of gain, $\sqrt{R_1 R_2}$ < 1.7x10^{-4} is required.

Suppression of facet reflections and coupling:

An important aspect of TW-SOA design is minimising facet reflectivities. Anti-reflection coatings are the most basic requirement for the reduction of reflections however it is extremely challenging to produce antireflection coatings with reflectivities less than 0.1%, this has led to the development of other techniques to reduce the reflection feedback in SOAs [47].

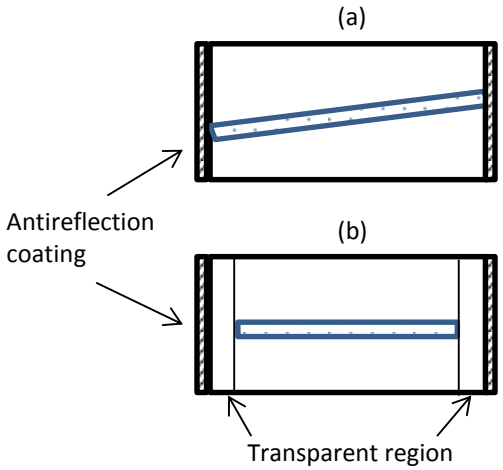

Figure 3.6. (a): SOA with angled waveguide, (b): window facet waveguide

One method is to incline the active region away from the facet cleavage angle as shown in Figure 3.6 (a). The active region is tilted by θ_p with respect to the norm of the input plane. This reduces the effective facet reflectivity by directing reflected light away from the active region into the cladding regions.

Another approach is a window facet (or buried facet) structure in which the window contains a transparent region which helps to reduce facet reflectivity as shown in Figure 3.6 (b). There is a trade-off using this method between the length of the window and the device effective reflectivity. Increasing the window length decreases the effective reflectivity which in turn reduces the coupling efficiency [55].

As well as minimising facet reflectivity another important consideration is the coupling of light into and out of the SOA active region. Figure 3.7 shows an SOA with both an angled and tapered waveguide. The very small refractive index difference in glass fibre results in a weakly guided mode with a typical mode size of 8µm to 10µm. However in a semiconductor waveguide there is greater refractive index difference which leads to mode sizes of 2 µm or less. In order to efficiently couple the light from the fibre into the SOA and from the SOA back to the fibre tapered sections are introduced at either end of the active region. These tapered regions increase the mode spot size as it propagates and maximises the coupling between the active region and the fibre at the input/output.

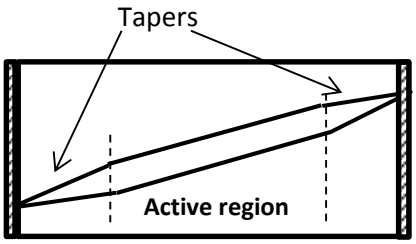

Figure 3.7. Angled waveguide with tapers.

3.1.2 SOA Gain Saturation

To calculate the gain of a TW-SOA for high input powers a carrier density rate equation is used, where the facet reflectivities are assumed to be zero. To discuss gain saturation consider the peak gain at the signal wavelength and assume it is a linear function of carrier density N

$$g = \Gamma\sigma_g(N - N_0) \qquad 3.7$$

where σ_g is the differential gain, Γ is the confinement factor and N_0 is the value of N at transparency. The rate equation for the carrier density can be written as follows in terms of optical power

$$\frac{dN}{dt} = \frac{I}{qV} - \frac{N}{\tau_c} - \frac{\Gamma\sigma_g(N - N_0)}{\sigma_m h\nu} P \tag{3.8}$$

where I is the injection current, q is the electronic charge, V is the volume of the active region, τ_c is the carrier lifetime, σ_m is the cross-sectional area of the waveguide mode, h is Planck's constant, ν is the optical frequency of the signal and P is the optical power. The first term on the right represents the addition of carriers in the conduction band from the injected current, the second term is the recombination due to spontaneous emission and the final term is recombination due to stimulated emission. The steady state value of N can be obtained by setting $dN/dt = 0$ in Equation 3.8. This can then be solved for N

$$N = \left(\frac{\tau_c I}{qV}\right)\left(\frac{1}{1 + P/P_s}\right) + \frac{N_0 P}{P + P_s}, \tag{3.9}$$

where the saturation power P_s is defined as

$$P_s = \frac{h\nu\sigma_m}{\Gamma\sigma_g\tau_c}. \tag{3.10}$$

Substituting Equation 3.9 into Equation 3.7 the gain is found to saturate as

$$g = \frac{g_0}{1 + P/P_s}. \tag{3.11}$$

where g_0 is the small signal gain given by

$$g_0 = \Gamma\sigma_g\left(\frac{\tau_c I}{qV} - N_0\right). \tag{3.12}$$

The amplifier gain G is defined as

$$G = \frac{P_{out}}{P_{in}}, \tag{3.13}$$

where P_{in} and P_{out} are the input and output power of the signal being amplified. The device gain can be calculated using the travelling wave propagation equation, where waveguide loss is neglected

$$\frac{dP}{dz} = gP(z) = \frac{g_0 P}{1 + P/P_s}. \quad 3.14$$

If Equation 3.14 is integrated across the length of the amplifier using the initial condition $P(0) = P_{in}$ and $P(L) = P_{out} = GP_{in}$ where L is the length of the SOA, then the following relation is found for the large-signal amplifier gain

$$G = G_0 \exp\left(-\frac{G-1}{G}\frac{P_{out}}{P_s}\right), \quad 3.15$$

This demonstrates that G decreases from G_0 when P_{out} approaches $\mathrm{P_s}$. Another quantity of interest is the output saturation power $P_{sat,3dB}$, which is the output power of the amplifier when G has been reduced from G_0 by half (3dB). Using $G = G_0/2$ and substituting into Equation 3.15,

$$P_{sat,3dB} = \frac{G_0 \ln 2}{G_0 - 2} P_s. \quad 3.16$$

3.1.3 Effects of SOA Non-Linearities

When an SOA is working in a regime of gain saturation the device behaviour is non-linear and there are a number of effects which occur because of this. Some of the most prominent effects are cross-gain modulation (XGM), cross-phase modulation (XPM) and Four-wave mixing (FWM) along with other effects such as self-gain modulation (SGM) and intensity noise suppression. These effects can have both negative and positive effects depending on the application. In this thesis the two effects of most interest are SGM and low frequency intensity noise reduction effects.

SGM induced distortions are a source of impairment in optical communication systems which use SOAs to amplify a high power intensity modulated signal. As SGM distortions introduced by the SOA depend on the pattern of the data signal

which it is amplifying, it is commonly referred to as patterning. If an NRZ-OOK data signal contains a long string of 0-bits, then the carrier concentration and hence the gain of the SOA is at its steady-state unsaturated value close to g_0 (Equation 3.12). If the power level of the following 1-bits is high enough to drive the SOA into saturation this results in a reduction of the carrier concentration and hence of the gain. The reduction in gain will happen over timescales dependent on the structure of the device, the bias current and the recombination parameters [70], [71]. If the bit rate of the signal is comparable with the timescales of the gain transient, the gain of the 1-bits, and hence their power at the output of the SOA, is dependent on the sequence of bits that preceded them and distortion in the amplitude of the 1-bits is introduced. In a similar way the gain of the 0-bits also varies with the preceding sequence. In Figure 3.8 we can see an example of an experimental 10Gb/s eye diagram at the output of a saturated SOA.

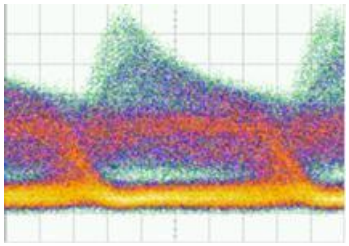

Figure 3.8. Eye diagram showing data patterning effects

The reduction in gain induced by the saturation can also have a beneficial effect. The non-linear amplification characteristic of a gain saturated SOA leads to the suppression of low frequency intensity noise on a saturating signal which is passed through the SOA. The effect can be explained in simple terms using Figure 3.9. When the saturating signal power leads the SOA to work in the non-linear part of its $\mathrm{P_{out}}$ vs $\mathrm{P_{in}}$ transfer characteristics, any small signal variation will experience a smaller gain compared to the saturating signal. The effect on the output signal is of a relative reduction of the small signal variations, which will depend on the frequency of the small signal.

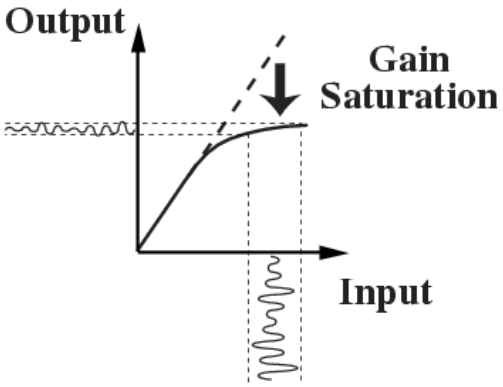

Figure 3.9. Noise suppression using saturated SOA [72].

Intensity noise which can appear on a CW carrier limits the achievable signal-to-noise ratio (SNR) of a signal and therefore reduces transmission performance. The intensity noise can come from a number of sources, for example relative intensity noise (RIN) due to spontaneous emission in semiconductor lasers or noise arising from sub-spectrum filtering of an incoherent light source (spectral slicing). It has been shown that a gain saturated SOA can be used to supress intensity noise at low frequencies [73] as it acts as a high pass filter. The suppression of the intensity fluctuations on the input light occurs across a bandwidth determined by the device operating point and the carrier lifetime. The noise suppression deteriorates at higher frequencies as the carrier concentration can no longer recover quickly enough to supress noise on the optical signal due to a limitation of the carrier lifetime of the SOA [72]. The same principal has also been used to mitigate signal induced Rayleigh beat noise using an R-EAM-SOA [50] and studies on SOA frequency response for wavelength conversion using XGM employ similar principles [74].

3.1.4 SOAs Used Experimentally

The SOA used for the analysis carried out in this thesis was an “SOA-S-OEC-1550” manufactured by CIP Technologies (now Huawei). The device is based on a buried heterostructure (BH) design in InP. The InGaAs MQW active region is approximately 0.88mm in length and features a tensile strained superlattice which gives a good differential gain, large bandwidth, good saturation power and low PDG. The devices

features a combination of an angled waveguide, large mode size and anti-reflection coated facets to minimise back reflections and features a tapered waveguide to improve coupling into optical fibres. Table 3.1 shows the main feature of the device.

Features	**SOA-S**
Optical bandwidth	60nm
Small signal gain	~22dB
PDG	Max 1.2dB
Noise figure	Max 7.5dB
Wavelength of peak gain	1525
$P_{sat, 3dB}$	~11dBm

Table 3.1. SOA-S features.

3.2 ELECTROABSORPTION MODULATOR

Electroabsorption modulators (EAMs) are very attractive devices for use in optical communications systems due to their high modulation bandwidth, compact size, ease of integration with other semiconductor devices such as semiconductor optical amplifiers and lasers and their ability to operate over a wide range of wavelengths. The electroabsorption (EA) effect is the change of the optical absorption coefficient in materials due to the presence of an electric field [75], these effects in a single optical waveguide directly result in optical intensity modulation. An EA waveguide usually consists of p-i-n semiconductor layers, among which the intrinsic layer has higher optical refractive index than the p-type and n-type doped layers to provide optical and electrical confinement.

The primary materials for fabricating EAMs working at 1300-1600nm optical wavelengths are III-V semiconductors, specifically, ternary and quaternary alloys (including InGaAs, InAlAs, InAsP, InGaP, In-GaAsP and InGaAlAs, etc) grown on an InP substrate [47]. These are also the choice materials for fabricating many other active optoelectronic components operating in the same wavelength range, including lasers, semiconductor optical amplifiers and photo-detectors. Hence,

EAMs are considered to be the most suitable modulator candidate for integration with these components. The most widely used integrated chips today are electroabsorption modulators and lasers, often with an SOA to boost output power [47]. Another advantage of EAMs is their compact size (typically 80-300µm long) due to high efficiency of the EA process. This leads to small footprint for a single device and high yield per wafer to lower the fabrication cost.

3.2.1 ELECTROABSORPTION EFFECT

There are two types of electroabsorption effects which occur in semiconductors, the Franz-Keldysh effect (FKE) in the bulk active layer and the quantum confined stark effect (QCSE) in QWs.

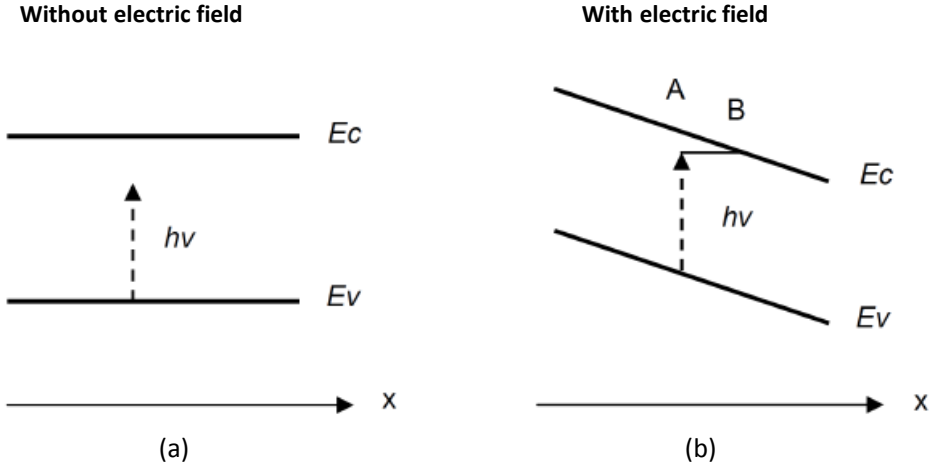

Figure 3.10. Franz-Keldysh effect for a bulk semiconductor material illustrated using a band diagram.

Franz-Keldysh effect (FKE):

Figure 3.10 (a) shows the band diagram of a bulk semiconductor without an applied electric field while Figure 3.10 (b) shows the band diagram with an applied electric field. When there is no electric field applied the incident photon has insufficient energy for an electron in the valence band (VB) to make a transition to the conduction band (CB) [75]. In contrast, when an electric field is present the energy bands are tilted and the photon energy hv meets the energy difference between the CB at location B and the VB at location A. The electron in the VB at location A

can now absorb one photon and make a transition to the CB at location B. This process can be referred to as photo-assisted interband tunnelling. The transition generates an electron-hole pair. If the electric field is increased, the distance between location A and B decreases which results in a larger transition rate which means the absorption coefficient is increased [75].

Quantum confined stark effect (QCSE):

In a semiconductor QW, both electrons and holes are tightly confined in a narrow well, so that the electron and hole energies are quantised to form discrete energy levels called "subbands" and the density of states $\rho(E)$ becomes a step function. This differs from the square root function of $\rho(E)$ in 3-D bulk material. Additionally, the confined electrons and holes are electrically bound as excitons which have a much smaller Bohr radius and a much larger binding energy than that of excitons in a bulk material. The properties of a QW therefore result in very different optical absorption behaviour than that seen in a bulk material [75]. Figure 3.11 shows ideal absorption spectra for a QW, where only the electronic transitions from heavy-hole subbands to the conduction band are considered.

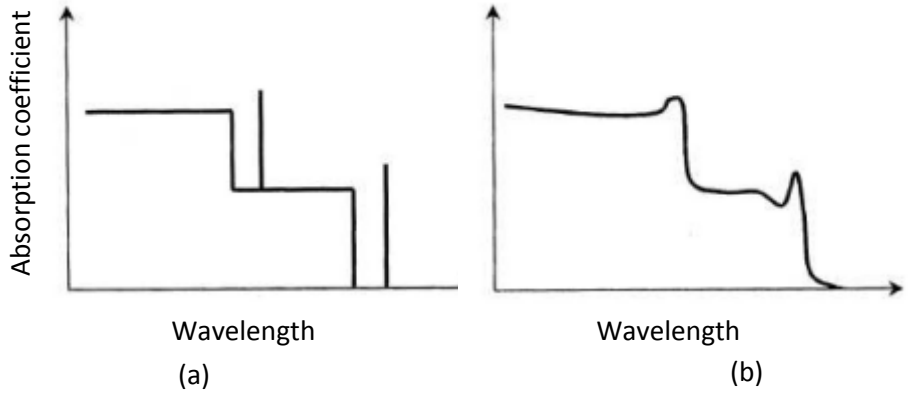

Figure 3.11. Optical absorption spectra for a QW. (a) idealised and (b) broadened.

The step feature is due to the inter-subband transitions and is determined by the step-like $\rho(E)$ function in a QW. The position of the step edges are located at

$$E_{cv} = E_g + E_e + E_h, \quad 3.17$$

where E_{cv} is the inter-subband energy gap, E_g is the bandgap of bulk material of the well layer, E_e is the electron energy level in the CB and E_h is the hole energy in the VB. The discrete lines are due to the exciton resonances located at

$$E_{ex} = E_{cv} - E_b, \quad 3.18$$

where E_{ex} is called the exciton transition energy and E_b is the exciton binding energy. Transitions from light-hole subbands result in a similar absorption spectrum, with step edges and the exciton lines shifted to shorter wavelengths due to the larger E_{cv} and smaller E_b. Figure 3.11 (b) shows a more realistic view of the optical spectrum with broadened step and exciton lines due to various broadening mechanisms. Despite the broadening the absorption edge is still very sharp for EAMs using a MQW active layer [75].

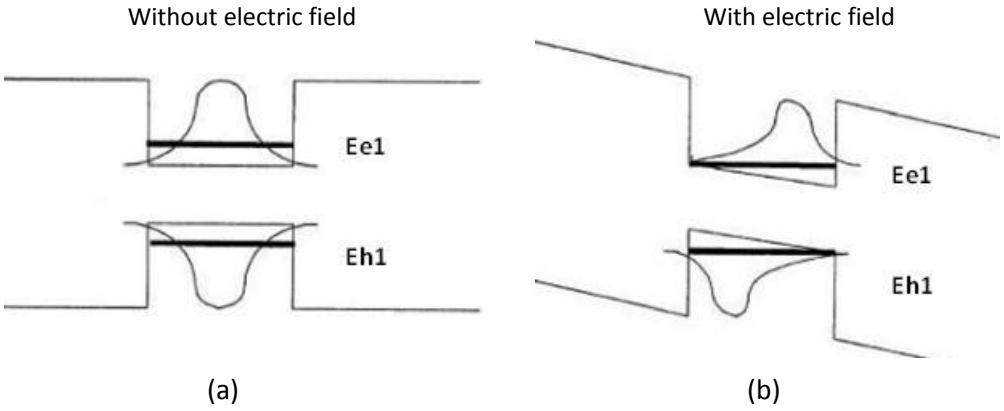

Figure 3.12. Quantum-confined Stark effect for a single QW.

When an electric field is applied across a QW, the band diagram is tilted and therefore the electron and hole confinements are changed. The electron energy levels E_c and hole energy levels E_h are reduced as shown in Figure 3.12. As a result, the exciton absorption peaks are shifted to longer wavelengths (red shift). The exciton linewidth is also further broadened due to the presence of the electric field. These two factors cause an increase in the optical absorption at the longer wavelength side of the band edge. This effect is known as QCSE [75]. Due to exciton resonance, QCSE induced absorption change is much larger than that of FKE.

Another important phenomenon is that the decrease in electron-hole overlap in the presence of an electric field reduces the exciton oscillation strength, and lowers the absorption. Thus there exists some optimum electric field for maximising the absorption change.

3.2.2 R−EAM USED EXPERIMENTALLY

The EAM used for the analysis carried out in this thesis was a reflective EAM (R-EAM-1550) manufactured by CIP Technologies. The R-EAM featured an InGaAs/InAlAs MQW core and enabled modulation up to 10Gb/s. The device operates across the C-band with low dispersion penalty due to optimised chirp and has low polarisation dependence. The main features of the device are shown in Table 3.2.

Features	**R-EAM**
Insertion loss	6dB
Polarisation dependent loss	~0.5dB
Small signal RF bandwidth	~20GHz
Extinction ratio under 10Gb/s NRZ modulation	~9dB

Table 3.2. R-EAM features.

3.3 R−EAM−SOA

As discussed in Chapter 2 one of the devices of interest for the realisation of long reach carrier distributed passive optical networks is the integrated reflective electroabsorption modulator semiconductor optical amplifier (R-EAM-SOA) [14]. The device, based on a monolithically-integrated combination of an R-EAM and an SOA, would be a key part of the optical network unit (ONU) and act as the upstream transmitter [12]. The customer transmitter needs to have sufficient launch power to overcome losses in the PON, have sufficient bandwidth to support bit rates of 10Gb/s and above and have sufficiently low chirp to enable transmission over distances of the order of 100km. The device is based on a monolithically-integrated combination of an R-EAM and an SOA.

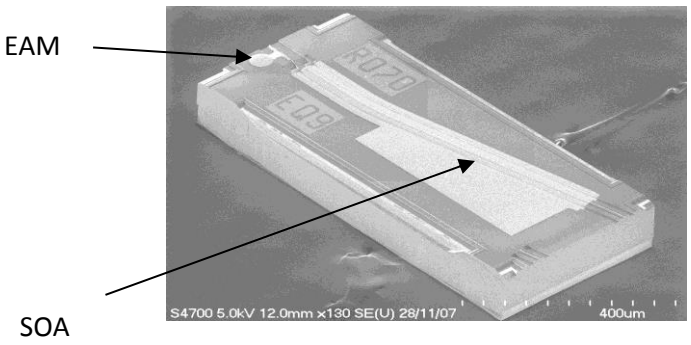

Figure 3.13. SEM micrograph of the R-EAM-SOA.

The R-EAM-SOA operates in a reflective configuration where an input CW carrier is first amplified by the SOA, the EAM then modulates the signal before reflecting the modulated signal back into the SOA where it is amplified again before launching it into transmission fibre. Since the R-EAM is inherently introducing loss the gain of the SOA is crucial to both overcome the loss of the R-EAM and the loss in the network.

The R-EAM-SOA analysed in this thesis (R-EAM-SOA-1550) was fabricated by CIP Technologies. It is the 3rd generation of these devices and is based on a buried heterostructure (BH) design with a butt-coupled interface allowing the SOA and EAM active regions to be separately optimized [14]. The SOA section in the device is approximately 670µm long and it includes an integrated curved waveguide and mode expander to minimize front facet reflection ($R<10^{-5}$ with AR coating). This also allows low loss coupling to a fibre with relatively relaxed alignment tolerances. The SOA active region is composed of a tensile strained InGaAs superlattice which helps to obtain a low polarization dependent gain. The butt coupled EAM section uses an InGaAs/InAlAs MQW core. This provides a low polarization dependent loss, a steep absorption characteristic and good performance with high optical power injection. The 50µm long EAM section had a high reflectivity coating at the rear facet so it operated in a reflective configuration [14]. Table 3.3 shows the main features of the device.

Features	R-EAM-SOA (3rd gen)
Small signal RF bandwidth	18GHz
Small signal gain	~15dB
PDG	~0.5dB
Extinction ratio under 10Gb/s NRZ modulation	~9dB

Table 3.3. R-EAM-SOA features.

3.4 CONCLUSION

In this chapter the SOA, the R-EAM and the R-EAM-SOA were introduced. These devices are central to the analysis that will be described in the following Chapters. The integrated R-EAM-SOA is of particular interest since it has potential to act as the upstream transmitter in the carrier distributed PON configuration which was described in Chapter 2. The SOA was introduced in particular detail as its performance is a key part of the operation of the R-EAM-SOA.

In the following two Chapters the behaviour and performance of the R-EAM-SOA will be analysed in detail using both the integrated device and a emulated device built using an discrete R-EAM and a discrete SOA. In Chapter 4 the R-EAM-SOA itself will be studied in detail using both experiments and modelling and a number of unique features will be demonstrated for this type of device. In Chapter 5 the device will be studied from a network perspective and using the analysis carried out in Chapter 4, modelling will be used to demonstrate an optimum configuration for an integrated R-EAM-SOA acting as the upstream transmitter in a carrier distributed PON.

4

Advantageous Effects of Gain Saturation in Semiconductor Optical Amplifier–Based Integrated Reflective Modulators

In this chapter a study is carried out on the behaviour of reflective modulators, based on the combination of a reflective electroabsorption modulator (EAM) and semiconductor optical amplifier (SOA), which are operating in a regime of gain saturation in the SOA section. Monolithically integrated reflective EAM-SOAs (R-EAM-SOAs) have demonstrated unexpected behaviour when operating in this regime, where the output power of the device is clamped around a maximum value and also the patterning effects normally associated with a gain saturated SOA are supressed [12]. Experimental results are presented from both an integrated R-EAM-SOA and an R-EAM-SOA which was emulated from discrete components [17]. The experimental measurements give an insight into how the output-input power characteristics of these devices are heavily dependent on the gain of the SOA section and the internal loss between the SOA and R-EAM sections in the device. Then using both an analytical model and an accurate numerical model the reason for this behaviour is explained in detail and it is demonstrated that, counterintuitively, a high value of internal loss and a high gain SOA allow utilisation of these devices in the region where the output power is clamped around a maximum value for input carrier powers compatible with those present in carrier distributed optical access networks, while also mitigating patterning distortions

[18]. The noise reduction on the input carrier due to the noise squeezing in the SOA section is also studied and it is shown that using a correctly designed R-EAM-SOA the noise reduction effect is accessible without patterning distortion [18].

4.1 INTEGRATED R–EAM–SOA

The first generation of the integrated R-EAM-SOA was developed by CIP for the EU project PIEMAN, where it was proposed to act as the upstream transmitter in a carrier distributed long reach PON. This device showed two unexpected and unintuitive characteristics [12] which are not observed with a traditional single pass transmission SOA. The first was the clamping of the output power of the device around a maximum value after which an increase in input carrier power produced no further increase in output power.

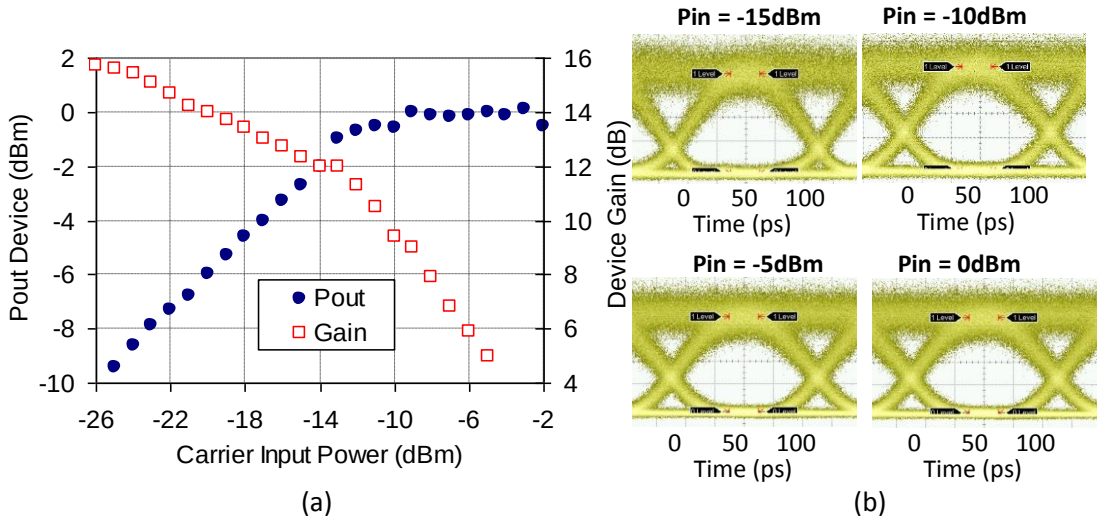

Figure 4.1. (a): Output power versus input power for 1st generation R-EAM-SOA. (b): Eye diagrams for 1st generation R-EAM-SOA for range of input powers indicated [12].

Figure 4.1(a) shows this feature, where for an input power of -10dBm upwards, the output power of the device is clamped at approximately 0dBm. This phenomenon was attributed to the presence of a high loss at the interface between SOA and R-EAM sections and to gain saturation effects in the SOA. The high loss present at the butt joint between the SOA and R-EAM can be caused by many factors such as

mode mismatch, interface reflections or interface roughness etc and the normal procedure would be to minimise this loss. The effect seen with the integrated R-EAM-SOA is similar to what has been reported in the literature for a reflective SOA (R-SOA) with low mirror reflectivity both experimentally [76] and using a simple analytical R-SOA model [77]. It was also shown in [17] that this power clamping effect can be very beneficial in a carrier distributed passive optical as it can help to reduce the burst to burst dynamic range of the upstream signal. As outlined in Chapter 2, this is a major issue in this type of network configuration. Figure 4.1(a) also shows the overall gain of the device versus input power. In this instance it can be seen that the gain has a similar trend to that which would be seen with a single pass transmission SOA. The second unexpected result was that the device, despite clearly working in a regime of SOA gain saturation, showed no degradation of the performance due to patterning distortion. Figure 4.1(b) shows a number of the eye diagrams presented in [12], it can clearly be seen that the eyes are not showing the high level of patterning which would be expected when amplifying a high input power modulated signal with an SOA. These results prompted a detailed analysis of R-EAM-SOAs in order to understand and explain this unexpected behaviour.

Despite the advantageous behaviour of the first generation R-EAM-SOA the device suffered from residual reflectivity at the SOA to R-EAM interface and cavity effects within the device which degraded its overall performance. Therefore two later generations of the device were developed. The second generation of the device also demonstrated similar poor performance which resulted in the development of the third generation R-EAM-SOA.

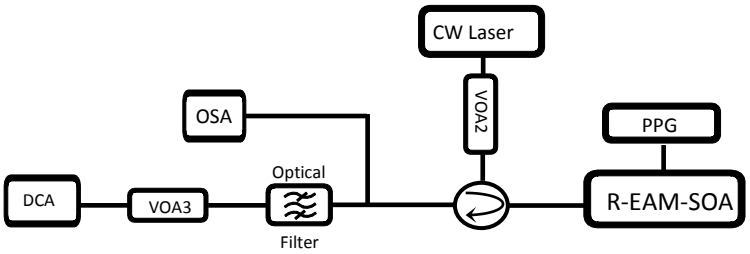

Figure 4.2. Integrated R-EAM-SOA characterisation setup

The third generation device featured a much improved butt joint between the SOA and R-EAM sections which leads to reduced reflections while a lower gain SOA section made the device less sensitive to any reflections which were still present. A study of the third generation device was therefore the first step in the analysis, to determine if it demonstrated the same unexpected behaviour as the device described in [12]. The experimental setup for the characterisation is shown in Figure 4.2.

A CW optical carrier of wavelength 1550nm was generated by a tuneable laser and injected into the R-EAM-SOA (CIP-R-EAM-SOA-1550) via a circulator. The input power to the device was varied using a variable optical attenuator (VOA2) to give a range of input powers from -20dBm to 0dBm, which are typical of the range encountered in a PON due to the variation in loss experienced by the carrier. The SOA was biased at 100mA and the R-EAM was biased at -1.5V and modulated at 10Gb/s with $3V_{pp}$ NRZ data (2^7-1 Pseudo random binary sequence (PRBS)).

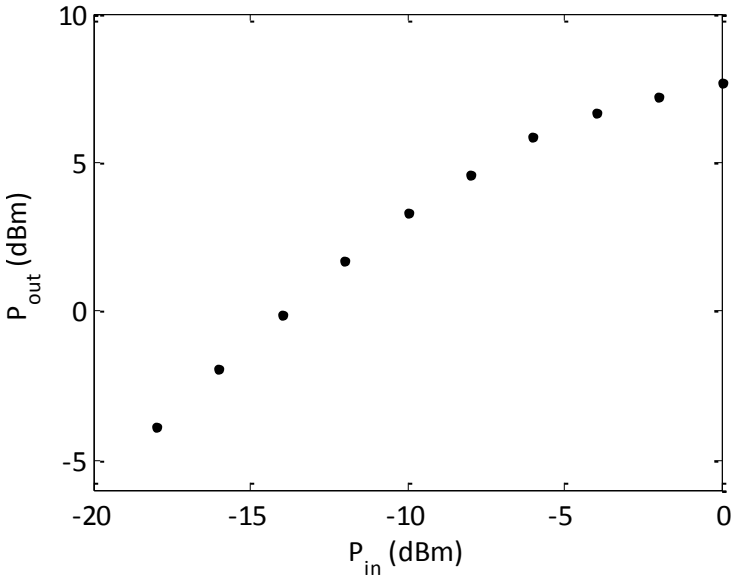

Figure 4.3. Measured output power versus input power for the integrated R-EAM-SOA.

The eye diagrams were measured at the output of the device using a digital sampling oscilloscope (DCA) with a 30GHz bandwidth optical input and the output

power from the device was measured using an optical spectrum analyser (OSA). VOA3 was used to set the input power falling on the DCA. A 1nm bandpass filter tuned to 1550nm was used to minimise the amplified spontaneous emission (ASE) falling on the DCA. Figure 4.3 shows the plot of output power versus input power measured for the integrated R-EAM-SOA. It is obvious that this device does not exhibit the power clamping effect seen in Figure 4.1(a) [12] within the range of input powers examined experimentally, which is the range of interest for a typical PON. It is only when the input power significantly exceeds 0dBm that the output power of this device would begin to clamp.

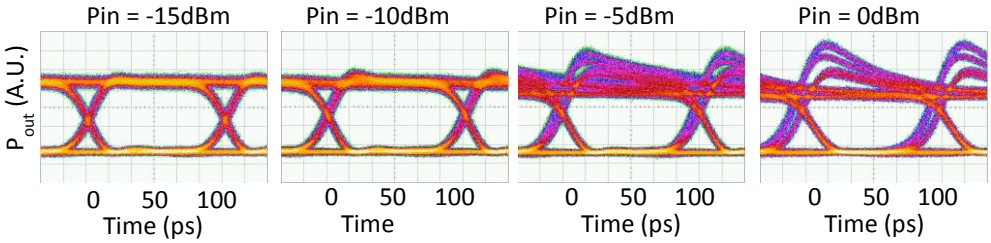

Figure 4.4. Eye diagrams measured for the integrated R-EAM-SOA.

Figure 4.4 shows the eye diagrams measured from the output signal of the integrated R-EAM-SOA for input powers of -15dBm to 0dBm in 5dB steps. In comparison to the eye diagrams seen in Figure 4.1(b) [12] the eyes for this version of the R-EAM-SOA suffer from patterning distortion as the input power is increased, with the eyes being heavily patterned at -5dBm and 0dBm. To fully understand this behaviour it would have been necessary to control the loss between the SOA and R-EAM section, however as it was not possible to change the internal loss of the integrated R-EAM-SOA a more in-depth study could not be carried out using this device.

4.2 DISCRETE R–EAM–SOA

An alternative setup was therefore required with which the internal loss of the R-EAM-SOA could be varied in a controllable fashion, which was not possible in the integrated device. This would allow a more detailed study of the unexpected effect

the internal loss in the device had on its performance. Figure 4.5 shows the experimental setup which was designed to emulate the integrated R-EAM-SOA using discrete components [17].

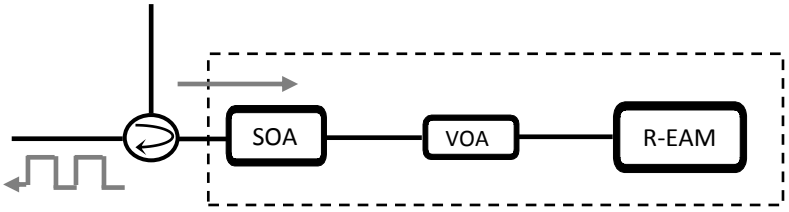

Figure 4.5. R-EAM-SOA emulated from discrete components.

To build the emulated R-EAM-SOA a discrete SOA is connected to a discrete R-EAM via a variable optical attenuator (VOA) which was placed between the SOA and R-EAM. The VOA emulates the interface loss between the SOA and R-EAM section which would be present in an integrated device. The internal loss in the integrated R-EAM-SOA is an additional loss located where the SOA section is butt coupled to the R-EAM section. While the discrete devices do have input/output coupling losses, the internal loss is unique to the R-EAM-SOA as it is a result of the integration process. Therefore this loss must be emulated by the VOA.

The configuration in Figure 4.5 allowed the effects of variation in internal loss to be investigated which would not be possible with a fully integrated device, albeit with the trade-off of a much longer internal delay between the SOA and the R-EAM due to the fibre pigtails of the discrete components (approximately 60ns round trip delay).

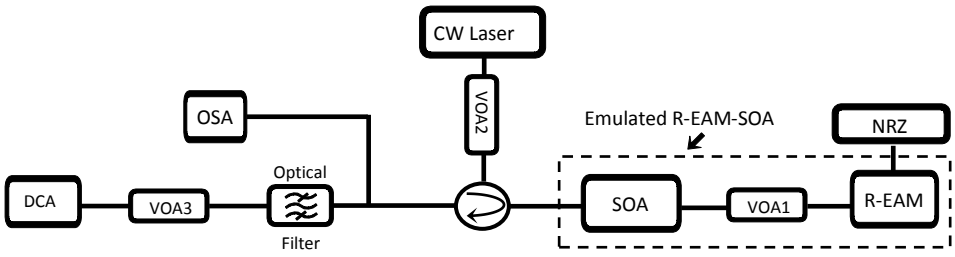

Figure 4.6. Experimental setup using R-EAM-SOA emulated from discrete components

As seen in Figure 4.5, the emulated R-EAM-SOA operates in a similar way to the integrated device. A CW carrier is amplified as it passes through the SOA, it then passes through the VOA before being modulated and reflected by the R-EAM. The backward modulated signal passes back through the VOA and then passes through the SOA for a second time and the output modulated signal is extracted using a circulator. The experimental set-up for the characterisation of the emulated R-EAM-SOA is shown in Figure 4.6. A discrete SOA (CIP SOA-S-OEC-1550) and a discrete R-EAM (CIP REAM-1550-LS) were connected together via a VOA (indicated as VOA1 for clarity) with a double pass loss which represents the internal loss in an integrated device, it should be noted that this loss is in addition to the insertion loss of the SOA on the port closest to the R-EAM and the absorption loss of the R-EAM. When driven at the designed operating current of 100mA, the SOA had a small signal gain (G_0) of 23dB at the gain peak wavelength of 1550nm and it had a saturated output power ($P_{sat,3dB}$) of ~11dBm. The R-EAM was modulated at 10Gb/s with $3V_{pp}$ NRZ (2^{31}-1 PRBS) data superimposed on a DC bias, which was set to -1.4V.

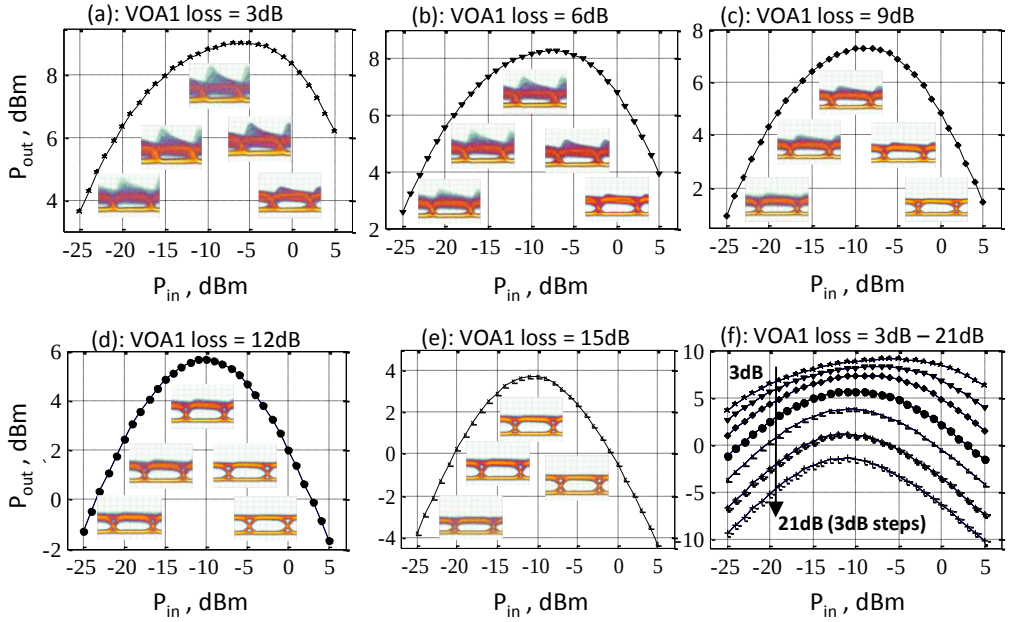

Figure 4.7. (a)-(e): Output power versus input power and eye diagrams for VOA1 loss values of 3dB to 15dB in 3dB steps. (f): Output power versus input power on same scale

Figure 4.7(a)-(e) show the modulated output power versus input power characteristics for the emulated R-EAM-SOA, obtained for VOA1 loss values in the range 3dB to 15dB (3dB step size) and Figure 4.7(f) shows all the output power versus input power curves plotted together on the same vertical scale for internal loss values from 3dB to 21dB (3dB step size). In contrast to the integrated R-EAM-SOA in Section 4.1 the results for the emulated device show a number of unique and striking features which result from gain saturation effects. It can be seen that for all values of VOA1 loss the output power is clamped around a maximum value after which the output power decreases with increasing input power. As the VOA1 loss is increased the output power is clamped at lower and lower values and the output power decreases more as the input power is increased. This is illustrated clearly in Figure 4.7(f).

The output eye diagrams were also measured for input powers in the range of -20dBm to 0dBm (5 dB step size) and are superimposed on the output power versus input power plots (Figure 4.7(a)-(e)). It can be seen that the degree of data patterning and eye closure induced by the gain saturation depends strongly on the value of VOA1 loss and it is greatly reduced at the higher loss values. The higher gain of the SOA used in the emulated R-EAM-SOA, compared to the much lower gain of the SOA in the integrated device, is also crucial.

In Figure 4.7(a), where the VOA1 loss was set to 3dB, heavy data patterning can be seen on all eye diagrams except for the highest input power of 0dBm, the level of patterning is particularly high in the input power range of -15dBm to -5dBm. When the VOA1 loss is increased to 6dB, as shown in Figure 4.7(b), a small improvement can be seen in the eyes with the levels of patterning reduced for all input powers. There are however still significant levels of patterning and eye closure, particularly at input powers of -15dBm and -10dBm. In Figure 4.7(c) where the VOA1 loss is increased to 9dB a more significant improvement can be seen for all input powers compared to both lower loss conditions, however there is still visible eye closure as a result of residual patterning. When the VOA1 loss is increased to 12dB in Figure 4.7(d) much improved eye opening is found for all input powers, with patterning now almost completely eliminated. Similar results are found in Figure 4.7(e) when

the loss is increased to 15dB, where there is little evidence of data patterning. Although not shown here the eye diagrams were also measured for VOA1 losses of 18dB and 21dB but no further improvement was found.

This analysis indicates that an optimum VOA1 loss is reached in the 12dB to 15dB range, this range best compliments the gain of this particular SOA. Increasing the loss of VOA1 to values greater than 15dB is not beneficial as patterning has already been almost eliminated and higher losses result in decreased output power as can be seen in Figure 4.7(f). The analysis here also confirms that the different behaviour seen with the first generation R-EAM-SOA in comparison to the third generation R-EAM-SOA is due to the low internal loss and low gain SOA combination present in the third generation device.

The emulated R-EAM-SOA has given further insight into the unexpected behaviour of saturated R-EAM-SOAs and the key role played by the internal loss, however in order to achieve a better understanding of the phenomena seen experimentally and better explain the origin of the output power clamping and patterning reduction seen with the emulated R-EAM-SOA, the devices were studied using two models, an analytical model and then a more comprehensive numerical model.

4.3 ANALYTICAL R−EAM−SOA MODEL

The first model used to study the behaviour of the R-EAM-SOA was an analytical R-SOA model which accounts for the double pass nature of the device. The model was presented in detail in [77] and is described in detail in the Appendix.

Parameter	value	Units
G_0	23	dB
P_{sat}	10	dBm
Internal loss (VOA1)	9 – 21	dB

Table 4.1. Parameters used in analytical model

In [77] parameter R represents the mirror reflectivity of an R-SOA, this is equivalent to the total internal loss experienced in the R-EAM-SOA (SOA insertion loss at facet

closest to the R-EAM, SOA to R-EAM interface loss (VOA1 loss) and R-EAM absorption loss). To implement the model, the parameter R is set to the total internal loss of the emulated R-EAM-SOA in Section 4.2, made up of the chosen VOA1 loss, the R-EAM absorption loss which was measured to be approximately 5.7dB and an SOA to R-EAM coupling loss which was measured to be approximately 2.8dB (double pass) in full transmission (0V bias). The values used in the analytical are listed in Table 4.1.

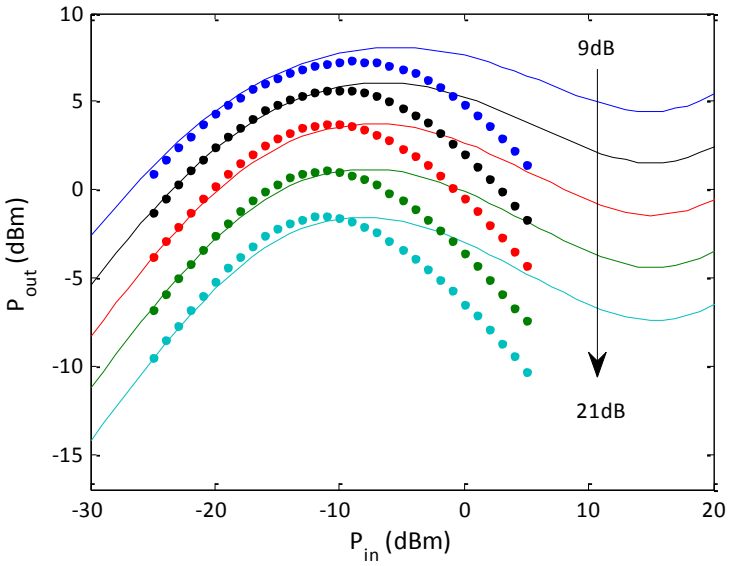

Figure 4.8. Output power versus input power for the emulated R-EAM-SOA, VOA1 losses of 9dB to 21dB in 3dB steps are shown. Dots represent experimental results and solid lines represent results obtained using the analytical model.

Figure 4.8 shows a plot of the experimentally measured output power versus input power for VOA1 losses from 9dB to 21dB in 3dB steps, compared to results of the analytical model. The value of G_0 used was 23dB, a saturation power ($P_{sat,3dB}$) of +10dBm and the mirror reflectivity ranged from -18dB to -30dB in 3dB steps (which corresponds to VOA1 losses from 9dB to 21dB). The values of the mirror reflectivity correspond, with opposite sign, to the total internal loss of the emulated R-EAM-SOA, i.e. a mirror reflectivity of -18dB corresponds to a total internal loss of 18dB.

It can be seen in Figure 4.8 that the model shows good agreement with the measurements for all values of internal loss in the linear regime when the input

power is low. As the input power increases the model is also able to reproduce the output power clamping effect seen in Figure 4.6, however the analytical model could not match the exact peak output power or the position the peak. In Figure 4.8 the model parameters were adjusted to match the linear regime, alternatively the parameters could have been adjusted to match the peak output power or the position of the peak, but using this model it was not possible to obtain an accurate match of all three for the same set of parameters. The inability to get a close match between experiments and modelling for the linear regime, peak power and peak position for the same parameter settings is due to a number of simplifications in the SOA model, for example, both waveguide loss and ASE are neglected in order to obtain an analytical solution. Despite this the model does indicate that the power clamping observed is caused by the internal loss in the R-EAM-SOA, which is equivalent to a reduced mirror reflectivity in an R-SOA.

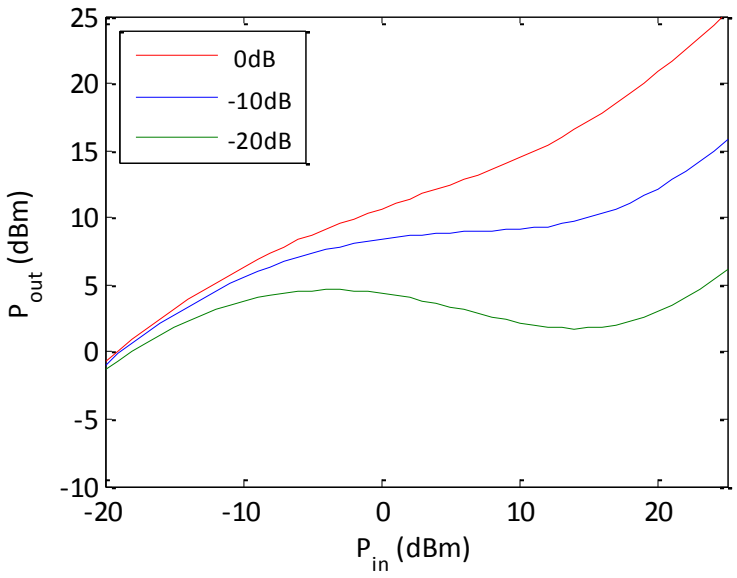

Figure 4.9. Output power versus input power for the analytical model for a $P_{sat,3dB}$ of +10dBm and reflectivities of 0dB, -10dB and -20dB and G_0 of 10dB, 15dB and 20dB. The overall unsaturated gain of the device is the same in all cases.

This can be demonstrated by referring to [78] where it was shown that as the mirror reflectivity approaches 100%, or equivalently the internal losses are negligible, the output power clamping disappears and the device behaves similarly

to a single pass transmission SOA. This happens because the power of the backward signal travelling through the SOA is always stronger than the forward signal. Hence the gain saturation is governed by the power of the backward signal alone. To clearly show these effects the output power versus input power behaviour was modelled for a device with a $P_{sat,3dB}$ of +10dBm, a mirror reflectivity of 0dB (100%) and a G_0 of 10dB. This is shown by the upper curve in Figure 4.9. For this device configuration the saturation can be seen as a reduction of the slope for input powers to the SOA above approximately 0dBm. If the internal loss is increased (or the mirror reflectivity reduced) the saturation of the SOA begins to be dominated by the forward signal. The forward signal becomes the dominant contribution to saturation if the internal loss is higher than the single pass gain of the SOA.

Under these conditions, once the SOA enters saturation the gain decreases rapidly with an increase in input power. However the forward signal power at the interface between the SOA and R-EAM only sees a small increase and can be considered constant to a first approximation. The backward signal power at the internal interface, after it has experienced the internal loss, is also then roughly constant as a function of the input power. The backward signal, however, experiences the same gain which was experienced by the forward signal and this gain decreases rapidly with increasing input power. The overall effect is that the output power of the SOA decreases as a function of increasing input power. This can be seen in Figure 4.9 for input powers above -5dBm, when the mirror reflectivity is set to -20dB and G_0 is set to 20dB. Using the model it is also possible to show that the decrease in output power always begins to occur when the forward signal power at the interface is approximately equal to the saturation power of the SOA.

It is interesting to note that as soon as the there is any amount of internal loss there is an input power range for which the forward signal starts to be the dominant contribution to the saturation. However, if the internal loss is low, this regime can only be reached for high powers and for a limited range before the SOA gain is completely depleted. Intermediate situations also arise, such as setting the reflectivity to -10dB and G_0 to 10dB as shown in Figure 4.9. In this case the decrease in power might not be present and instead only a flattening of the output power

versus input power curve is observed. For any value of internal loss the SOA gain will be completely depleted if the input power is increased to high enough values. In this case the signals only experience the internal loss and the output power starts to increase again with an increase in input power.

The simple analytical model used in this section allows us to determine useful trends in terms of some device parameters. Due to the approximations introduced, however, the match with the experiments is only qualitative and not accurate as can be seen in Figure 4.8. Therefore it cannot be employed to accurately optimise the characteristics of the R-EAM-SOA in terms of the design parameters. The analytical model also neglects the time evolution of the optical and driving signals hence it cannot be used to examine the other phenomenon observed Section 4.2, which is the absence of patterning degradation on the output signal despite the SOA being in saturation.

4.4 NUMERICAL R−EAM−SOA MODEL

A more accurate time domain model is therefore necessary to further analyse the emulated R-EAM-SOA. All of the R-EAM-SOA analysis presented throughout the rest of this thesis uses the numerical R-EAM-SOA model, which is described in detail in the Appendix. The key part of the R-EAM-SOA model used to analyse the experimental results in this paper is the SOA model, which is described in detail in [70].

Several models have been developed in the past to simulate the characteristics of SOAs. In order to accurately model the carrier dynamics inside the devices the model needs to account for the effects of the amplified spontaneous emission (ASE) on the carrier recombination. Models that account for the effects of ASE in CW simulations can be found in the literature [79], [80] but only recently have the effects of ASE been included in time domain SOA models [81], [82], [83]. Various solutions have been proposed to account efficiently for the ASE. A simple solution is to consider the propagation of the ASE only at the signal wavelength [84]. In this case there is a problem in the determination of a value for the spontaneous emission coupling coefficient β. Another solution is to include the whole ASE

spectrum [83], this is very accurate but it is also very computationally intensive. A more efficient solution is to consider the effects of the whole ASE using an effective value for β [81], [82]. The numerical model described in the Appendix is similar to the models in [81], [82]. It accounts for the saturation caused by the bidirectional ASE propagation in the device, which is an important phenomenon to understand and to obtain accurate behaviour regarding the carrier saturation and recovery in SOAs [71]

As with the analytical model, the first step with the numerical model was to attempt to reproduce the output power versus input power characteristics obtained experimentally using the emulated R-EAM-SOA.

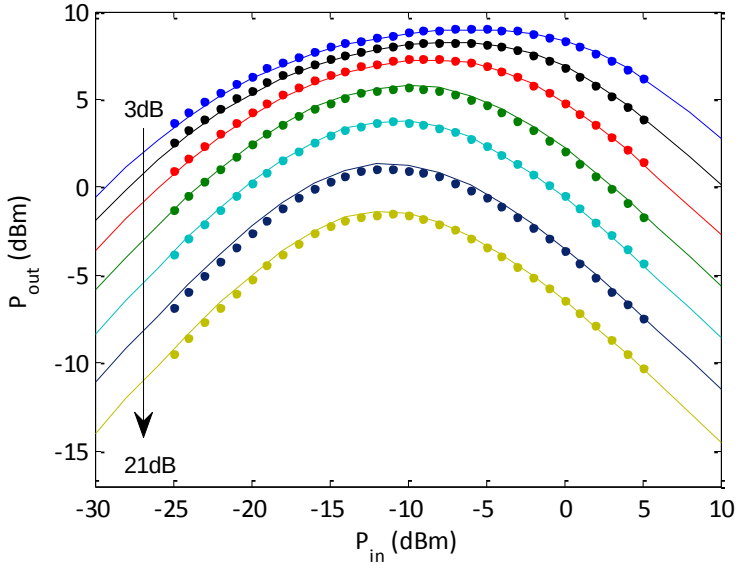

Figure 4.10. Output power versus input power for the emulated R-EAM-SOA with a VOA1 loss range from 3dB to 21dB in 3dB steps. Dots represent the experimental measurements shown in Section 4.2 and lines represent the results obtained using the numerical model.

The conditions for the modelling are set to match those used experimentally, the carrier wavelength is set to 1550nm, the SOA bias current is set to 100mA and the R-EAM is modulated at 10Gb/s with NRZ data. The R-EAM absorption loss is fixed at 5.7dB and the SOA insertion loss on the facet closest to the R-EAM is fixed at 2.8dB (double pass). The length of the SOA was set to 0.88mm which gave a G_0 of 23dB at a bias current of 100mA. Then, as in the experimental setup the VOA1 loss is swept

from 3dB to 21dB in 3dB steps and the input power to the modelled R-EAM-SOA is swept from -30dBm to +10dBm, this covers the entire input power range which was studied experimentally. Figure 4.10 shows the modelled output power versus input power found using the numerical model compared to the experimental measurements for the emulated R-EAM-SOA. The excellent agreement between measurements (dots) and modelling results (solid lines) is a validation of the modelling approach used here. It is clear from the plot that the numerical model can reproduce the clamping of the output power seen experimentally over the wide range of VOA1 loss. The model can also accurately reproduce the exact output power peak as a function of increasing VOA1 loss and the reduction in output power after the peak as the input power is further increased.

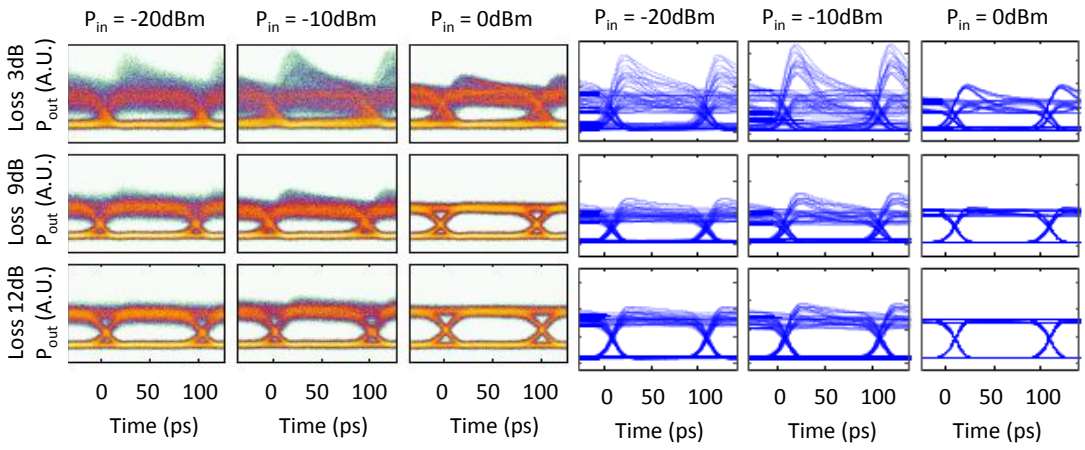

Figure 4.11. Eye diagrams for emulated R-EAM-SOA. (a): experimental measurements, (b): modelled eyes.

It is important to note at this point that all of the model parameters were determined in this case by measurements on the discrete components and no parameters were used to fit the simulation results to the measurements. The full list of parameter values used for modelling the emulated R-EAM-SOA is shown in Table 4.2.

The model was then used to generate eye diagrams for the emulated R-EAM-SOA in order to study the patterning introduced by the SOA gain saturation. Eye diagrams were modelled for VOA1 losses of 3dB, 9dB and 12dB with input powers to the R-EAM-SOA of -20dBm, -10dBm and 0dBm for each VOA1 loss.

SET OF PARAMETERS USED IN MODEL CALCULATIONS

Parameter	Discrete R-EAM-SOA	Integrated R-EAM-SOA	Unit
SOA Length	0.088	0.06	cm
SOA Active Area	0.08	0.08	μm^2
SOA Waveguide Loss	25	25	cm^{-1}
Carrier injection eff.	95%	95%	-
Radiative Recomb. coeff.	$1x10^{-10}$	$1x10^{-10}$	cm^3s^{-1}
Auger Recomb. coeff.	$1x10^{-28}$	$1x10^{-28}$	cm^6s^{-1}
Transparency Density	$5x10^{17}$	$5x10^{17}$	cm^{-3}
a_1, Gain Parameter	$2.7x10^{-17}$	$1.7x10^{-17}$	cm^2
C_v, Gain Parameter	$3.44x10^{-6}$	$3.44x10^{-6}$	Hz cm^3
Band gap wavelength	1640	1675	nm
β_{eff}, ASE coupling coeff.	$3.2x10^{-3}$	$3.2x10^{-3}$	-
ASE eff. wavelength	1550	1550	nm
ASE gain param.	$3.1x10^{-17}$	$1.9x10^{-17}$	cm^2
ASE transparency density	$1.2x10^{18}$	$1.2x10^{18}$	cm^{-3}
Input/Output port coupling loss	1.8	1	dB
SOA internal port and EAM insertion loss	8.4	4	dB

Table 4.2. Set of parameters used in model calculations

Figure 4.11(a) shows the measured eye diagrams for the R-EAM-SOA emulated by discrete components (previously shown in Figure 4.7) and Figure 4.11(b) shows the eye diagrams obtained using the numerical model.

It can be seen from the qualitative comparison of the eye diagrams that there is close agreement between the experimental and modelling results. The model is

capable of accurately reproducing the behaviour seen in the experimental eye diagrams under the same conditions. It can also be seen that the model can reproduce the trends of the distortion as a function of input power and internal loss. As the discrete components in the experimental setup were connected with relatively long fibre pigtails, it was necessary to account for this delay by adding a propagation delay between the SOA and the R-EAM in the model. The lengths of the fibre pigtails used in the experimental setup resulted in a single pass delay between the SOA and R-EAM of approximately 30ns. To highlight the effect this delay had on the eye diagrams the model can also be used to estimate the performance of an integrated device with the same SOA and internal loss characteristics of the emulated device, but with a propagation delay of 1ps. This delay is representative of the propagation through the R-EAM section in an integrated R-EAM-SOA. Figure 4.12 shows the modelled eye diagrams for an integrated R-EAM-SOA with the same characteristics as the emulated device but with an internal delay of 1ps.

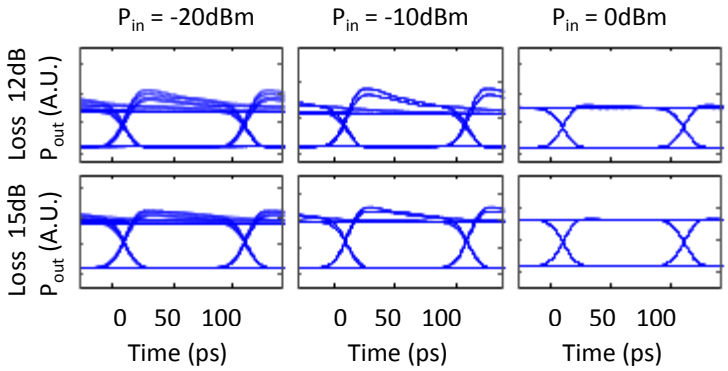

Figure 4.12. Modelled eye diagrams for the emulated R-EAM-SOA with a 1ps delay between the SOA and R-EAM for VOA loss of 12dB and 15dB and input powers of -20dBm, -10dBm and 0dBm.

It can be seen that with an equivalent VOA1 loss of 12dB the traces are more open and better defined when compared to those in Figure 4.11(b). In the modelling, a degradation of the eye diagrams is noticed as the internal delay between the SOA and R-EAM exceeds 1 bit period. This means that the input carrier is experiencing pattering in the SOA by a different symbol of the sequence from the one that will

modulate it in the R-EAM. The effect of this is that the patterning distortion traces are spread more uniformly and tend to close the eye diagram more as can be seen in Figure 4.11(b). This effect of the long internal delay is more difficult to identify in the experimental eyes as the receiver noise also broadens the traces, this can be seen in Figure 4.11(a). Figure 4.12 also shows modelling results for an R-EAM-SOA with a VOA1 loss of 15dB (the internal delay of 1ps is maintained also), here it can be seen that the eye diagrams are clearly open and only show small signs of patterning.

The numerical model was then used to model the integrated R-EAM-SOA which was studied experimentally. However for the integrated device the model parameters cannot be easily measured due to the fact that the SOA and EAM sections cannot be probed independently (nor unidirectionally as is the case for the discrete SOA). Instead, the model parameters must be estimated using device design parameters specified by the manufacturer. The G_0 for the integrated device was estimated to be approximately 11dB at a wavelength of 1550nm and an SOA bias current of 100mA. The overall internal loss for the device was estimated to be approximately 4dB.

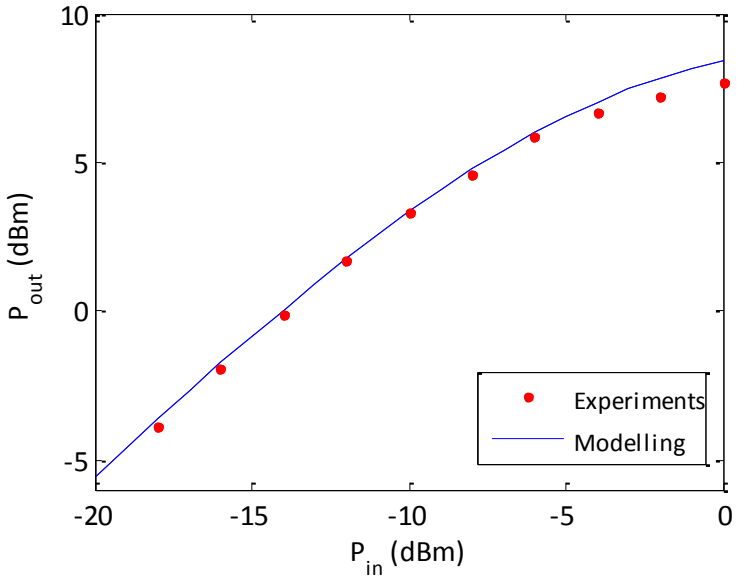

Figure 4.13. Output power versus input power for the integrated R-EAM-SOA.

The parameters for the integrated R-EAM-SOA which could not be measured directly were either derived from scaling of the parameters from discrete devices with similar design or by fitting with the experimental measurements. The full list of the parameters values used to model the integrated device can also be found in the Table 4.2. Figure 4.13 shows the results for the modelling of the output power versus input power (blue line) compared to the experimental measurements on the integrated R-EAM-SOA (red dots). The wavelength used was 1550nm, the SOA bias was 100mA and the R-EAM was modulated at 10Gb/s with NRZ data (as in Section 4.1).

Again, it can be seen in Figure 4.13 that there is good agreement between modelling and experimental measurements for the integrated R-EAM-SOA. In this case the model is able to accurately reproduce the different behaviour seen in the experimental measurements using the integrated device, where no output power clamping was present over the input power range which was studied.

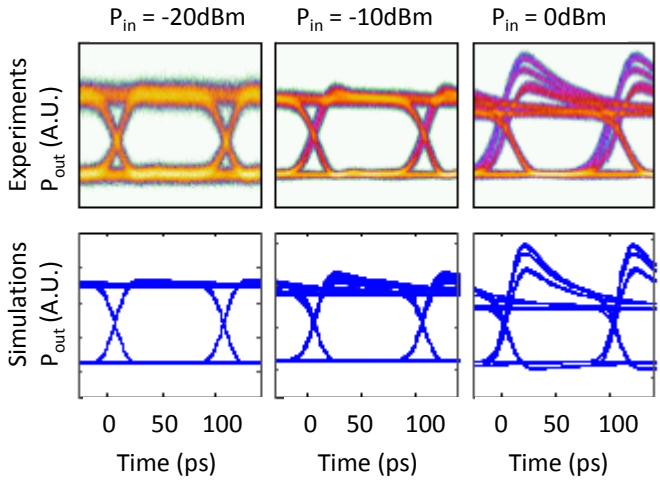

Figure 4.14. Measured and modelled eye diagrams for the integrated R-EAM-SOA.

The model was then used to obtain eye diagrams for the integrated R-EAM-SOA using the same device characteristics, wavelength and SOA drive current as in the output-input power study. The chosen input powers to the R-EAM-SOA were -

20dBm, -10dBm and 0dBm. Figure 4.14 shows the modelled eye diagrams compared to the eye diagrams measured experimentally (shown previously in Figure 4.4). It can be seen that close agreement between experiments and modelling is also found in this instance. The patterning distortion seen in the measured eye diagrams is being closely reproduced by the model over the wide range of input powers which were investigated.

It should be noted that in the modelling presented in this thesis the EAM is assumed to be linear in the operation region of interest and it is modelled as a loss, dependent on the driving voltage. The wavelength dependence of the absorption is also neglected for simplicity. Despite these simplifications the overall R-EAM-SOA model provides results in extremely good agreement with the characteristics derived experimentally over a wide range of conditions, proving that the assumptions made are valid.

The patterning distortion which is introduced by the R-EAM-SOA emulated by discrete components can be easily explained in the extreme cases in terms of input powers and internal loss, if the SOA is considered as a lumped saturable gain. When the internal losses are low the gain saturation is dominated by the modulated backward signal in the SOA. The patterning distortion that would already be generated in this case is increased by the patterning added to the input carrier in the first pass through the SOA. As the input power increases, the forward signal starts to become comparable to or higher than the backward travelling signal and this clamps the carrier concentration. This effectively reduces the pattering as can be seen in the eye diagram for 0dBm and VOA1 loss of 3dB (shown in Figure 4.4). At the other extreme when the internal loss is high, for example in the case where the VOA1 loss is 12dB or higher (Figure 4.4 and Figure 4.12), the eye diagrams are showing little or no patterning distortion over the range of powers examined. For high powers this is also easily explained. The unmodulated forward signal passing through the SOA has, on average, a higher power than the modulated backward signal passing through the SOA. The forward signal therefore clamps the carrier concentration which in turn reduces the patterning distortion. However, in situations where the input power is low, for example the case of -20dBm, or for

situations where the internal loss is of a mid-value, for example 9dB VOA1 loss, the average powers of the unmodulated carrier and the modulated signal are comparable. Despite this the eye diagram still shows little patterning distortion as can be seen in Figure 4.11(a).

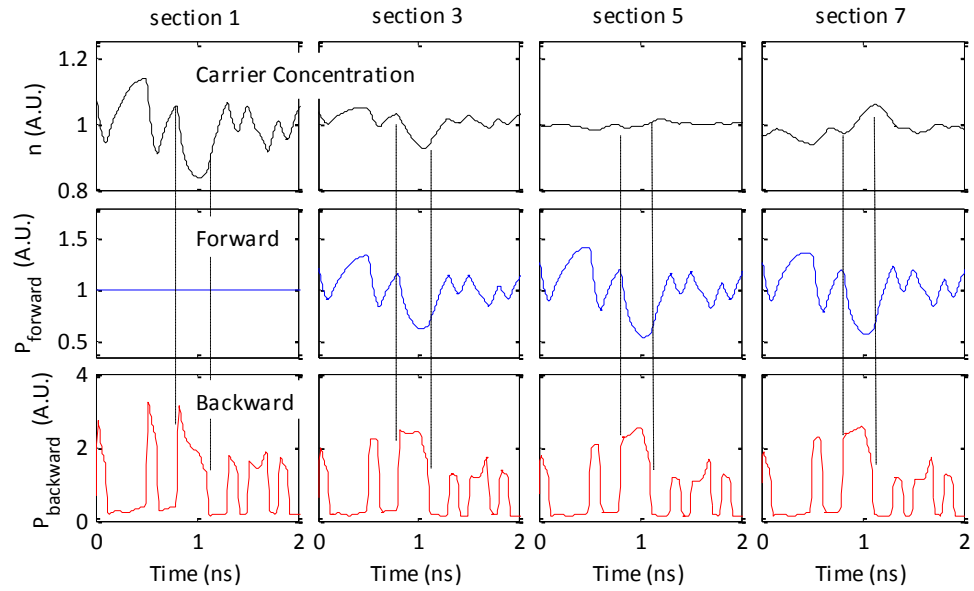

Figure 4.15. Segment of the modelled evolution in time in various positions along the length of the SOA of the normalised carrier distribution, normalised power of forward and backward travelling optical signal for the emulated R-EAM-SOA.

In order to understand this case it is necessary to examine the carrier dynamics inside the device using the time domain model. Figure 4.15 shows the evolution of the normalised carrier concentration as a function of time for a portion of the PRBS sequence for the emulated R-EAM-SOA. The input power to the emulated R-EAM-SOA was -10dBm, the VOA1 loss was 9dB and the R-EAM was modulated at 10Gb/s with NRZ data (2^7-1 PRBS). For these simulations the SOA was subdivided into 7 sections and the results for section 1, 3, 5 and 7 are presented in Figure 4.15. The plot has been normalised to the time averaged carrier concentration in each section. This was done in order to show the variations in the carrier concentration clearly using a common scale for all sections.

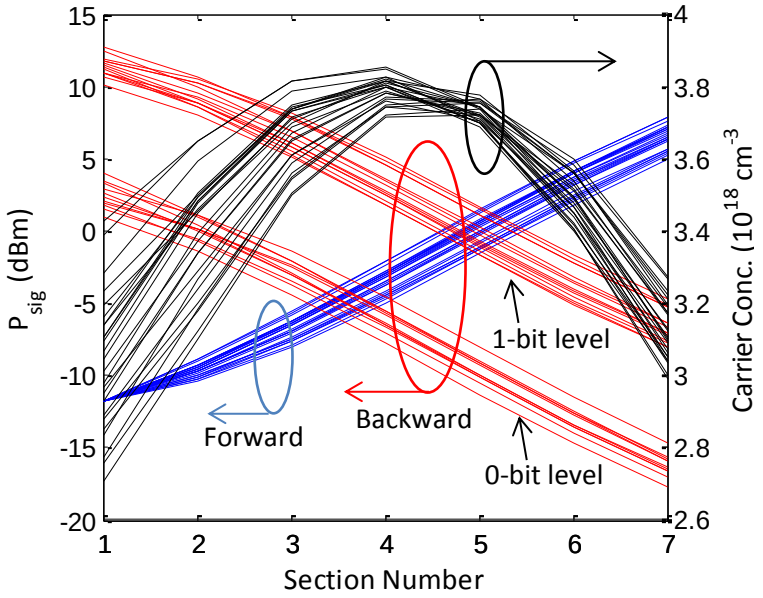

Figure 4.16. Segment of the modelled evolution in time in various positions along the length of SOA of the carrier concentration and power of the forward and backward travelling signal

Figure 4.15 also shows a segment of the time evolution of the forward and backward travelling signals at the output interface of the sections, these are also normalised to their time averaged value. Figure 4.16 shows the absolute power levels sampled at the mid-point of the PRBS symbols as a function of the section inside the SOA for both forward and backward travelling signals. The multiple traces represent the patterning at the symbol mid-point for all symbols in the sequence and clearly show the effect of the modulation of 0 (lower traces) and 1 (upper traces) symbols on the two separate groups of traces for the backward signal. It can be seen that from this plot that most of the patterning is imprinted on the forward travelling signal in the middle sections of the SOA and that the patterning remains of similar magnitude as the modulated signal propagates in the sections close to the R-EAM (sections 3 to 7). This can also be inferred from Figure 4.15.

Figure 4.16 shows that the modulated signal is strongest in the first section of the SOA, near the input and output facet. This creates a patterning effect in the carrier concentration with sign opposite to the modulation pattern. The patterning of the

carrier concentration modulates the gain of the device and therefore the forward travelling signal, which as it travels through the SOA, is also modulated with the inverse of the modulation pattern. As the forward signal travels through the SOA it is also amplified and in the sections towards the R-EAM its power is higher than the modulated signal travelling backwards (Figure 4.16). Therefore it dominates the pattering of the carrier concentration, which has in this case the same sign as the modulation pattern. After the optical signal is modulated in the R-EAM the modulation of the gain in the SOA sections close to the internal interface creates a distortion, which is opposite to the one experienced in the sections close to output facet, effectively removing some of the patterning that was imprinted on the forward signal. It is only in the region close to the output (section 1) that the modulated signal power is high enough to further increase the patterning distortion.

The behaviour of the integrated device is closer to that of a single pass SOA because of the low internal loss (estimated to be 4dB) and the low G_0 (estimated to be around 11dB for single pass at 1550nm and 100mA bias current). Because of the low gain the SOA is only saturated when the input power is close to 0dBm. This results in patterning distortions being introduced. Using the model it can be estimated that the gain clamping regime for this device could only be accessed for input powers around +5dBm. It is also only for those higher powers that the integrated device would show the patterning reduction seen in the emulated R-EAM-SOA.

4.5 NOISE REDUCTION

Another interesting effect which has been demonstrated using both SOAs and R-EAM-SOAs is the reduction of the noise present on the input optical carrier. This has been shown in the case of residual modulation present in the carrier [76] and in the case of Rayleigh backscattering mixing with the carrier [85]. The noise reduction is caused by the noise squeezing effect in the saturated SOA which was outlined in Chapter 3.

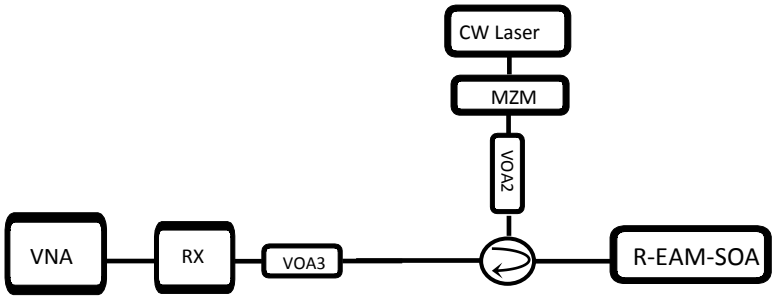

Figure 4.17. Experimental setup to measure low frequency noise reduction using integrated R-EAM-SOA

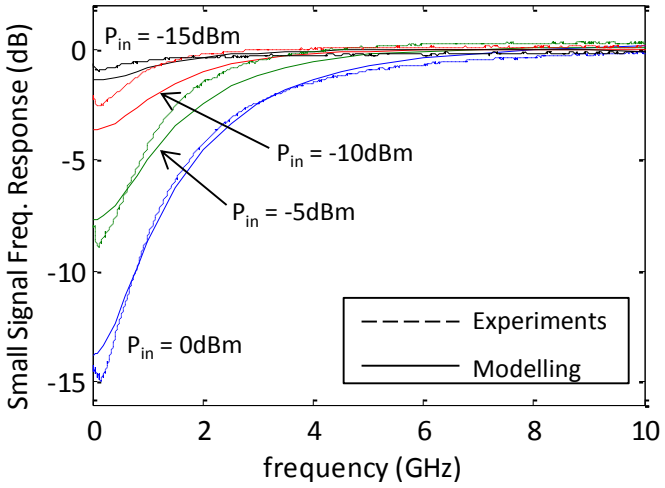

Figure 4.18. Small signal frequency response for the integrated R-EAM-SOA, measured (dashed lines) and modelled (solid lines).

As SOA saturation is required for this noise squeezing effect, the benefits are only accessible in a region where the output signal from a single pass SOA would suffer from patterning distortion. The advantage of an R-EAM-SOA compared to a single pass SOA is that the noise reduction can be obtained without the patterning distortion, provided that the internal loss and the SOA gain are optimised.

Figure 4.17 shows the experimental setup used to demonstrate the noise reduction effect using the latest version of the integrated R-EAM-SOA. A CW carrier with a wavelength of 1550nm is amplitude modulated with a small signal modulation by a MZM, the signal is then passed through the R-EAM-SOA, before being detected by a

high speed receiver. The frequency response is then measured using a vector network analyser (VNA). The R-EAM is biased in full transmission and the SOA bias was 100mA. The frequency response was measured for an input power range to the R-EAM-SOA of -15dBm to 0dBm. The dashed lines in Figure 4.18 show the plot of the small signal frequency response measured using the experimental setup.

The low frequency noise reduction effect can be clearly seen as the input power to the R-EAM-SOA is increased. Almost no reduction of the frequency response was seen for an input power of -15dBm but as the input power is increased and the SOA begins to saturate a reduction in the response can be seen with approximately 15dB of reduction achieved when the input power is set to 0dBm. Figure 4.18 also shows the frequency response calculated for the integrated device using the numerical model (solid lines). A similar schematic to that shown in Figure 4.17 is implemented using the model, with the same wavelength and bias conditions for the SOA and R-EAM. However in the case of the numerical model the frequency response is obtained by applying a small signal (1%) sinusoidal tone to the optical carrier and calculating the variation of the modulation index on the output signal as a function of the tone frequency. Again, good agreement can be seen between the numerical model and experimental results, both in terms of the shape and the magnitude of the frequency response. Comparing these results with the eye diagrams in Figure 4.14 it can be seen that the noise reduction effect can only be obtained for input powers where the device is suffering from patterning distortion and hence with this device design choice, in terms of SOA gain and internal loss, the noise reduction is not usable in a practical application.

The experimental setup shown in Figure 4.17 was then modified by removing the integrated R-EAM-SOA and replacing it with the discrete components that form the emulated R-EAM-SOA. The small signal frequency response was then measured for a range of input powers to emulated R-EAM-SOA. In this case however the small signal frequency response measured experimentally showed a large ripple due to the interaction of the SOA nonlinearity and the long cavity created by the fibre pigtails. Unfortunately for this measurement the discrete devices do not correctly emulate the behaviour of an integrated R-EAM-SOA and the noise reduction effect

cannot be demonstrated experimentally. Similar ripple was also found when the numerical model was used to estimate the noise reduction effect of the emulated R-EAM-SOA using the same delay found in the experiments. Despite the limitations of the experimental setup in this instance the numerical model can still be used to estimate the performance of an integrated device with similar characteristics, in terms of SOA gain and internal loss, to the emulated device, if the internal delay is set to a value close to what would be present in an integrated device.

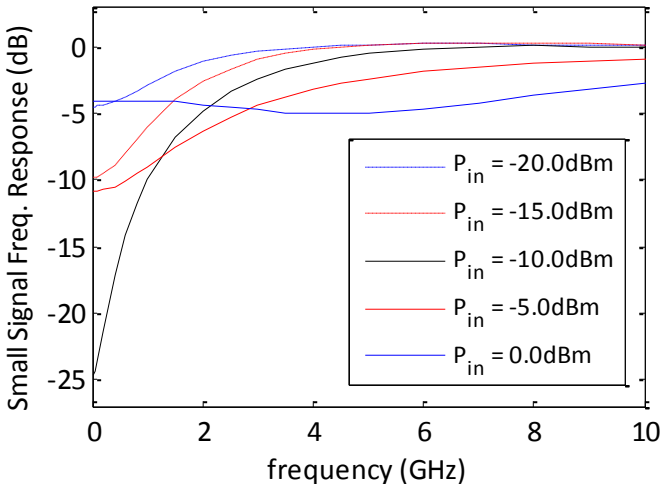

Figure 4.19. Modelled Small signal frequency response for the emulated R-EAM-SOA with an internal delay of 1ps.

Figure 4.19 shows the frequency response obtained using the model, a wavelength of 1550nm, an SOA bias of 100mA was used and the SOA had a single pass input saturation power ($P_{sat,in}$) of ~-11dBm. The R-EAM was biased in full transmission. The input power range was from -20dBm to 0dBm in 5dB steps, the VOA loss was set to 12dB and the internal delay was set to 1ps in the model.

It can be seen from the plot that a substantial reduction of the small signal frequency response at low frequencies can be achieved for some input power values. The most significant reduction is obtained for an input power to the R-EAM-SOA of -10dBm where low frequencies are supressed by up to 25dB. A smaller, yet still substantial reduction of 10dB or more can be obtained for input powers in the -15dBm to -5dBm range, which also corresponds to the region around the peak in

output power for this device. It is important to note that, in contrast to the integrated R-EAM-SOA, the reduction of the small signal frequency response at low frequencies which would correspond to the noise reduction effect can be obtained for a device of this configuration with only a small amount of patterning distortion.

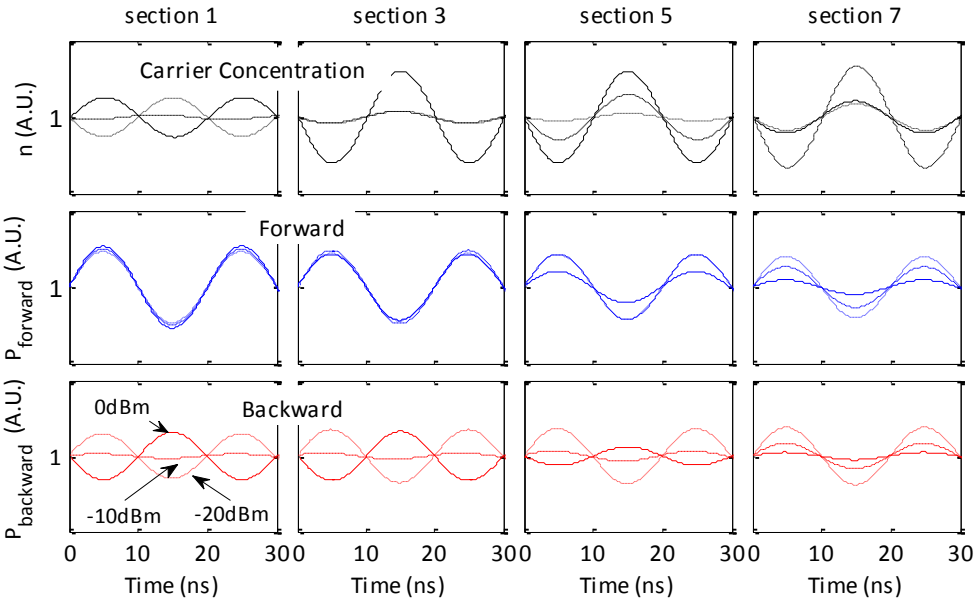

Figure 4.20. Segment of the modelled evolution in time in various positions along the length of the SOA of the normalised carrier concentration, normalised power of forward and backward travelling optical signal for the emulated R-EAM-SOA under small signal sinusoidal modulation at 50MHz. Input powers of -20dBm (dotted line), -10dBm (dashed line) and 0dBm (solid line).

This can be observed in Figure 4.11. As this device is pushed deeper into saturation the noise reduction at low frequencies is reduced. This can be seen for an input power of 0dBm in Figure 4.19. This is an interesting effect which is created by double passing the SOA and by the different saturation induced by the forward and backward travelling signals.

In order to better understand how the small signal modulation of the carrier is affected, for the different input powers, as it travels through the SOA it is interesting to study the evolution in time along the length of the SOA of both the carrier concentration and the forward and backward travelling signals. Using the

emulated R-EAM-SOA configuration (with 1ps internal delay) plots of the normalised carrier concentration, forward and backward propagating signals for section 1, 3, 5 and 7 of the SOA for small signal modulation at 50MHz are generated and shown in Figure 4.20. The VOA1 loss is fixed at 12dB and input powers of -20dBm (dotted lines), -10dBm (dashed lines) and 0dBm (solid lines) are shown.

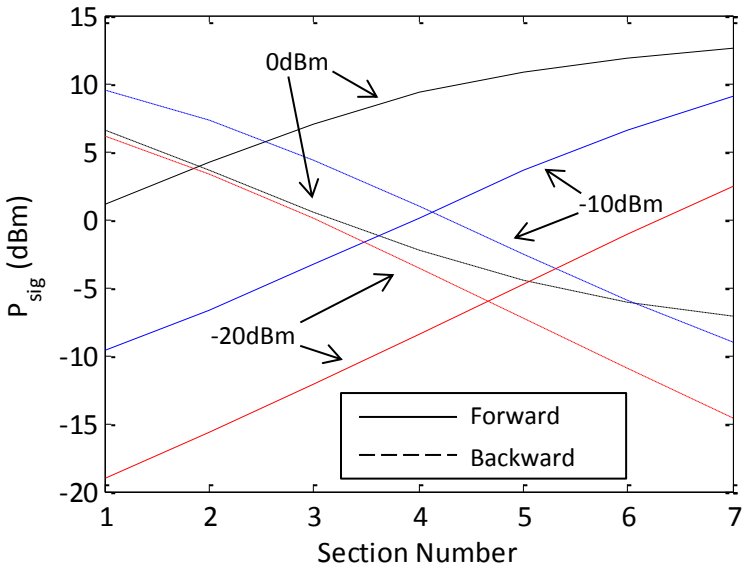

Figure 4.21. Segment of the modelled evolution in time in various positions along the length of the SOA of the absolute forward and backward travelling signal.

The model is also used to estimate the absolute powers along the length of the SOA for both the forward (solid lines) and backward (dashed lines) signals using the same input power range, these are shown in Figure 4.21.

First focusing on the signal for low input power, it can be seen that at low input power the signal creates a noticeable modulation of the carrier concentration near the output facet of the SOA only (section 1), where the power level of the backward signal is higher. This can be seen in the dotted lines of Figure 4.20. Because of this the small signal modulation of the carrier is only slightly attenuated in the sections near the output facets and therefore we only see a small reduction of the frequency response in Figure 4.19 for an input power of -20dBm.

The next input power of interest is -10dBm (dashed lines). In this case the maximum modulation of the carrier concentration is obtained near the internal facet of the SOA (section 7). This results in the small signal modulation being strongly attenuated for both forward and backward signals as can be seen in sections 5 and 7. It should also be noted that, although the power of the backward signal causes saturation in the region near the output facet (section 1), it does not modulate the carrier concentration as the attenuated small signal modulation is negligible. This can be seen by the significant low frequency suppression in Figure 4.19 for an input power of -10dBm.

Finally looking at 0dBm (solid lines), which was the highest input power studied. In this case the forward signal causes a strong modulation of the carrier concentration in the middle of the SOA (sections 3 and 5). When the forward signal reaches the internal interface (section 7) the small signal modulation has already been attenuated. The backward signal on the other hand is modulated by the carrier concentration variation as it travels through the SOA. The variation of the carrier concentration has an opposite sign compared to the input small signal modulation. Near the output facet of the SOA (section 1) the backward signal power is high enough to modulate the carrier concentration, and the opposite phase can be seen compared to the forward signal. Because the backward signal is re-modulated as it travels through the SOA the attenuation of the small-signal frequency response is effectively reduced and results in the poor suppression of low frequencies seen in Figure 4.19 for an input power of 0dBm.

4.6 CONCLUSION

The counterintuitive behaviour demonstrated by a gain saturated integrated R-EAM-SOA [12] prompted a detailed study of the behaviour of this type of device using both experimental measurements and modelling. An initial experimental characterisation of an available integrated R-EAM-SOA showed the device was not operating in a regime where the output power clamping and patterning suppression, seen previously, could occur for the required range of input power. As it was not possible to adjust any of the important parameters in the integrated

device an alternative device was required to continue the experimental investigation. An emulated R-EAM-SOA was then built using discrete components where the behaviour of the device could be analysed in more detail by allowing the adjustment of the internal loss, in a way which was not possible with a fully integrated device. The experimental investigation using the emulated R-EAM-SOA indicated that the value of the internal loss was a key factor in order to achieve the output power clamping effect and also the highly desirable patterning suppression effect. The models described were used to obtain insight into the behaviour seen experimentally in this type of device and in particular they can help to explain the reason for the peak in the output power as a function of the input power and also why patterning distortions are supressed at high input power. The numerical model was also used to analyse the noise squeezing effect in the SOA section, an important attribute which can be used to reduce the noise present on the input carrier.

Using the numerical models it was possible to confirm that these effects are related to the amount of internal loss present after the SOA section and on the SOA section single pass gain. The experimental and modelling results compared here for different SOA single pass gain and internal loss show that, against intuition, a high gain and high internal loss allow these devices to operate in a region of output power clamping and also with low patterning distortion. Under these conditions the noise suppression is also accessible at low input carrier power and in a region of operation with moderate patterning distortion. This finding suggests a previously unrecognised beneficial trade-off in the design of this class of device, where additional internal loss can actually improve performance. This is at odds with the usual assumptions made for integrated photonic devices, where minimisation of internal loss is considered desirable for improved efficiency and performance.

The experimental and modelling results presented here indicate that a choice of SOA single pass gain of approximately 20dB and a total internal loss also of approximately 20dB allows the three beneficial effects described to be obtained for a range of input carrier powers from -15dBm to 0dBm, which corresponds to the

range of input carrier powers usually assumed in carrier distributed PONs [17], [86]. While the emulated R-EAM-SOA is not a practical solution in real network scenario and the integrated R-EAM-SOA used here did not allow changes to the internal loss, it is feasible to fabricate such an integrated device with variable loss. One approach would be a split contact SOA section, where altering the drive current to the second contact would alter the attenuation properties of that SOA section. Another possibility is the addition of a second (unmodulated) EAM section between the SOA and R-EAM. Here changes in the bias voltage would allow changes to absorption properties of the EAM and thus provide a controllable loss.

Despite the understanding obtained with the analysis presented in this chapter a further, more systems oriented, study is also required. In Chapter 5 the emulated R-EAM-SOA will first be studied using a bit error rate analysis to better understand how the changes to VOA1 loss impact on its performance. The validated numerical model will then be used to study how changes to the SOA gain in an R-EAM-SOA as well as the internal loss affect its performance. Using the numerical model in combination with a system simulation the design parameter space is explored and an optimum device design is proposed for use as the upstream transmitter in a carrier distributed long reach PON.

5

Design Optimisation of R-EAM-SOA for Long Reach Carrier Distributed Passive Optical Networks

In this chapter the focus of the R-EAM-SOA analysis moves towards the performance of the device in a network scenario and specifically how the device can be optimised for use in a carrier distributed passive optical network (PON). The R-EAM-SOA has shown strong potential for use as the upstream transmitter in carrier-distributed long reach PONs [12], [13], [16]. It was shown in Chapter 4 that gain saturated integrated R-EAM-SOAs have demonstrated interesting behaviour, where the output power of the device is clamped around a maximum and patterning distortions are supressed. This happens if the device is correctly configured with the right amount of internal loss to complement the gain of the SOA. The major advantage of this output power clamping is that it can reduce the burst to burst dynamic range of the upstream signal in a carrier distributed PON [17]. Now using the validated model this dynamic range compression can be demonstrated and explained in detail by exploring a wide parameter space which is not possible with the experimental devices.

Both the experimental study and modelling of the R-EAM-SOA emulated using discrete components have shown that the output-input power characteristics and position of the output power peak of the device can be controlled by changing the VOA loss between the SOA and R-EAM [18]. Eye diagrams were also used to show visually how changes to the VOA loss affect the levels of patterning on the signal. The first step in this Chapter is to carry out bit error rate (BER) measurements on the experimental device in order to fully understand how the VOA loss changes

affect its performance and to find the optimum VOA loss for this particular emulated R-EAM-SOA. These results will then be used to build a validated simulation setup to estimate the BER for modelled devices.

The experimental analysis of the R-EAM-SOA was limited to devices which had fixed gain, therefore only changes to the loss could be studied to date. The next step in this Chapter is to use the numerical model validated in chapter 4 to model R-EAM-SOA devices which have different gain SOA sections, while also adjusting the internal loss. It will be demonstrated that careful design of both the SOA gain and internal loss can provide an optimum balance between dynamic range compression, output power maximisation and patterning distortion reduction.

The validated system simulation is then used to estimate the performance of the modelled R-EAM-SOAs in a network scenario and the design parameters are proposed which give optimum performance for an R-EAM-SOA operating as the upstream transmitter in a carrier distributed long reach PON. The analysis carried out here will also help to outline the design parameters in terms of SOA gain and loss tuning range required for the design and fabrication of an integrated R-EAM-SOA with a split contact SOA section or additional EAM section which would allow loss optimisation of an integrated device.

5.1 DISCRETE R–EAM–SOA BIT ERROR RATE MEASURMENTS

The experimental setup for BER measurements using the emulated R-EAM-SOA is shown in Figure 5.1. The R-EAM was modulated at 10Gb/s with 3Vpp NRZ data (2^{31}-1 PRBS) superimposed on a DC bias, which was set to a value of -1.4V.

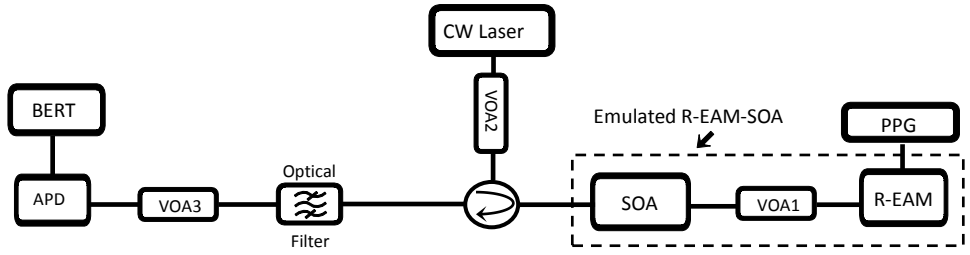

Figure 5.1. Experimental set up. PPG: Pulse pattern generator, APD: Avalanche photodiode, PC: Polarisation controller

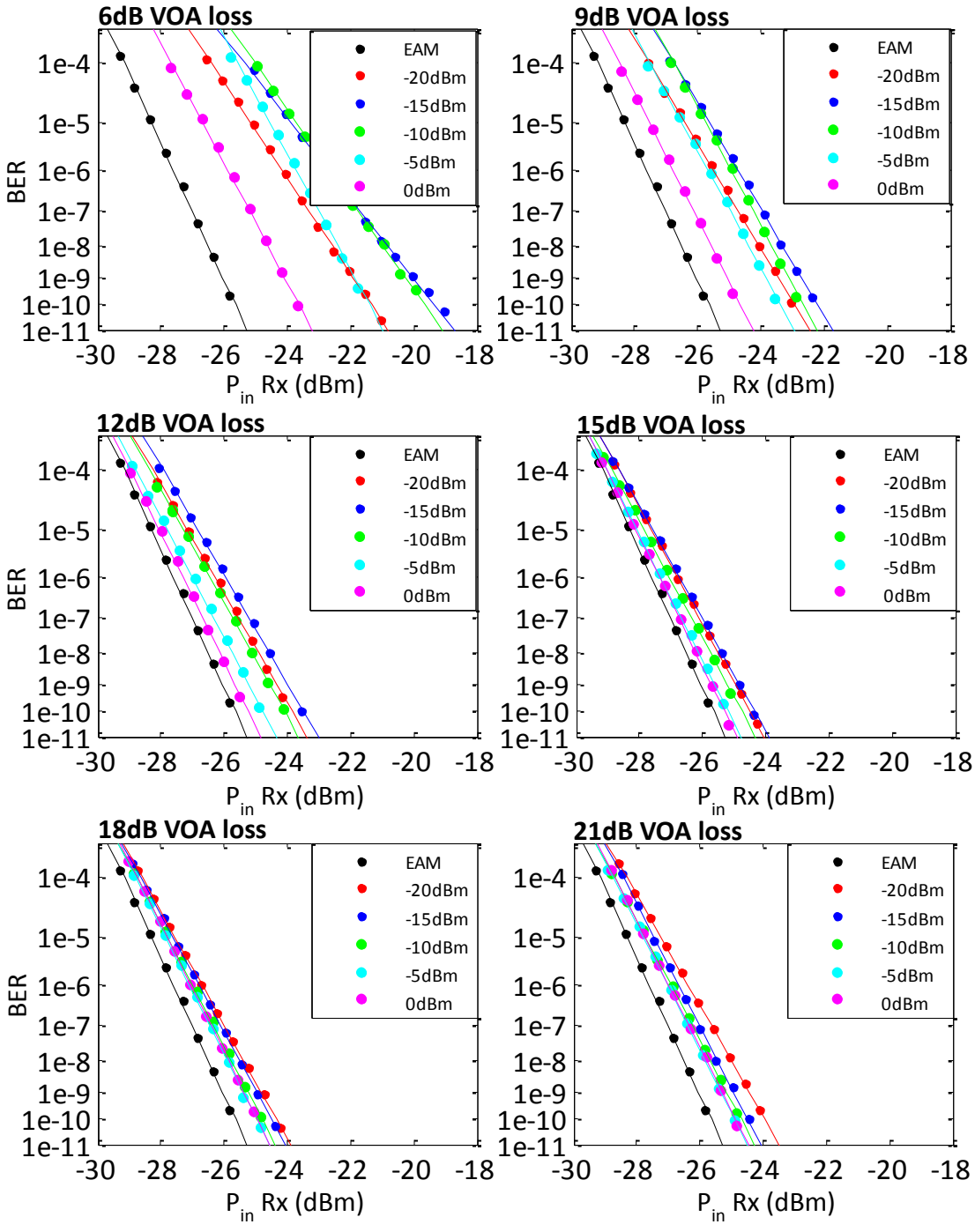

Figure 5.2. BER versus received power for R-EAM only and emulated R-EAM-SOA for indicated VOA1 losses and SOA input powers.

A continuous wave (CW) optical carrier with a wavelength of 1550nm was generated by a tuneable laser and injected into the emulated R-EAM-SOA via a circulator. The output signal BER was measured using the 10Gb/s APD receiver (−26dBm sensitivity at 10^{-9} BER) coupled to an error detector. A 1nm bandpass filter tuned to 1550nm was used to reduce the amplified spontaneous emission (ASE) falling on the receiver. As outlined in chapter 4 the variable optical attenuator (VOA) placed between the SOA and R-EAM is vital [18] as this emulates the internal loss which would be present between the SOA and R-EAM sections in a real device. Again, this will be called VOA1 for clarity.

Before proceeding with the BER measurements on the emulated R-EAM-SOA a BER measurement was first carried out on the R-EAM only for comparison purposes. As the SOA is not present, this measurement will be free from any impairments caused by the SOA and will be used for comparison with all the results using the SOA in this section [17]. To measure the BER of the R-EAM alone, the SOA and VOA1 in Figure 5.1 were removed. The input power to the R-EAM was fixed at +5dBm for the measurement and the input power to the APD receiver was swept to generate a plot for BER versus input power to the receiver for the R-EAM.

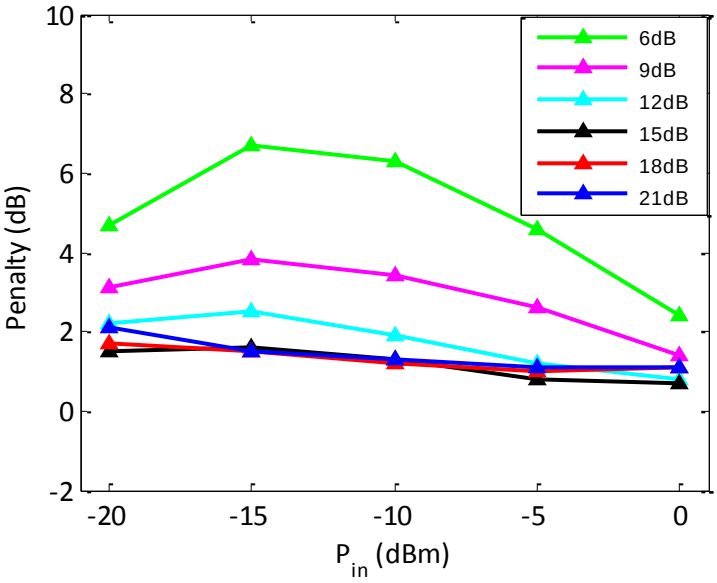

Figure 5.3. Penalty versus R-EAM-SOA input power for VOA1 loss range of 6dB to 21dB.

The SOA and VOA1 were then reinserted into the setup and BER measurements were taken for VOA1 losses of 6dB to 21dB in 3dB steps with the input power to SOA swept from -20dBm to 0dBm in 5dB steps. The input power to the receiver was swept for each SOA input power and VOA1 loss and the results were used to plot BER as a function of received power. Figure 5.2 shows the plots of BER versus received power for the various SOA input powers and VOA1 losses, the results for the R-EAM only are also included for comparison. Figure 5.3 shows the plot of power penalty at a BER of 10^{-10} versus input power to the R-EAM-SOA. The penalty is calculated from Figure 5.2 using the R-EAM only as reference.

Starting with the lowest VOA loss setting of 6dB the performance of the emulated R-EAM-SOA is poor, large penalties compared to the R-EAM can be seen for all input powers with a worst case penalty of approximately 6dB at a BER of 10^{-10}. When the loss is increased to 9dB an immediate improvement can be seen in performance, however penalties are still relatively high in this case with a worst case penalty of approximately 4dB. As the attenuation of VOA1 is increased again to 12dB the performance of the emulated R-EAM-SOA improves considerably with a penalty of less than 3dB for all SOA input powers. Further increasing the loss to 15dB gives a small improvement with all penalties now less than 2dB. Increasing the VOA1 loss to values greater than 15dB shows little or no improvement as patterning has been almost completely eliminated, this can be seen in the eye diagrams in Figure 4.7 of Chapter 4 [18]. When the VOA loss reaches 18dB and 21dB the penalty over the R-EAM begins to increase again for low input powers to the SOA. This increase in penalty is due to a slightly degraded OSNR which is caused by a decrease in the output power due to the high VOA1 loss [18].

Taking into account the patterning impairments when VOA1 losses are low and the onset of OSNR penalties when VOA1 losses are very high, a VOA1 loss in the 12dB to 15dB range was the optimum setting for this emulated device, thus giving an approximate overall loss of 21dB to 24dB when the VOA1 loss is added to R-EAM insertion loss and SOA coupling loss.

The behaviour of R-EAM-SOAs has been studied both experimentally using an emulated R-EAM-SOA [17] and using a numerical model [18]. The impact this

behaviour has on the experimental BER performance of the device has been also been demonstrated. The next step is to use the emulated R-EAM-SOA experimental BER results to help design an accurate system simulation which can estimate the BER of the devices which were modelled in Chapter 4 and devices which will be modelled in later sections of this chapter.

5.2 BER ESTIMATION

The ability to accurately estimate BER for the discrete R-EAM-SOA is an important step in completing the study of the experimental device. It is also important to have a validated method for simulating BER so that the system performance of the numerically-modelled devices can also be studied. The optical communications system simulation software VPI transmissionMaker 8.6 [87] was chosen to simulate the system performance of the R-EAM-SOA as the VPI environment offers a comprehensive library of component and system tools. VPI also allows co-simulation with Matlab, which is very advantageous as it allows the already validated Matlab based numerical model for the R-EAM-SOA [18] to be integrated into the VPI environment. VPI's well-established simulation tools and techniques can then be used to build accurate system simulation schematics.

The simulated receiver is a key component in enabling accurate BER estimation and in particular its ability to correctly estimate the BER of signals with very different levels of patterning. Therefore before the BER estimates could be carried out using the modelled version of the emulated R-EAM-SOA, the simulation tools needed to be validated.

In order to generate valid BER estimates the performance of the simulated receiver must closely match that of a real receiver. In this characterisation a PIN receiver with a bandwidth of 12.5GHz is used rather than an APD receiver. The simulated receiver has a number of important parameters which are the thermal noise, responsivity and post-detection filter bandwidth. The other key setting in the simulated receiver is the BER estimation method and in particular its treatment of inter-symbol interference (ISI). In measurements carried out in this section the OSNR will be kept high and the thermal noise of the receiver will be the limiting

factor therefore a Gaussian estimator is chosen. Although ISI will not be present in back to back (B2B) when estimating the BER with no SOA, it needs to be taken into account when the SOA is used as patterning effects in the SOA introduce ISI.

If the statistical model used in calculating the BER treats all bits in the sequence as independent in the presence of ISI, this will result in incorrect results. If for example the Q-parameter is being used to evaluate the BER, it assumes a Gaussian noise distribution on both the 1-bit and 0-bit levels and relates the mean values of their levels to their standard deviations [88]. If there is excess ISI this process becomes unreliable due to the assumption that there are only two Gaussian noise distributions.

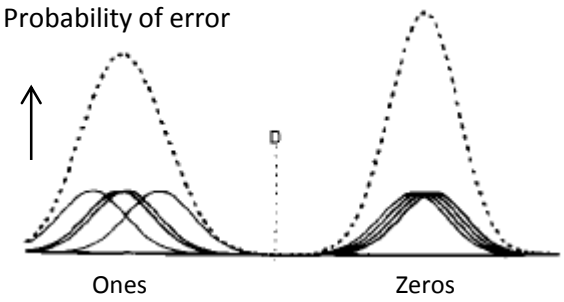

Figure 5.4. Graphical representation of the eight noise distributions and their sum [88].

When ISI is present this assumption is no longer valid and results in the overestimation of standard-deviations and therefore poor values of Q. If it is assumed to a first approximation that the ISI on a bit is strongest from the bit preceding it and following it then it is possible to relate each bit to one of eight unique patterns or meta-symbols. There are four patterns associated with each logical level (e.g. 111, 101 etc) and these can be represented as eight different noise distributions as shown in Figure 5.4. The bits in the sequence are then sorted by pattern and a separate mean and standard deviation can be calculated for each pattern. The different distributions then give the probability of error for that particular pattern, therefore maintaining a Gaussian noise distribution. The total BER is then calculated by adding the contributions of the eight patterns weighted to represent the frequency of each pattern within the original bit sequence [88].

In order to validate the ISI estimator and find the optimum number of pre-bits and post-bits to consider, the ISI pre-bits specify the number of bits preceding the current bit to be considered in the ISI calculation while the ISI post-bits specify the number of bits following the current bit to be considered in the ISI calculation. The initial characterisation was performed using the simpler setup of a Mach-Zehnder modulator (MZM) and an SOA in single pass rather than the R-EAM-SOA. Figure 5.5 shows the simple experimental setup used to obtain BER measurements with the MZM. The most important aspect here is to demonstrate that, with the optimised settings, the receiver in VPI can accurately model the distortions introduced by patterning and thus give accurate BER estimates.

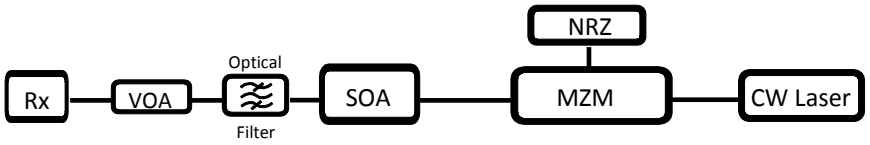

Figure 5.5. Experimental and Simulation schematic setup for receiver characterisation

Before generating BER estimates using VPI, experimental BER measurements were first obtained using the MZM and single pass SOA. These are required to validate the BER estimator. First the BER was measured with no SOA (B2B), this was required as a reference. Measurements were carried out using a combination of a MZM and SOA in single pass for an SOA input power range of -20dBm to -4dBm. The CW input to the MZM was at a wavelength of 1550nm and was fixed at +5dBm. The MZM was modulated at 10Gb/s with an NRZ signal (2^7-1 PRBS), the SOA is operated in single pass with a bias current of 100mA and amplifies the modulated output signal from the MZM before it is detected by the receiver. The BER is then measured by the BERT. Figure 5.6 shows the plot of power penalty at 10^{-9} and 10^{-3} versus input power to the SOA. The penalty is calculated using the B2B measurement as the reference.

An unexpected feature can be seen in Figure 5.6 where some SOA input powers are showing negative penalty compared to the B2B measurement. This result suggests a source of discrepancy in the experimental setup as the BER results in B2B should always be better than results which include the SOA. This is because the effects of

gain saturation and recovery in the SOA and the ASE noise added by SOA can only impair the signal quality not improve it. Therefore the results here indicate that there is some additional distortion in B2B which the SOA is compensating for. Having ruled out the other components in the setup up we believe that the source of this discrepancy is the low frequency response of the input stage of the BERT. The improvement in BER seen for some SOA input powers can be attributed to the frequency response of the SOA as it enters saturation which compensates for the non-ideal low frequency response of the BERT, thus giving the negative penalty seen in Figure 5.6.

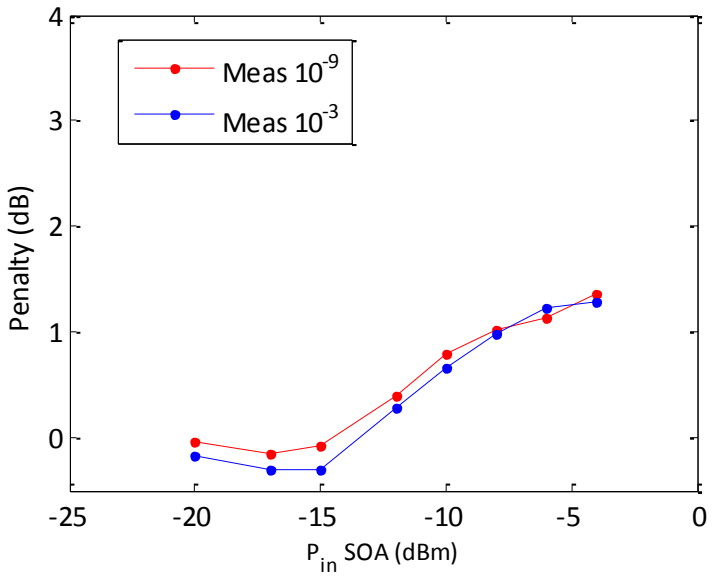

Figure 5.6. Power penalty versus SOA input power for experimental measurements using MZM and single pass SOA.

To validate the BER estimator a simulation schematic was built in VPI which matched the experimental setup shown in Figure 5.5. The first step is to fit B2B estimates from the simulation with B2B results found experimentally by fine tuning the receiver in VPI (thermal noise, responsivity etc). If the B2B results are matched then the estimator should be able to account for the impairments added by the SOA and give close estimates to the experimental BER results for the MZM and SOA combination. The ISI settings are the only receiver setting which should be tuned while the SOA is in use. The simulations were then implemented using the same wavelength, MZM input power and modulation settings as were used in the

experimental setup. The B2B experimental results and B2B simulations were matched by tuning the receiver. BER estimates were then generated for a range of SOA input powers from -25dBm to 0dBm.

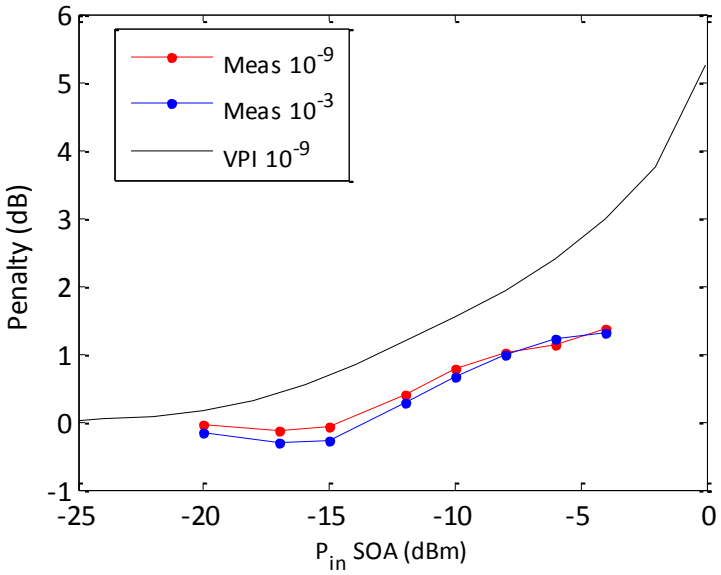

Figure 5.7. Power penalty versus SOA input power for experimental measurements and VPI simulations using MZM and single pass SOA. Standard Bessel LPF used in receiver.

Figure 5.7 shows experimental results outlined previously compared to the power penalty at 10^{-9} versus SOA input power found using the simulation schematic. The optimised ISI settings were 3 pre-bits and no post-bits, as the gain recovery is only affected by the proceeding part of the bit sequence no post bits were required. It is clear from Figure 5.7 that the simulations are not in close agreement with the experimental results and do not show the same negative penalty seen at some SOA input powers in the experiments. The disagreement between the results is because the simulated receiver does not take the BERT frequency response discrepancy into account. Because of this the simulation results have a different trend and are worse than the experimental results for all SOA input powers.

In order to improve the agreement between experimental results and simulations it was necessary to find a way to compensate for the non-ideal BERT frequency response. Experimental results have shown that the MZM and SOA combination, with an SOA input power of -15dBm, were able to overcome the discrepancy in the

frequency response. Therefore the frequency response of the SOA under this input power condition was used to design two custom post-detection low pass filters for the simulated receiver, which would replace the standard Bessel LPF currently used. While it was not possible to find the exact frequency response of the BERT input stage, the use of a custom post-detection filter should help to replicate the conditions found experimentally.

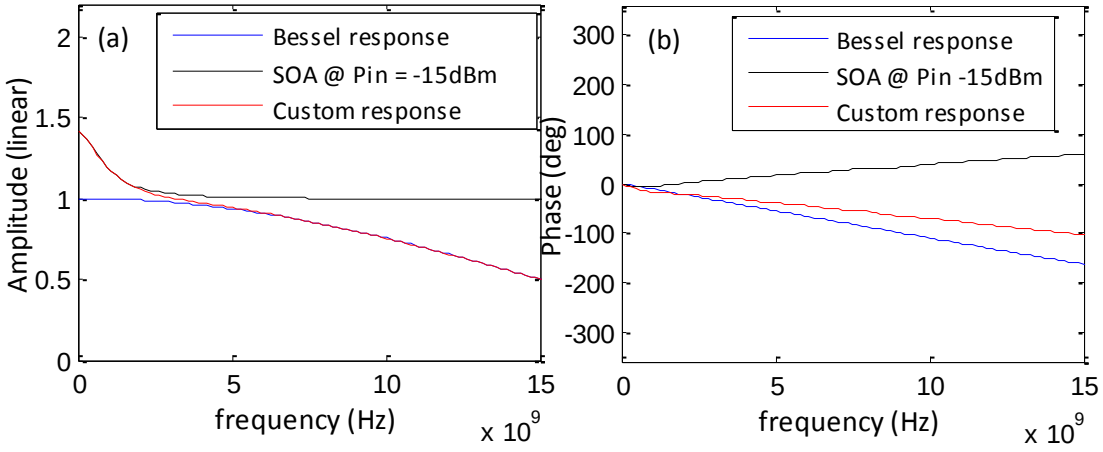

Figure 5.8. (a): Bessel LPF amplitude response, inverted amplitude response of the SOA and the custom amplitude response. (b): Bessel LPF phase response, inverted phase response of the SOA and the custom phase response.

The response of the custom filters was generated by multiplying the frequency response of a standard Bessel low pass filter (LPF) with the inverted frequency response of the SOA at an input power of -15dBm. One filter had a custom amplitude and phase response while the second custom filter used the standard amplitude response of a 12.5GHz Bessel LPF but a custom phase response. Figure 5.8 (a) shows the amplitude response of a 12.5GHz Bessel low pass filter (blue line), the inverted amplitude response of the SOA (black line) and the response generated from their product (red line). Figure 5.8 (b) shows the phase response of a 12.5GHz Bessel low pass filter (blue line), the inverted phase response of the SOA (black line) and the custom phase response (red line).

The Bessel LPF in the simulated receiver was then replaced by the LPF filter with custom amplitude and phase response. The BER was then simulated, first in B2B (no SOA) where the thermal noise and responsivity were again fine-tuned so that the

BER estimates and experimental results were in agreement. The receiver settings were then fixed and the BER was simulated for the MZM and SOA combination. The same process was carried out for the second filter with custom phase response only. Figure 5.9 shows the power penalty versus SOA input power for the experimental results and the simulations using both custom filters.

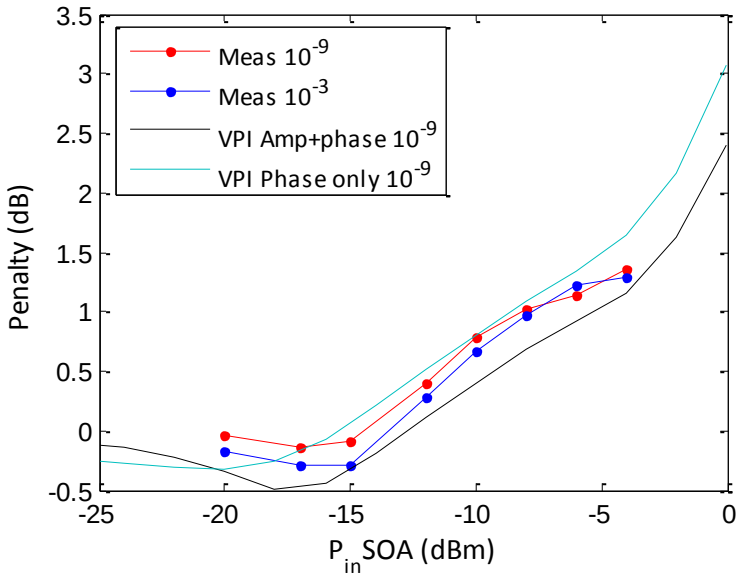

Figure 5.9. Power penalty versus SOA input power for experimental measurements and VPI simulations using MZM and single pass SOA. Custom LPFs used in receiver.

Using the LPF filter with both custom phase and amplitude response a better match can now be found between the experimental results and the simulations especially in the trend of the power penalty which now follows the experimental results much more closely. The negative penalty at some SOA input powers can now also be seen in the simulation results. The optimised receiver settings are shown in Table 5.1. The agreement was not as close when using the filter with custom phase response only, although it still gave a closer match than using a standard LPF Bessel filter. Again it should be noted the real frequency response of the input stage to the BERT is unknown, however these results suggest that the custom filters are able to give a good approximation. This characterisation confirms that the BER estimator, and in particular the ISI estimator in VPI can model the pattering distortion correctly in this situation using a single pass SOA. The next step is to modify the simulated receiver

to model the APD receiver which was used experimentally when acquiring BER measurements with the emulated R-EAM-SOA.

Parameter	value	Units
Thermal noise	10.9	$A/Hz^{1/2}$
Responsivity	0.7	A/W
ISI	3 Pre-bits 0 Post-bits	-

Table 5.1. Optimised PIN receiver settings

5.3 DISCRETE R-EAM-SOA BER SIMULATIONS

Having confirmed that accurate BER estimation of patterned signals can be obtained using VPI the next step was to modify the simulation setup to incorporate the R-EAM-SOA in place of the MZM. However as the experimental results in Section 5.1 were obtained using an APD receiver the receiver module in VPI also needed to be modified so that simulations and experimental measurements could be compared directly. At this point it was also decided to change the estimation method from a Gaussian model to a Chi^2 model. The Chi^2 model is more computationally intensive however as BER estimation will be carried out in situations where the OSNR is degraded due to amplifiers the Chi^2 model was more appropriate.

A similar procedure to that in Section 5.2 was followed in-order to setup the simulated APD receiver. The simulation schematic is shown in Figure 5.10. Firstly BER estimates were obtained for an R-EAM only with no SOA, which was done by deactivating the SOA section in the R-EAM-SOA model. A VPI laser module was used to generate the CW carrier at a wavelength of 1550nm and a PRBS generator and coder driver modules generate a 10Gb/s NRZ electrical drive signal with a PRBS length of 2^7-1, with a rise time of 25ps at a crossing point of 50%.

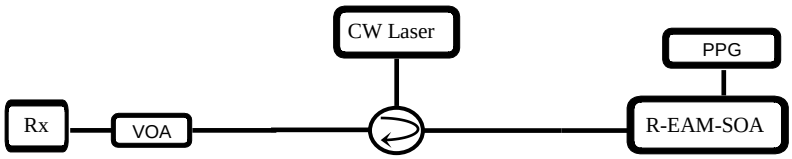

Figure 5.10. Simulation setup for receiver characterisation

This electrical signal was then used to modulate the R-EAM. The receiver module was set as an APD with the responsivity and avalanche multiplier parameters initially set to those outlined in the data sheet for the device used in the experiments. Due to the change in receiver type it was also necessary to test both custom post-detection LPFs (custom amplitude and phase response and custom phase response only). In this instance the response of the filters was generated again to account for the lower bandwidth of the APD receiver (7.5GHz). As in Section 5.2 the parameter settings were fine-tuned in order to best match the performance of the experimental receiver.

Parameter	value	Units
Thermal noise	9.5	$A/Hz^{1/2}$
Responsivity	0.7	A/W
Avalanche multiplier	8	
ISI	3 Pre-bits 0 Post-bits	-

Table 5.2. Optimised APD receiver settings

Figure 5.11 shows the plot of BER versus receiver power using the R-EAM only for both custom LPFs. In contrast to the PIN receiver in Section 5.2, it is the LPF with custom phase only which gives the best fit with the experimental results when the APD receiver is used. Again, as the frequency response of the input stage cannot be measured it is possible that there is a distortion in the phase at low frequencies. Although the effect is small it can still affect the signal. It can also have a different effect on the signals from the different receiver types, which is demonstrated by

the need to use different filters to optimise the APD receiver compared to the PIN receiver.

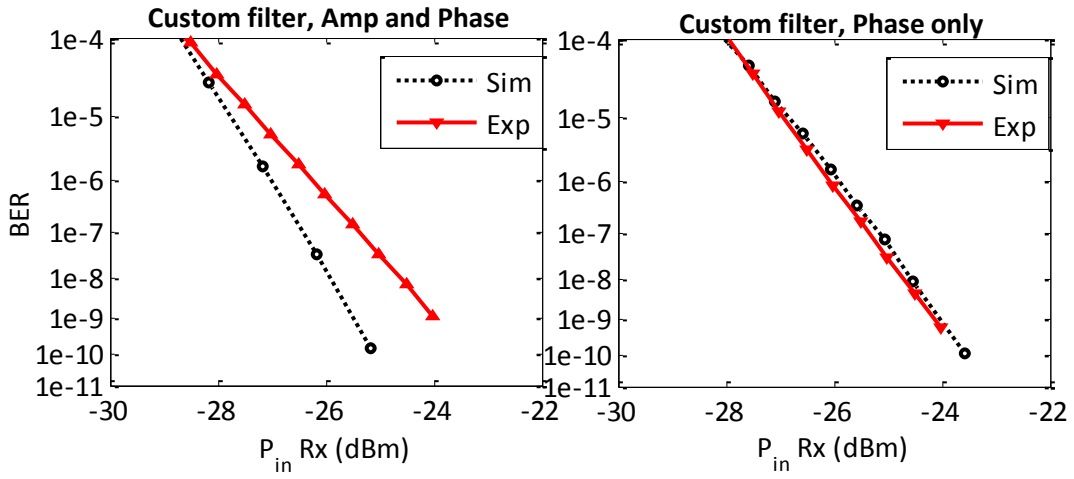

Figure 5.11. BER versus received power for R-EAM only. Both Simulations and experimental measurements are shown.

The receiver settings were then fixed (including the LPF with custom phase only) and the module in Figure 5.10 was set to simulate the full R-EAM-SOA. The optimised receiver settings are shown in Table 5.2. Simulations were then implemented using the same input power and VOA1 losses which were used in Section 5.1.

Figure 5.12 shows an example of two of the simulations using the modelled version of the R-EAM-SOA compared to the experimental results for the emulated R-EAM-SOA. Both are for an input power of -15dBm and with VOA1 losses of 12dB and 6dB. The good agreement between experimental results and simulations show that the patterning distortion is again being modelled correctly and that very accurate BER estimates can be achieved for signals with different levels of patterning using the APD receiver also. Although not shown here similar good agreement is also achieved over the entire input power and internal loss range. The comparison between experiments and simulations validates the receiver and the BER estimator used in the simulations in conjunction with the R-EAM-SOA.

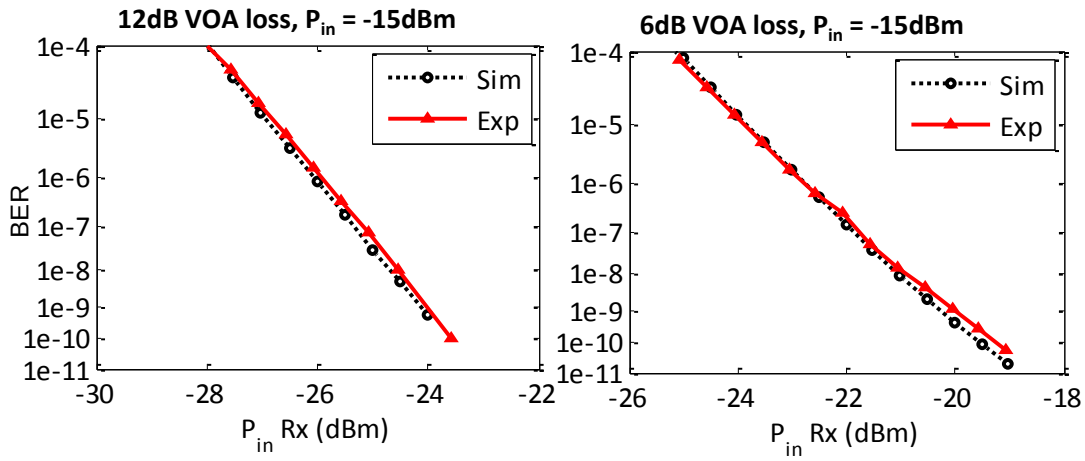

Figure 5.12. BER vs. received power for emulated R-EAM-SOA with internal loss and input powers indicated. Both Simulations and experimental measurements are shown.

5.4 R–EAM–SOA MODELLING

The work so far has concentrated on experimental devices and modelling their behaviour, now with a validated numerical model it is possible explore the entire parameter space with the ultimate goal of finding the optimum configuration for an R-EAM-SOA as the upstream transmitter in a long reach carrier distributed PON. In order to obtain accurate and reliable results it is desirable to maintain the same active region structure, and hence gain parameters, as the experimental device characterised and modelled in Chapter 4 [17], [18]. Therefore in order to vary the gain of SOA section only the length of the active region was changed. The accurate SOA model used takes into account longitudinal effects such as waveguide loss, bidirectional ASE propagation and non-uniform carrier distribution [70], thus allowing realistic and accurate modelling of SOAs with different lengths. Details for the parameter values used in the R-EAM-SOA modelling in this chapter are given in Table 5.3. The procedure used to derive these parameters can be found in [86].

The length of the SOA used in the emulated R-EAM-SOA was approximately 0.88mm. In the model this length can be reduced to give lower gain SOAs and increased to give SOAs with higher gain. In this and following Sections the loss in the device will not be broken down into different losses as has been done when describing the experiments and modelling carried out on the discrete R-EAM-SOA.

The R-EAM absorption loss and the interface loss between the SOA and REAM (equivalent to the VOA1 loss in the case of the discrete R-EAM-SOA) will be given as a total loss which will be referred to as the internal loss.

SET OF PARAMETERS USED IN MODEL CALCULATIONS

Parameter	R-EAM-SOA	Unit
SOA Length	0.6 – 1.5	mm
SOA Active Area	0.08	μm^2
SOA Waveguide Loss	25	cm^{-1}
Carrier injection eff.	95%	-
Radiative Recomb. coeff.	$1x10^{-10}$	cm^3s^{-1}
Auger Recomb. coeff.	$1x10^{-28}$	cm^6s^{-1}
Transparency Density	$5x10^{17}$	cm^{-3}
a_1, Gain Parameter	$2.7x10^{-17}$	cm^2
C_v, Gain Parameter	$3.44x10^{-6}$	Hz cm^3
Band gap wavelength	1640	nm
β_{eff}, ASE coupling coeff.	$3.2x10^{-3}$	-
ASE eff. wavelength	1550	nm
ASE gain param.	$3.1x10^{-17}$	cm^2
ASE transparency density	$1.2x10^{18}$	cm^{-3}
Input/Output port coupling loss	1.8	dB

Table 5.3. Set of parameters used in model calculations.

SOA length, mm	G_0, dB	$P_{sat,3dB}$, dBm
0.6	19	11
0.7	21	11
0.9	24	10
1.0	26	8
1.2	27	8
1.5	29	7

Table 5.4. SOA lengths, G_0 and $P_{sat,3dB}$ for modelled R-EAM-SOAs

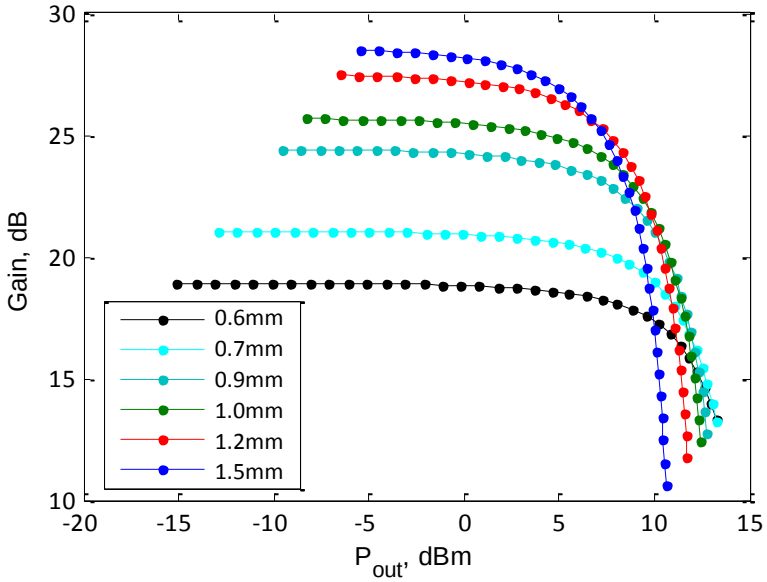

Figure 5.13. G_0 versus output power for modelled SOAs in single pass

The SOA sections were first modelled in single pass and without the R-EAM in order to find the unsaturated single pass gain (G_0) and saturated output power ($P_{sat,3dB}$) for the different SOAs lengths. The range of SOA lengths chosen and their corresponding G_0, and saturated output power $P_{sat,3dB}$ are listed in Table 5.4. It should be noted that an SOA drive current of 100mA was maintained for all modelled devices. Figure 5.13 shows the plot of G_0 versus output power for the different length SOAs. The SOA lengths chosen were from 0.6mm to 1.5mm, which gave a range of SOA's from low gain (G_0≈ 19dB) to very high gain (G_0 ≈ 29dB) with a range of $P_{sat,3dB}$ from 11dBm to 7dBm. It can be seen that the $P_{sat,3dB}$ reduces as G_0 increases due to the higher gain SOAs entering deep saturation at lower input powers. The loss range chosen was from 3dB to 33dB, with a step size of 3dB. A wide loss range is required to ensure suitable loss conditions are present for the various different gain SOAs.

A number of R-EAM-SOAs designs were then modelled across the range of SOA length and internal loss. A carrier wavelength of 1550nm was maintained for all modelling and the R-EAM was modulated at 10Gb/s with an NRZ data signal (2^7-1 PRBS) for all SOA lengths. Figure 5.14 (a) and (b) shows the output power as a function of input power curves for two low gain SOAs with lengths of 0.6mm and

0.7mm. The different losses are represented by different colours on the plot with loss increasing in the direction indicated.

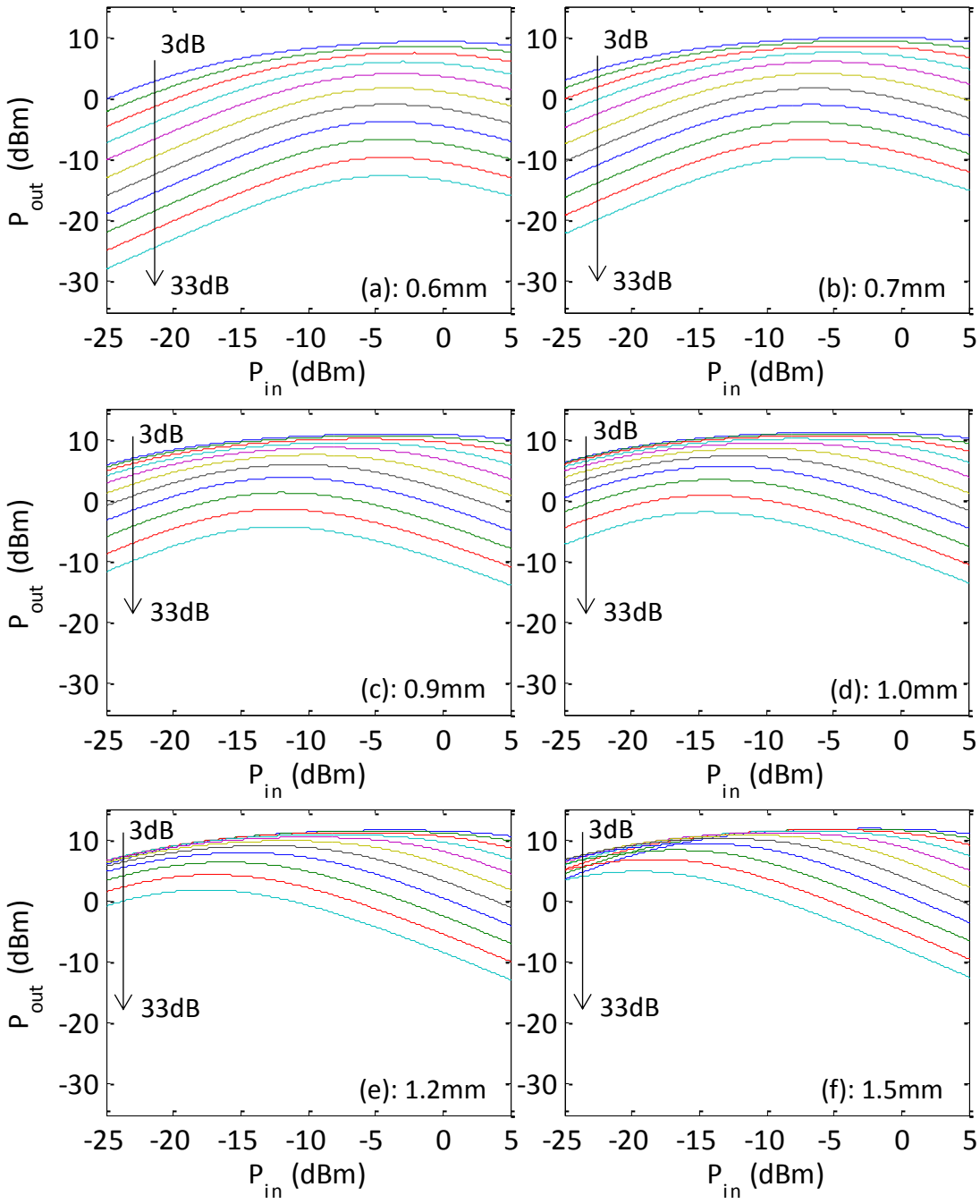

Figure 5.14. Output power versus input power for modelled R-EAM-SOAs with SOA lengths of (a): 0.6mm, (b): 0.7mm, (c): 0.9mm, (d): 1.0mm, (e): 1.2mm, (f): 1.5mm.

The striking features seen for the experimental device are again present for these modelled devices, namely the output power clamping and shift of the output power peak to lower input powers as the loss is increased. For the lowest gain (a), the peak output power is found at relatively high input power for all losses due to the low gain nature of the SOA. The position of the peak output power remains similar with only a small shift to slightly lower input powers as the loss is increased. For example at an internal loss of 3dB the output power peak is found at an input power of -1dBm while at an internal loss of 33dB the peak is found at an input power of -4dBm. The behaviour of this device is quite similar to that found with the integrated R-EAM-SOA discussed in chapter 4.

The next modelled device Figure 5.14 (b) has similar behaviour to Figure 5.14 (a); the output power peak does however move to slightly lower input powers as the internal loss is increased, from -2dBm at an internal loss of 3dB to -7dBm at an internal loss of 33dB. There is also a small increase in the peak power as would be expected from a higher gain device.

The shape of the output-input power curves for these devices is a result of the low gain SOAs used. The SOAs are not saturated or just starting to saturate for low input powers and therefore only reach the peak output power at high input powers, then after the output power peak there is a small reduction in output power due to the combination of gain saturation and internal loss.

In Figure 5.14 (c) and (d) the next two modelled devices are shown, the SOA lengths used here were 0.9mm and 1.0mm. Looking at device (c) a change in behaviour can be seen especially for higher internal losses. The higher gain of this SOA results in the peak output power moving to lower input powers than the previous low gain devices, when the internal loss is high, with the peak position moving from an input power of -3dBm for an internal loss of 3dB to an input power of -12dBm at an internal loss of 33dB. This device is operating in a similar regime to that of the R-EAM-SOA emulated by discrete components. This trend continues for the modelled device (d), with a further shift in the peak output power to lower input powers as the internal loss is increased. The output power peak moves from an input power of

-4dBm at an internal loss of 3dB to an input power of -14dBm at an internal loss of 33dB in this case.

Finally we look at the devices in Figure 5.14 (e) and (f), which have SOA lengths of 1.2mm and 1.5mm respectively. These very high gain devices continue the trend seen in (c) and (d) with the output power peak now moving to very low input powers for high internal losses. For the SOA with a length of 1.2mm, the position of the output power peak moves from an input power of -3dBm at an internal loss of 3dB to an input power of -18dBm when the internal loss is set to 33dB. For the highest gain SOA with a length of 1.5mm the position of the output power peak moves from an input power of -2dBm at an internal loss of 3dB to an input power of -19dBm at an internal loss of 33dB. This means the peak position has moved by 17dB as the internal loss is increased in the highest gain SOA compared to only a 3dB movement in the peak position with the same internal loss conditions for the lowest gain device (a), demonstrating the significant change in the operating regime of an R-EAM-SOA when the SOA gain is increased. These very high gain devices saturate at low input powers (~-20dBm) and thus reach the output power peak at much lower input powers than when using the low gain SOAs. They enter deep saturation for high input powers and as a result the gain is severely depleted; this in combination with high internal loss results in the considerable reduction in output power which can be seen for these devices when the input power is high. In a PON application scenario the position of the R-EAM-SOA output power peak is of great interest as it is vital to have the highest possible launch power from ONUs positioned in locations where the optical distribution network (ODN) loss is high in order to minimize the dynamic range of the upstream signal, this will be analysed in the next section.

5.5 DYNAMIC RANGE COMPRESSION

As outlined in Chapter 2 variations in splitter port loss, non-symmetric splitter distributions and fibre path length variations in a PON result in a differential loss (DL) between ONUs at different locations in the PON [25]. This is a major issue as it causes large burst-to-burst amplitude variations in the upstream signals from the different ONUs when they arrive at the upstream receiver. In a carrier distributed

PON that problem is even more severe and if the upstream transmitter in the customer ONU has linear gain the differential loss would double the number of dBs of dynamic range compared to what would be experienced in a more traditional PON configuration [17]. The output-input power characteristic shown in Chapter 4, where the output power is clamped in a correctly configured R-EAM-SOA, has the potential to reduce this dynamic range [17] by taking advantage of the peaked nature of the output power.

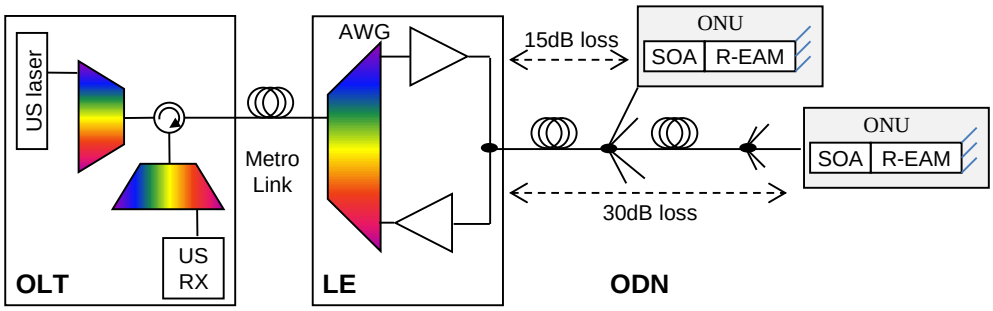

Figure 5.15. Access network configuration for Class C GPON upgrade scenario. LE: Local exchange, OLT: optical line termination, ODN: optical distribution network.

If the R-EAM-SOA is correctly designed then the ONUs with low input power (farthest from the LE) will have a higher output power than those with high input power (closest to the LE). This can help to overcome the differential loss between different the ONUs and thus reduce the dynamic range of the upstream signal.

Figure 5.15 shows the network configuration used for calculating the dynamic range, for this analysis we consider the specific scenario of the upgrade of a class C-GPON therefore 30dB maximum loss and 15dB minimum loss are used for the ODN (i.e. 15dB differential access loss). We further assume a carrier launch power of +15dBm from the local exchange (LE) into the ODN, which is representative of the typical achievable values if standard stimulated Brillouin scattering mitigation techniques are employed [13], [16]**.** Consequently the carrier power at the inputs to the R-EAM-SOAs on the network will vary between –15dBm (soft packet) and 0dBm (loud packet). Using the results for output power versus input power from Section 5.4 and applying them to the PON configuration in Figure 5.15, the dynamic range

between loud and soft packets arriving at the local exchange versus the internal loss of the R-EAM-SOA was calculated and is shown in Figure 5.16.

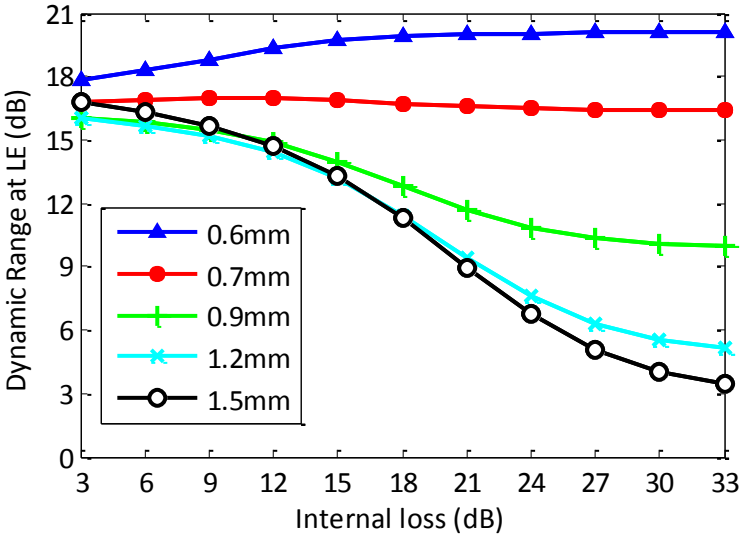

Figure 5.16. Dynamic range vs. internal loss measured at the local exchange for modelled R-EAM-SOAs.

A considerable change in dynamic range can be seen when moving from an R-EAM-SOA with a low gain SOA and low internal loss to one with a very high gain SOA and high internal loss. The low gain SOAs with lengths of 0.6mm and 0.7mm can achieve a minimum dynamic range of 18dB and 17dB respectively. Using this network configuration and a transmitter with linear gain the dynamic range at the receiver would be 30dB or more [17]. Therefore the low gain SOAs do offer some dynamic range reduction, however it is still relatively high. When the SOA gain is increased using lengths of 0.9mm, 1.2mm and 1.5mm significant dynamic range compression can be seen as the internal loss increases, with a dynamic range as low as 4dB possible for an R-EAM-SOA with very high gain and high internal loss.

The origin of this dynamic range reduction is the shift in the output power peak to lower input powers when the SOA gain and internal loss are high, as seen in Section 5.4. This shift in the peak means that the soft packet launch power increases in combination with a reduction in the loud packet launch power. The increased

launch power of the soft packet helps to partially compensate for the high ODN loss it experiences and thus reduce the dynamic range at the local exchange.

5.6 MODELLED EYE DIAGRAMS

As seen in chapter 4 the patterning distortion in these devices can be very different depending on the SOA gain and internal loss [17], [18]. Therefore the R-EAM-SOA model was also used to generate eye diagrams for a number of the modelled devices. The eye diagrams help to determine how changes in both SOA gain and internal loss in the R-EAM-SOA affect levels of patterning on the signal. For the purposes of this investigation three of the modelled R-EAM-SOAs were chosen, the low gain device with an SOA length of 0.6mm, the high gain device with an SOA of 0.9mm and the very high gain device with an SOA length of 1.5mm. Figure 5.17 shows the modelled eye diagrams for the low gain device, a range of losses from 6dB to 15dB was chosen and two input powers are shown, -15dBm (soft packet) and 0dBm (loud packet).

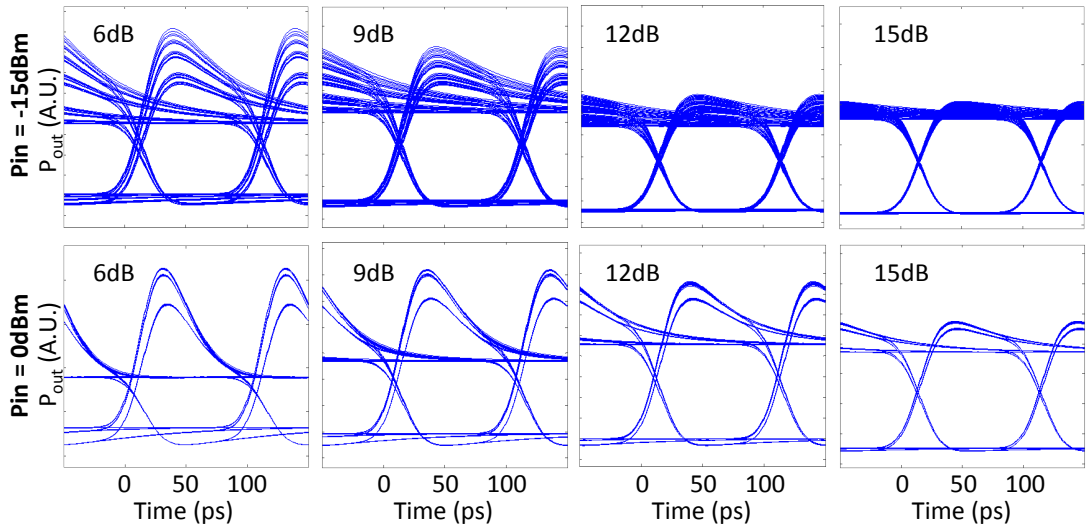

Figure 5.17. Eye diagrams for modelled R-EAM-SOA with a low gain SOA of length 0.6mm for indicated internal losses and input powers.

For the lowest loss of 6dB, both the loud and soft packets are affected by patterning as SOA saturation is dominated by the second pass modulated signal, the patterning is worse for the loud packet due to the SOA being in deeper

saturation. As the loss is increased to 9dB and then 12dB the pattering reduces in both cases as the CW input begins to contribute more to the saturation of the SOA. It is not until the loss is increased to 15dB however that the patterning has been significantly reduced for the loud packet.

Next eye diagrams were generated for the R-EAM-SOA with a high gain SOA with a length 0.9mm, these are shown in Figure 5.18. The internal losses are increased for this higher gain device with eyes shown for a range of 18dB to 27dB. The behaviour of this device is quite different to that of the device with lower gain.

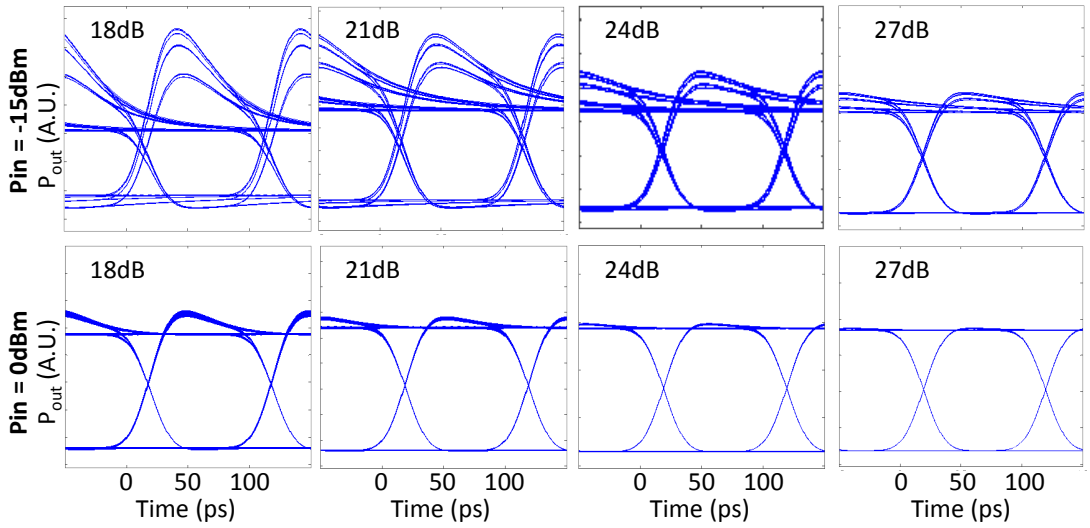

Figure 5.18. Eye diagrams for modelled R-EAM-SOA with a high gain SOA of length 0.9mm for indicated internal losses and input powers.

For the lowest internal loss of 18dB it is now the eye diagram with the lower input power of -15dBm which is most affected by patterning where the eye is visibly distorted. The eye diagram for the loud packet does suffer from some residual patterning but is much less affected than the soft packet as the CW input is clamping the gain of the SOA. A small increase in the internal loss eliminates any patterning for the loud packet but it is not until the highest internal loss shown of 27dB where patterning is significantly reduced for the soft packet. The behaviour of this device is therefore similar to that of the R-EAM-SOA emulated from discrete components. The higher gain of the SOA in this device results in it entering

saturation at much lower input powers and this causes the change in behaviour seen for high internal losses when compared to the lower gain device.

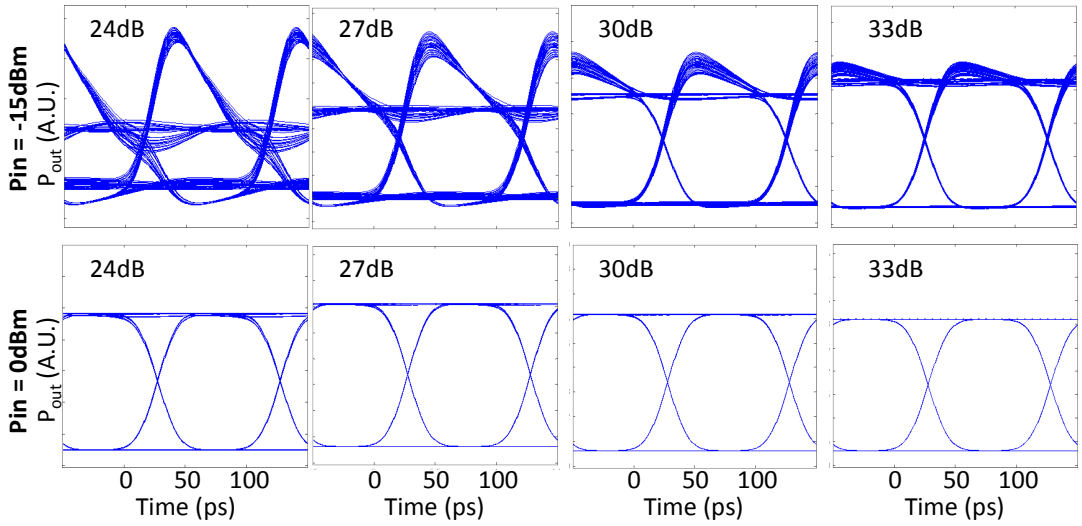

Figure 5.19. Eye diagrams for modelled R-EAM-SOA with a very high gain SOA of length 1.5mm for indicated internal losses and input powers.

Finally Figure 5.19 shows the modelled eye diagrams for an R-EAM-SOA with a very high gain SOA which had a length of 1.5mm. The range of internal loss used is 24dB to 33dB, in this case very high losses are required to compensate for the increase in SOA gain. For this device the eye diagram for the soft packet is severely distorted at 24dB loss due to SOA saturation being dominated by the modulated signal, however even at this relatively low loss there is almost no patterning on the eye for the loud packet, again because the SOA gain is clamped by the high CW input power. For the soft packet, it is not until a very high loss of 33dB is reached before the CW input begins to dominate SOA saturation sufficiently to considerably reduce the levels of patterning on the eye diagram.

This analysis demonstrates the importance of having sufficient internal loss to complement the increase in SOA gain. Studying both the eye diagrams and the dynamic range compression suggests that the best choice of device is one with a very high gain SOA and a high internal loss. However, the patterning mitigation and dynamic range reduction are not the only effects that need to be considered. The impact of the ODN loss and amplification of the upstream signal on the OSNR, and

in turn the BER also needs to be studied in order to find the optimum R-EAM-SOA configuration for use in a carrier-distributed long reach PON.

5.7 OPTIMISED R–EAM–SOA CONFIGURATION

To assess the BER performance of the modelled R-EAM-SOA's in a system scenario a VPI simulation setup was designed to simulate a carrier distributed PON, using the receiver which was validated in Section 5.3. The simulation schematic is shown in Figure 5.20.

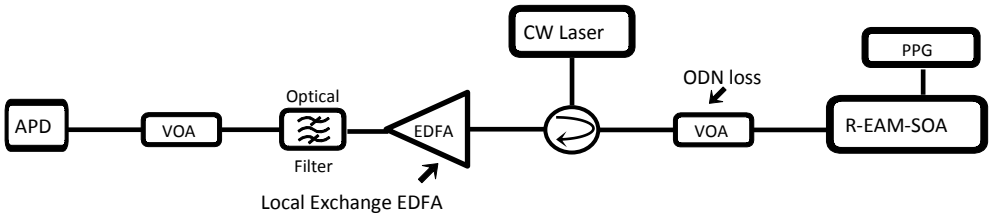

Figure 5.20. Simulation setup for carrier distributed PON.

The additions to this setup compared to the one used in Section 5.3 are a bidirectional VOA placed in front of the R-EAM-SOA which emulates the ODN loss and is varied to account for the differential ODN loss. It should be noted that this is the configuration in a real network scenario, in the VPI implementation the R-EAM-SOA module had an internal circulator and therefore separate VOAs were used at the input and output of the module rather than the double pass VOA shown here. An amplifier module is added which is setup to simulate an EDFA and represents the LE amplifier in a PON. The EDFA is set to have a gain of 23dB and a noise figure of 5.5dB, both of which are typical values for an EDFA which would be used in an optical access network. An optical channel filter (100GHz bandwidth) is also added after the EDFA. The metro section of the network is omitted since we aim to focus our study on the impairments which originate from patterning effects in the R-EAM-SOA and those from a reduced OSNR at the LE optical amplifier caused by the combination of low output power from the R-EAM-SOA and the ODN loss. There is no fibre used in the simulation as we want to omit the effects of dispersion in order to focus on the patterning and OSNR impairments.

The launch power into the ODN and differential ODN loss are kept the same as those used in the analysis of the dynamic range, which gives an input power to the R-EAM-SOAs of -15dBm for the soft packet and 0dBm for the loud packet. BER simulations were then performed using the modelled R-EAM-SOAs.

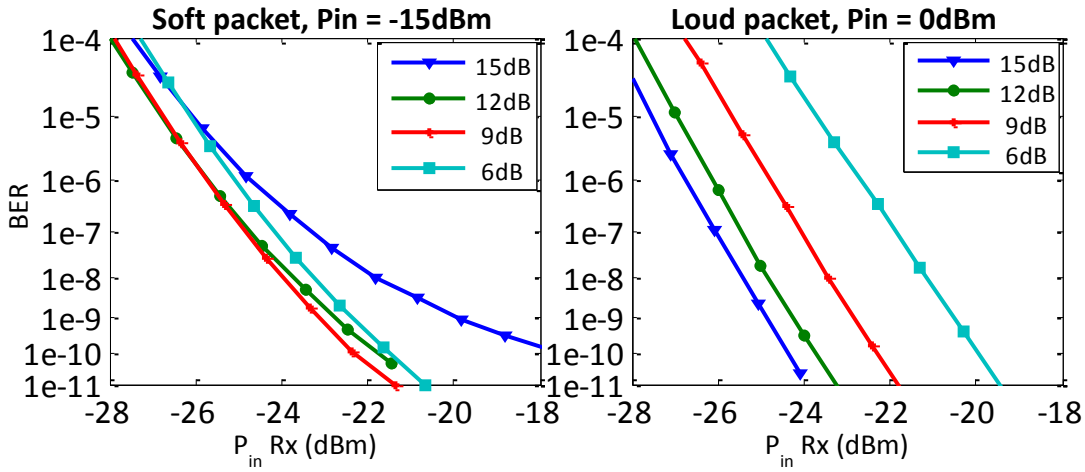

Figure 5.21. BER versus received power for a modelled R-EAM-SOA with a low gain SOA of length of 0.6mm in a carrier distributed PON. Internal loss values indicated in legend.

In order to show the significant change in performance when going from an R-EAM-SOA with a low gain SOA to one with a high gain SOA the two extreme cases which were modelled will first be analysed. Figure 5.21 shows the results of BER versus received power for an R-EAM-SOA with the low gain SOA which had a length of 0.6mm. The range of internal losses chosen was from 6dB to 15dB and plots for loud and soft packets are included. For the soft packet, the highest internal loss of 15dB had the worst performance. The low gain SOA and relatively high internal loss results in a low output power from the R-EAM-SOA and this in combination with the ODN loss degrades the OSNR of the signal resulting in a power penalty at the receiver.

As the internal loss is reduced the OSNR improves due to an increase in the output power, however reducing the internal loss to values lower than 9dB leads to a patterning penalty. In contrast the behaviour of the loud packet is quite different where high internal losses are giving the best performance, e.g. 15dB internal loss in this instance. This change in behaviour is due to the SOA being saturated by the

modulated signal which results in the onset of patterning and requires high internal loss in order to mitigate the effects. Patterning is the dominant contribution to receiver power penalties for the loud packet when a low gain SOA is used. This can also be seen in the eye diagrams in Figure 5.17.

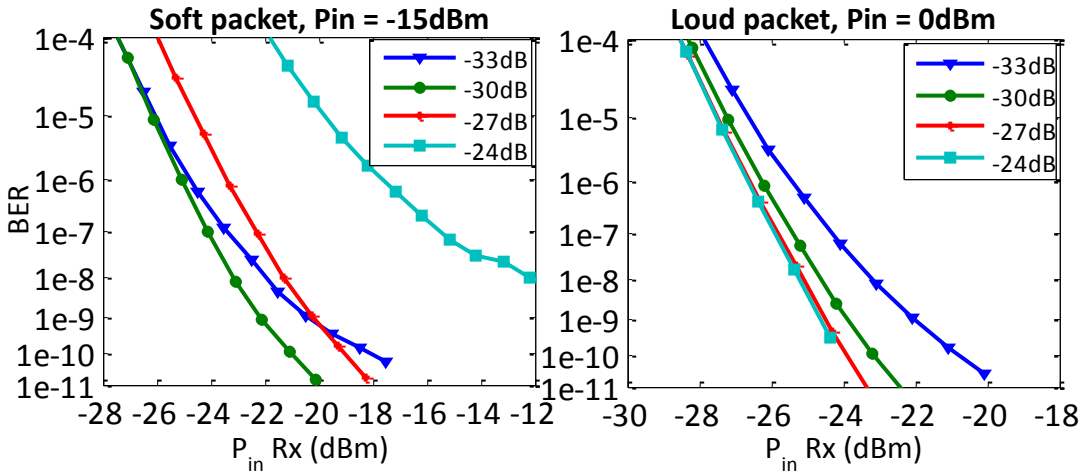

Figure 5.22. BER vs received power for a modelled R-EAM-SOA with a high gain SOA of length 1.5mm in a carrier distributed PON. Internal loss values indicated in legend.

The same analysis was carried out on a modelled R-EAM-SOA with a very high gain SOA which had a length of 1.5mm, the results are shown in Figure 5.22. In this case the range of losses chosen was from 24dB to 33dB. Again we start by looking at the plot for the soft packet, here the lowest loss condition of 24dB is severely affected by patterning, again because the modulated signal is contributing most to saturation in the SOA. Performance then improves with increasing loss until the highest loss condition of 33dB where again a degraded OSNR due to reduced output power from the R-EAM-SOA leads to a receiver power penalty.

Where the R-EAM-SOA with a low gain SOA was affected more by patterning in the loud packet case, the behaviour is quite different when the very high gain SOA is used. The loud packet is not affected by patterning due to the SOA now being pushed into deep saturation by the CW input, here the lowest loss setting of 24dB gives the best performance. A small power penalty is observed at 27dB loss due to a reduction in OSNR. This gets considerably worse when the highest loss condition of 33dB is reached where a large penalty can be seen. This is caused by a reduction in

OSNR which originates from a low output power from the R-EAM-SOA. This reduction in output power is due the change in slope of the output-input power curve at high internal losses. Again the trends seen in the eye diagrams in Figure 5.19 can be seen here with the BER measurements.

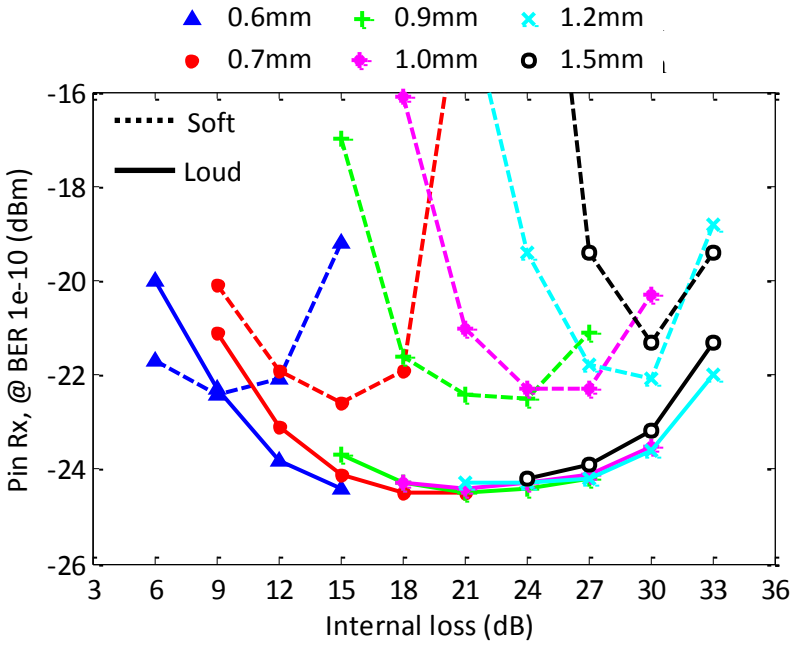

Figure 5.23. Received power required to achieve a BER of 10^{-10} (dBm) versus Loss (dB) for modelled R-EAM-SOAs with different SOA gain.

BER simulations were also performed on R-EAM-SOAs for the remaining SOA lengths of 0.7mm, 0.9mm, 1.0mm and 1.2mm. In order to easily compare the results for the different SOA lengths the received power required to achieve a BER of 10^{-10} was extracted from the plots of BER versus received power for each of the R-EAM-SOAs, including the lowest and highest gain devices already discussed. The received power required to achieve a BER of 10^{-10} is then plotted versus internal loss for both soft packets (dashed lines) and loud packets (solid lines) and is shown in Figure 5.23.

It can be seen in the plot that the soft packet performance is worse than that of the loud packet for almost all internal loss conditions and values of SOA gain. This is because the soft packet is more affected by OSNR degradation due to the high ODN

loss. Therefore it is the sensitivity of the soft packet which must be optimised in order to give best overall performance. Looking at the soft packet data, an optimum internal loss can be seen for each SOA and moving away from this optimum point results in a power penalty over the best case sensitivity. This penalty increases the further the internal loss moves from the optimum. The penalties seen at internal losses lower than the optimum are due to patterning in the SOA as the backward modulated signal is saturating the SOA due to insufficient internal loss. This was seen with the distorted eye diagrams for low internal losses in Section 5.6. Penalties at internal losses higher than the optimum are OSNR penalties caused by the high internal loss in the R-EAM-SOA. The high loss results in low output power which in turn leads to insufficient input power to the LE amplifier to maintain a high OSNR. The loud packets follow a similar trend, although the penalties are prominent only for the shorter and longer SOAs.

The minimum received power required for the soft packet is similar for all the SOAs, except for the very high gain device (1.5mm) whose poor performance is due to a combination of reduced OSNR and patterning. In order to find the optimum device a trade-off is required between optimum sensitivity, dynamic range and also how much tolerance the device has to deviations from the optimum internal loss and/or optimum SOA gain. As shown in Section 5.5 the dynamic range at the receiver is high for the low gain devices and the lowest gain device in particular also has a narrow range of optimum performance, where small changes in internal loss would result in a significant drop in performance. The very high gain and high internal loss devices also have a very narrow range of optimum performance. Despite the considerable dynamic range compression possible for R-EAM-SOA devices with very high gain and high internal loss they are not attractive from a PON application perspective due to their overall poor performance.

This analysis indicates that the optimum overall performance can be obtained from a device with an SOA length around 0.9mm and an internal loss in the 21dB to 24dB range. The optimized device shows low BER penalty over a wide range of optimum internal losses and also good dynamic range reduction with a dynamic range of approximately 12dB possible. Moreover the R-EAM-SOA with a 1.0mm SOA has similar performance to that with an SOA length of 0.9mm, this demonstrates the

added benefit of a tolerance to small changes in SOA gain easing the requirement to achieve a very precise SOA gain and internal loss, thus relaxing manufacturing tolerances and possibly reducing the effect of degradation due to device ageing.

It is important to note that this analysis was carried out with aim of optimizing the R-EAM-SOA for use in a network scenario with a burst mode receiver (BMRx) which can operate with a dynamic range of approximately 20dB [89] which is the target of upcoming PON standards [25]. Different trade-offs in the optimization could be made if, for instance, the R-EAM-SOA was to be used with a BMRx which could only handle a smaller dynamic range. In this case a higher gain device could be used such as the 1.2mm SOA which can achieve a lower dynamic range (≈7dB) at the expense of higher power penalty at the receiver.

5.8 CONCLUSIONS

The study of gain saturated R-EAM-SOAs conducted in Chapter 4 was broadened to include an investigation of how the BER obtained from the device is affected by changes to the internal loss of the device. Using these results for comparison a systems simulation tool was built in VPItransmissionMaker, which enabled BER estimates to be obtained for modelled versions of the experimental R-EAM-SOA. Then using both the validated numerical model and the system simulation tool an analysis was carried out on the affect changes to SOA gain and internal loss have on the performance of an R-EAM-SOA operating as the upstream transmitter in a carrier distributed long reach PON.

The significant change in behaviour of the device was demonstrated when moving from a low gain device with low internal loss to a high gain device with high internal loss. In particular the significant dynamic range compression which this novel solution can achieve, while still mitigating patterning effects, was shown. BER simulations of the modelled devices operating in a carrier distributed long reach PON have shown that increasing the device gain and internal loss to very high levels (G_0≈29dB) is also not beneficial and an optimum configuration was found consisting of a high gain SOA in combination with high internal loss, for example an SOA with a length of 0.9mm (G_0≈24dB) and internal loss in the 21dB to 24dB range. This

configuration gives the best balance between patterning reduction, high output power levels (hence maximizing available OSNR) and dynamic range compression for an R-EAM-SOA when operating in a network scenario where the BMRx can handle a dynamic range of approximately 20dB. It was also shown that the R-EAM-SOA can be designed to work with a BMRx which requires a smaller dynamic range by increasing the SOA gain and internal loss in order to reduce the dynamic range between upstream packets. However, this necessarily leads to an increased power penalty at the receiver.

6

FUTURE APPLICATIONS FOR REFLECTIVE MODULATORS

The analysis presented so far in this thesis has focused on long reach wavelength division multiplexed passive optical network (WDM-PONs), in particular the carrier distributed variant of WDM-PONs and the study of the R-EAM-SOA for use as the upstream transmitter. However the recent European research project, C3PO [19], has proposed extending the reflective concept outside WDM-PON and into metro transport networks and short-reach, high bit-rate inter-datacentre links. Exponentially increasing demands on the current metro network infrastructure are driving the development of next generation ultra-high bandwidth, energy efficient network architectures. Network operators are demanding a decrease in the cost per bit transported which will require a reduction in power consumption and more efficient utilisation of available space at metro nodes.

The C3PO project aims to address some of these challenges with a new type of metro node based on reflective technology and one of the key devices required to realise the proposed reflective metro node is a hybrid reflective electroabsorption (R-EAM) based photonic integrated circuit (PIC). In this Chapter the motivation for moving towards a reflective solution is first briefly discussed, followed by a description of the reflective metro node architecture. A detailed analysis is then carried out on the novel reflective modulator which is intended to operate as the transmitter in the metro node.

6.1 REFLECTIVE TECHNOLOGY AT METRO NODES

The rapid growth in bandwidth-intensive applications and exponentially increasing energy demands are driving the need for low cost, high capacity, energy efficient network architectures and photonic technologies to ensure the future scaling of access and metropolitan networks. DWDM approaches offer terabit-scale fibre capacities in current state-of-the-art infrastructures. However, growing traffic demands are requiring optical DWDM components with reduced power consumption, footprint, and therefore low cost-per-bit. In order to address these challenges, a potential solution involves the simplification and redesign of the network architecture to reduce the number of costly optical/electrical/optical (O/E/O) conversions.

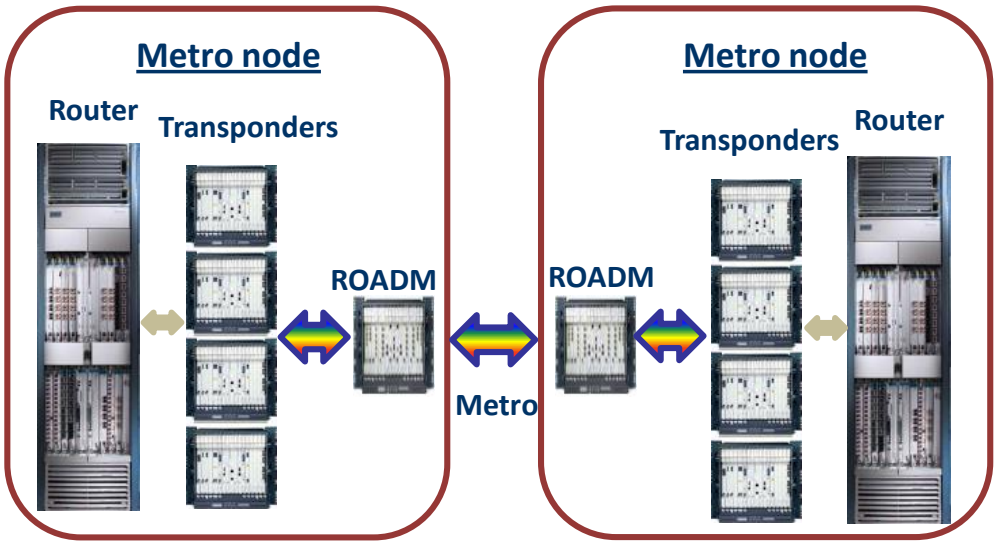

Figure 6.1. Current technology at metro nodes today.

Figure 6.1 shows the current configuration at metro nodes where uncoloured or "grey" short reach switch/routers interfaces are connected to DWDM transponders which perform the wavelength conversion and signal conditioning and coding required for long reach metro transmission. In addition, reconfigurable optical add and drop multiplexers (ROADMs) are used at the node to allow flexible routing and provisioning of wavelength channels in response to varying traffic demands. When a wavelength channel is received then the opposite process needs to be carried out.

The additional O/E/O conversion due to the separation of the electronic routing and long reach transport functions not only increases capital expenditure through the duplication of optic components but also results in additional power consumption and space requirements, thus increasing operating expenditure for network operators. One possible redesign approach is to realise DWDM router interfaces with tuneable lasers. However, current routers do not have the functionality required to dynamically set and control the wavelength of a tuneable interface. Replacing transponders with DWDM lasers placed directly on hot router linecards is also not desirable as it would mean cooled photonics being placed directly on the relatively hostile environment of the router. It would also require expensive tuneable lasers to be used in order to maintain wavelength flexibility. Therefore a more straightforward, power-efficient IP over DWDM (IPoDWDM) solution is proposed in [90] which is based on fully colourless, reflective transmitter modules located directly on the router linecards.

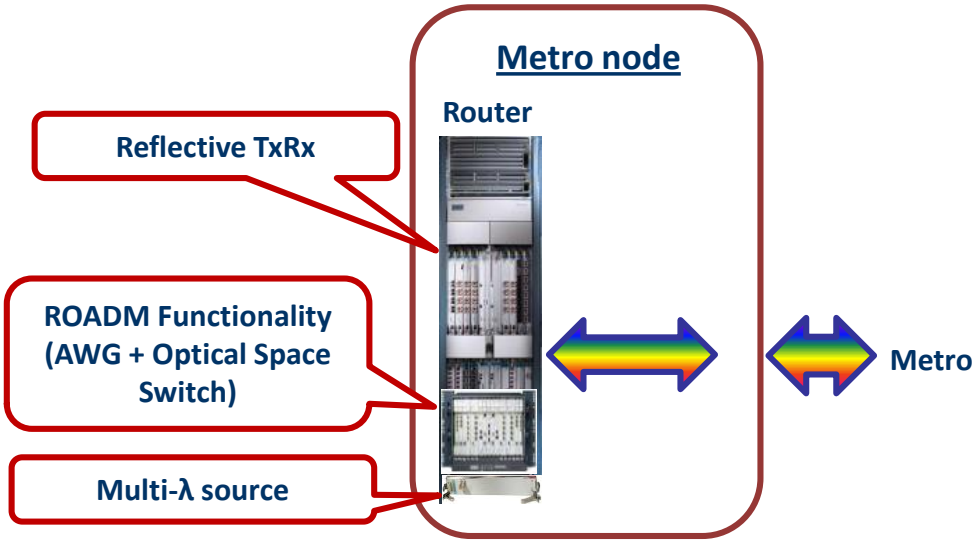

Figure 6.2. Simplified Metro node using reflective solution.

The simplified metro node design envisaged is shown in Figure 6.2. Figure 6.3 shows a schematic of the proposed architecture for a colourless reflective metro node which would enable dynamic IPoDWDM networks. This configuration demonstrated in [91], avoids the need for tuneable lasers and instead uses a multi-frequency laser

(MFL) to generate all the required optical carriers. The MFL then supplies the transmitters with all of the required optical carriers.

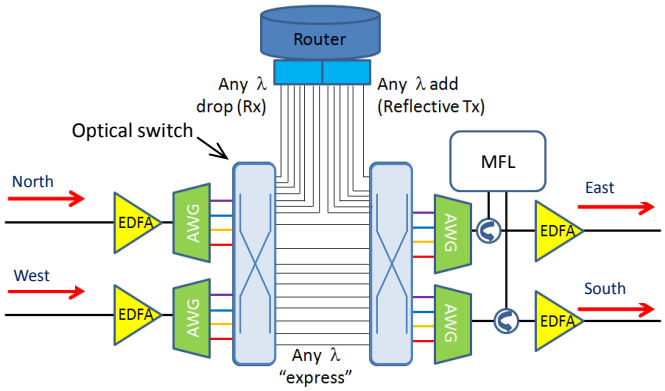

Figure 6.3.High-level schematic of the colourless reflective metro node architecture (AWG: Arrayed waveguide grating, MFL: multi-frequency laser.

The transmitters would be based on arrays of reflective electroabsorption modulators (R-EAMs) which would modulate the carrier and then reflect back the modulated signal. This is the same principle as described for carrier distributed PON in Chapter 2, except in this instance the carrier is supplied from a local source rather than being distributed across a network. An arrayed waveguide grating (AWG) and N-degree optical matrix switch [92], connected to all the reflective transmitters, is used to facilitate wavelength and optical path selection. The node would support 'express' wavelength channels, minimising the number of unnecessary O/E/O conversions by avoiding router traversals. The colourless, directionless, non-blocking optical space switch [92] provides full ROADM capabilities, including the wavelength 'add' and 'drop' functionalities. The complete metro node design creates a colourless, wavelength-agile interface with similar functionality as is currently available in state-of-the-art nodes.

The reflective modulators are a crucial part of the proposed reflective metro node and will be studied in detail in this chapter. The aim of realising the targeted low cost, reduced power consumption and compact footprint goals have the potential to be achieved if the reflective transmitters use hybrid array-integrated PICs which incorporate R-EAMs. The transmitters will be required to have a high throughput in order to handle the large volumes of data traffic at metro nodes and to achieve this

they must be capable of supporting multi-channel (multi-wavelength) operation. This can be achieved by integrating multiple reflective transmitters to give array transmitters capable of achieving 100Gb/s aggregate rates, suitable for support of 100GbEthernet services, for example. This can be done using either 10×10.Gb/s or 4×25Gb/s R-EAM arrays, but the latter is preferred for spectral efficiency reasons.

The reflective nodes are proposed for use in metro scale applications with distances of approximately 500km (using dispersion compensation) and high bit rate short reach uncompensated links for inter datacentre connectivity. For 25Gb/s line rates the traditional NRZ-OOK modulation used in PONs is not practical due to its relatively poor dispersion tolerance. Instead duobinary (DB) modulation is chosen due to its much increased dispersion tolerance compared to NRZ, its narrower spectrum which favours greater spectral efficiency through closer channel spacing while still using a simple low cost direct detection receiver.

6.2 REFLECTIVE DUOBINARY MODULATOR

DB modulation is traditionally implemented using a lithium niobate MZM. However the travelling wave electrode design and relatively large footprint of a MZM is unsuitable for the compact reflective configurations proposed. MZMs also require relatively high drive voltages which result in high energy consumption. Instead a novel hybrid PIC, containing reflective R-EAMs is proposed to act as the DB modulator. This device is optimised for low cost array integration and as EAMs are used the drive voltages required are also lower than those of MZMs. The reflective DB modulator was fabricated by CIP.

Figure 6.4 shows a block diagram of the reflective DB modulator, while Figure 6.5 shows a schematic of the device. The reflective DB PIC features an array of InGaAs/InAlAs multiple quantum well (MQW) R-EAMs [93], which incorporate mode expanders to allow for hybrid integration with silica waveguides. The MQW core provides high modulation efficiency with minimum saturation impairments at high input powers.

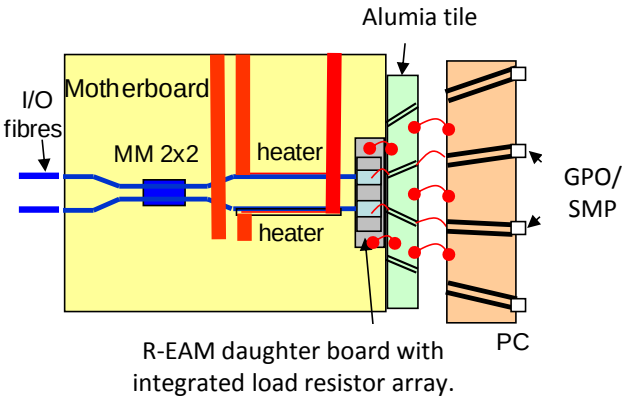

Figure 6.4. Block diagram of the reflective duobinary modulator

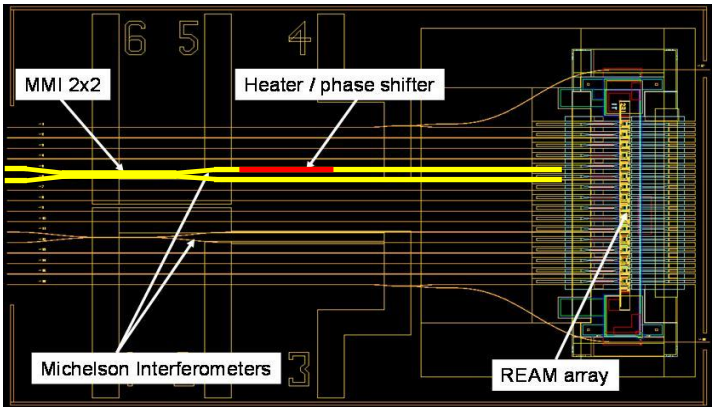

Figure 6.5. Schematic of the reflective DB modulator

The silica planar motherboard contains a hybrid Michelson interferometer circuit with a 2×2 multimode interference (MMI) coupler at its input. The phase difference between the two interferometer arms, required for generating DB, is adjusted using heater elements, which are deposited on the motherboard. The relatively small size of the R-EAM chip, approximate length of 0.2mm, permits further integration of multiple DB transmitters on a single compact board. Additionally, the reflective design benefits from shorter high-speed drive traces, as these are taken from the edge of the motherboard, hence minimising RF losses and crosstalk. The current prototype PIC is packaged with a polarisation-maintaining fibre, as such, the polarisation of the input CW carrier is fixed by aligning to the axis of this fibre. In

this reflective IPoDWDM approach, the carrier source is local to the reflective transmitter, so a means of polarisation control is feasible, unlike in remote modulation applications such as WDM-PON.

6.3 DUOBINARY MODULATION

Before explaining the operation of the reflective DB modulator the generation of DB is first discussed. Optical DB is classified as a partial response or correlative modulation format in which inter-symbol-interference (ISI) is intentionally and deterministically introduced to achieve the Nyquist rate for a given transmission bandwidth.

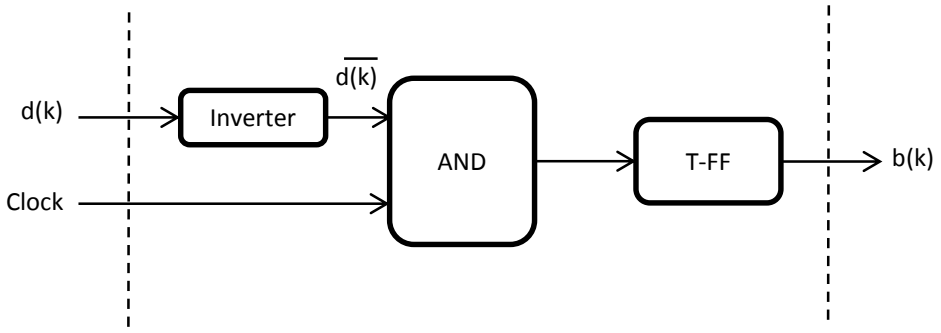

Figure 6.6. DB pre-coder implemented using an inverter and an AND gate followed by a T-Flip flop

The ISI introduced at the transmitter can then be unravelled at the receiver by differential decoding [94]. However, a single error at the receiver will propagate forever causing a catastrophic decoding error. Therefore optical DB is typically generated by first pre-coding an NRZ-OOK data signal. A pre-coder is implemented using an inverter and an XOR gate with a feedback path which has a one bit delay or an inverter and an AND gate followed by a T-Flip flop (shown in Figure 6.6).

The pre-coding rule for DB is

$$b(k) = \overline{d(k)} \oplus b(k-1) \qquad 6.1$$

where $d(k)$ is the transmitted binary sequence, $b(k)$ is the pre-coded binary sequence and $\oplus$ is the logic instruction "XOR" [94]. The pre-coded electrical signal

is then passed through either a two tap FIR filter and then low pass filtered to obtain an analog waveform or, more commonly, both of these steps are combined by using a Bessel-Thomson low pass filter (LPF) with a -3dB cut-off frequency at approximately one quarter of the bit rate of the original NRZ data signal. Both of these methods convert the two-level electrical NRZ signal to a three-level electrical signal using the following rule

$$c(k) = b(k) + b(k-1) \tag{6.2}$$

where $c(k)$ is the output from the LPF and $b(k)$ is the pre-coded binary sequence.

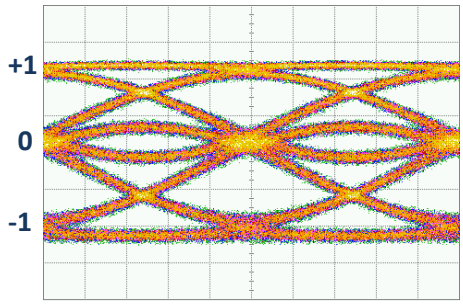

Figure 6.7. Three-level signal (DB drive waveform) generated by low pass filtering the NRZ signal.

The output symbols, $c(k)$ are "+1, 0, -1" as seen in Figure 6.7. An important property of the three-level signal at the output of the filter is that it is a correlated signal and therefore all possible values of the three values cannot occur, as will be explained later this is a key reason for DB's dispersion tolerance. The three-level electrical signal is then used to drive an optical modulator.

The most common modulator used for DB is either a dual-drive Mach-Zehnder modulator (MZM) driven in push-pull with a voltage swing of V_π in each arm or a single drive MZM with internal push-push biased at its null point and driven with a voltage swing of $2 \times V_\pi$ [95] as shown in Figure 6.8. The three-level electrical signal results in the MZM being driven around its minimum point. As can be seen in Figure 6.8 there is a π phase shift between the two transmission maxima, therefore 1-bits and -1-bits will be π out of phase with each other.

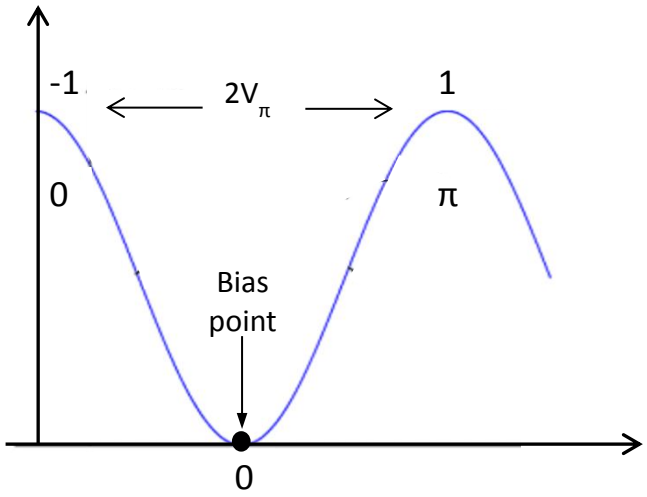

Figure 6.8. DB Transfer function for single drive MZM.

This results in a three-level signal in terms of electric field (0, $\pm|E|$) but only a two level signal in terms of optical power due to square-law detection at the receiver (0, $|E|^2$), thus meaning a simple direct-detection receiver can be used [22]. The phase change occurs when there are an odd number of 0-bits between two successive 1-bits meaning that for instance a "1 0 1" bit pattern in NRZ will be mapped to "+1 0 -1" in DB [22].

This phase change plays a key role in the much improved dispersion tolerance which can be achieved using DB. In a NRZ data sequence a "1 0 1" sequence gives "+E 0 + E" in the optical domain. As the pulses travel down the fibre they spread due to chromatic dispersion in the fibre and the E fields interfere constructively. This raises the power of the 0 level thus making the 0-bit harder to distinguish because of ISI and increasing the probability of an error [96]. However with DB the "1 0 1" sequence cannot occur while a "+1 0 -1" does occur. However as this is mapped to "+E 0 –E" in the optical domain there is now destructive interference between the E fields. This reduces the ISI for the 0-bit and therefore improves the dispersion tolerance for DB [22], [96]. The phase change that occurs for different 1-bits is also the reason for the carrier suppression seen with DB. On average the optical field of half the "1-bits" has a positive sign while the other half has a

negative sign. This results in a zero mean optical envelope and therefore there is no optical carrier present in a DB signal [22].

It is important to note that in laboratory experiments the step of pre-coding can be omitted if the data signal used is a pseudo-random binary sequence (PRBS). This is possible because a differentially pre-coded PRBS sequence is just a delayed version of the original sequence and as the BERT is capable of aligning the transmitted and received data streams, this delay is unimportant and the step of pre-coding the data is eliminated [97]. Therefore, for ease of implementation a pre-coder was not used in any of the experiments discussed in this chapter.

6.3.1 Generating Duobinary Using Reflective DB Modulator

Unlike a MZM, which can be driven between two transmission maxima with a π phase shift between them, a single R-EAM cannot be driven in a way which introduces the required phase shift required for DB signalling. The reflective DB modulator outlined in Section 6.2 is therefore designed to overcome this limitation by using two R-EAMs in a hybrid Michelson interferometer. Figure 6.9 shows the basic structure of the R-EAM DB modulator. If an overall π phase shift is introduced between the arms of the interferometer and the R-EAMs are driven in a push-pull configuration then it is possible to generate DB. The electrical three-level signal is generated in the same way as when using a MZM.

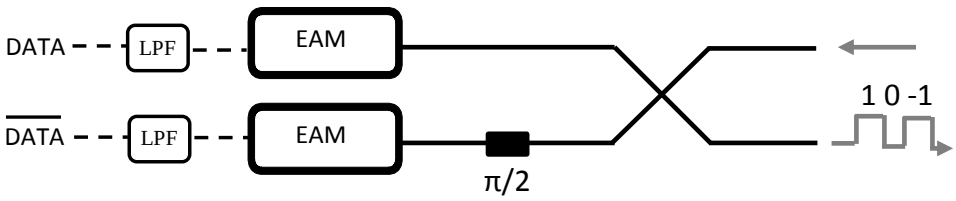

Figure 6.9. Block diagram of R-EAM DB modulator.

The CW light enters on one port of the MMI and is split equally between the two arms of the interferometer. One R-EAM is driven with the three-level data signal while the second R-EAM is driven in the same way except the logically inverted data signal is used.

Driving the R-EAMs in a push-pull configuration with a three-level drive signal means that, if one R-EAM is at the 1-level (transmitting) the second R-EAM is absorbing. Alternatively if one R-EAM is at the -1-level (transmitting) the other R-EAM is absorbing. The overall π phase shift introduced by the interferometer means that the phase of the signal produced by one R-EAM is shifted by π compared to a signal produced by the other R-EAM, at the output of the interferometer. This means the "1-bits" and "-1-bits" have a π phase shift between them as required for DB. The drive signal also produces a third state where both R-EAMs have equal bias and therefore reflect equal power. Because of the π phase shift between the two arms of the interferometer, this results in destructive interference between the two signals at the output of the interferometer and logical 0-bits are generated. The output DB signal is then output from the second arm of the MMI as shown in Figure 6.9. As with DB generated using a MZM the receiver does not distinguish between the "1-bits" and "-1-bits" due to square law detection and a simple direct detection receiver can be used.

This R-EAM based implementation has the advantage of using a lower drive voltage of $3V_{pp}$ for each R-EAM compared to the approximate 4.5V swing required to achieve V_π in each arm of a dual drive MZM or approximately 8V swing required to achieve $2 \times V_\pi$ for a single drive MZM.

6.4 10GB/S DUOBINARY EXPERIMENTAL SETUP

The experimental setup for generating DB at 10Gb/s using the reflective DB modulator is shown in Figure 6.10. A continuous wave (CW) optical carrier with a wavelength of 1550nm was generated by a tuneable laser and injected into the reflective modulator with an input power of +8dBm. The heater in one of the arms of the Michelson interferometer is biased in order to give a π/2 phase shift. This results in the optical signal in one arm experiencing a π phase shift relative to the other after the double pass through the modulator. Both R-EAMs are modulated at 10Gb/s with 3Vpp NRZ data (2^{31}–1 PRBS) superimposed on a DC bias which is set in the range of −1.2V to −2.2V depending on transmission distance. Both 10Gb/s NRZ data signals are filtered with 4th order Bessel-Thomson low pass filters (LPFs) which

generate the three-level electrical signals which are used to drive the R-EAMs between their high, intermediate, and low reflecting states.

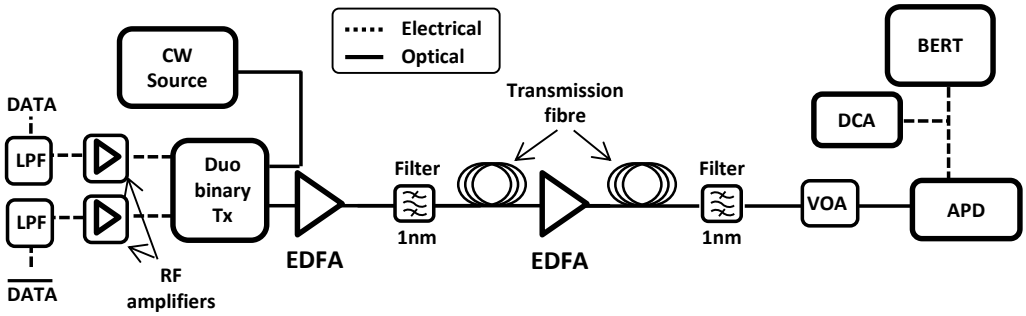

Figure 6.10. Experimental setup for 10Gb/s duobinary with reflective duobinary modulator.

One R-EAM is driven with the NRZ data while the other is driven with the logically inverted NRZ data. One set of LPFs had a -3dB bandwidth of 2.5GHz, while the second set had a -3dB bandwidth of 2.8GHz. In DB modulation, the LPF is normally set at one quarter of the bit rate, 2.5GHz for 10Gb/s, but for comparison filters with a higher frequency cut-off of 2.8GHz are also used in this study.

The resulting duobinary signal is amplified by an erbium doped fibre amplifier (EDFA) to overcome the relatively high overall dynamic insertion loss of the modulator, which was approximately 25dB. The output of the EDFA was then filtered using a 1nm bandpass filter to minimize the amplified spontaneous emission (ASE) falling on the receiver in back-to-back (B2B) (no transmission fibre) or being launched into the fibre in transmission. For transmission distances greater than 100km a second in-line EDFA was required to overcome loss in the additional fibre. For distances beyond 215km a third EDFA was required to overcome the additional loss. In all cases the optical signal to noise ratio (OSNR) was kept sufficiently high that receiver's thermal noise provided the dominant noise contribution in the system. A digital sampling oscilloscope with a 30GHz bandwidth optical input was used for measuring eye patterns and a 10Gb/s APD receiver (−26dBm sensitivity at a BER of 10^{-10}) coupled to a BERT was used for bit error rate (BER) measurements.

The modulator could also be configured to produce a conventional NRZ signal by simply switching off the RF drive signal to one of the R-EAMs and setting the bias to the maximum recommended valve of -3V in order to minimise the reflected power in that arm of the interferometer. The LPF was removed and the active R-EAM was modulated with a 10Gb/s NRZ signal. The relative π phase shift was maintained between the arms, the rest of the path to the receiver remains unchanged.

6.5 10GB/S DUOBINARY RESULTS

Figure 6.11 shows the optical spectrum for a 10Gb/s duobinary signal generated using the reflective DB modulator using the 2.5GHz LPFs. The resolution of the spectra were limited, to a bandwidth of 0.01nm, by the optical spectrum analyser used. For comparison the spectra for a 10Gb/s NRZ signal and the CW carrier only are also shown. The characteristic carrier suppression associated with DB can be seen in the spectrum when compared to the NRZ signal and CW carrier confirming the device is generating true DB. The reduced spectral width of the DB signal can also be seen when compared to the much broader NRZ signal. The reduction in spectral width is another important characteristic of DB signals.

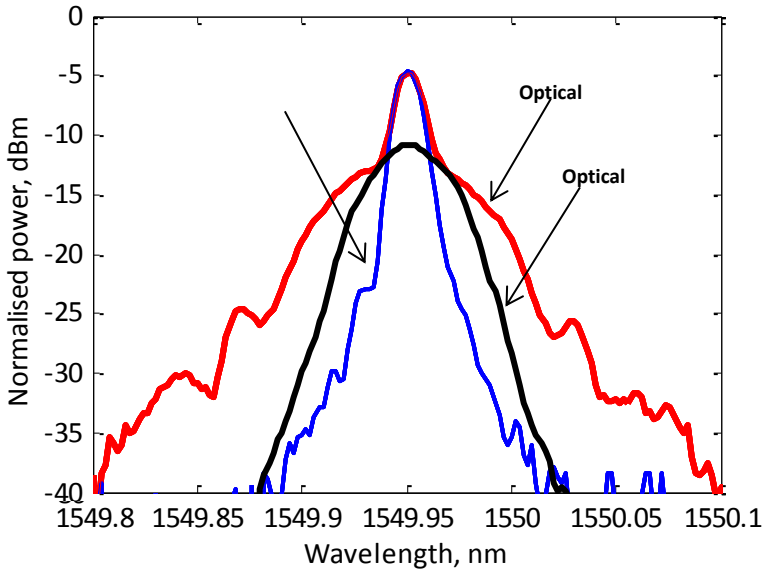

Figure 6.11. Optical spectrum of the CW carrier, 10Gb/s NRZ signal and 10Gb/s DB signal.

In the proposed DWDM applications the spectrally narrower DB signals have the potential to reduce cross talk between densely multiplexed channels and hence allow narrower channel spacings.

The BER of the DB signal was then measured in B2B and over a number of transmission distances up to 240km. Figure 6.12 shows the plot of BER versus received power for a number of the transmission distances studied. It can be seen that a BER of less than 10^{-10} was achieved for all distances up to 215km with no error floors present. When the transmission distance was further increased to 240km an error floor begins to appear at the relatively low BER of 10^{-9}. It can be seen that, as expected with DB, in the B2B case there is a receiver power penalty compared to a number of the transmission distances. This penalty is due to the ISI introduced by the low pass filtering. The input power of at the receiver to achieve a BER of 10^{-10} was -23.9dBm in B2B. The best performance can be seen at a distance of 150km where a BER of 10^{-10} is achieved at an input power to the receiver of -26dBm, giving a penalty of approximately 2dB in B2B over the best case performance. These BER results will be discussed in more detail later in this section.

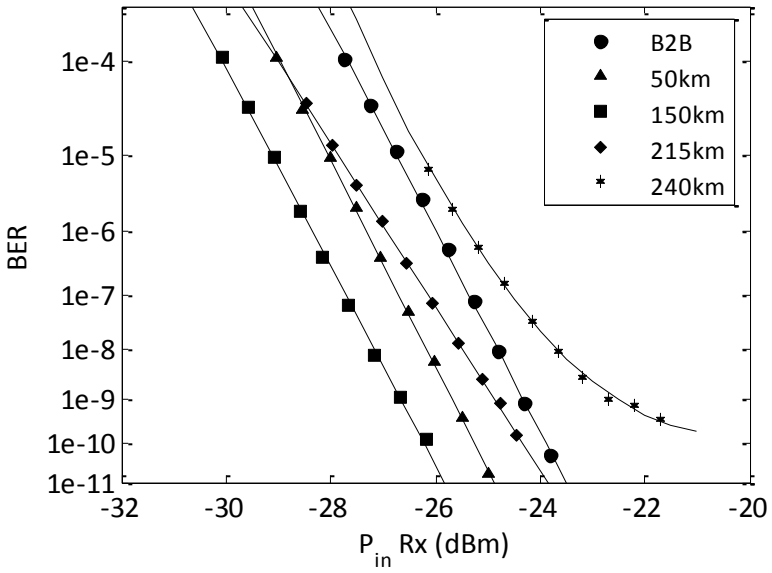

Figure 6.12. BER versus input power for Reflective duobinary modulator (2.5GHz LPFs)

Figure 6.13 shows the optical eye diagrams for B2B and transmission distances of 50km, 100km, 150km, 190km and 215km. It can clearly be seen that the eyes have a different shape to NRZ eyes, this is especially obvious for the 0-bit level where the destructive interference gives a very distinct 0-bit level. The good eye opening which is maintained up to a transmission distance of 215km again demonstrates the excellent dispersion tolerance offered by DB modulated signals. Although not shown here the eye diagram for 240km was also measured, as expected due to the error floor in the BER it showed considerable eye closure.

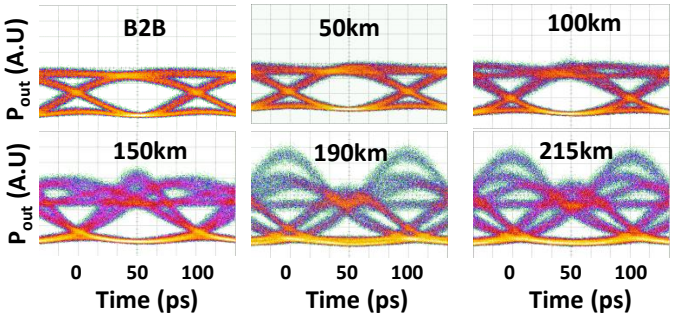

Figure 6.13. Received eye diagrams for reflective DB modulator (2.5GHz LPFs)

The same experimental procedure as describe above was then carried out for the LPFs with a -3dB bandwidth of 2.8GHz in order to investigate how a slight change in filtering would affect performance. Then, for comparison with the experimental measurements carried out using the reflective DB modulator, the setup was modified and the same set of measurements was carried out using a commercially available DB optimised Lithium Niobate MZM (Oclaro powerbit F10-D). Figure 6.14 shows the setup used to obtain BER measurements using the MZM. The reflective DB modulator was removed and replaced with the DB optimised MZM. The LPFs were removed as this device had built in filtering for 10Gb/s duobinary, it also required only one drive signal. The RF amplifier which gave a 3Vpp swing was also replaced with a driver amplifier which gave the $2 \times V_\pi$ swing of approximately 8V which was required to generate duobinary using the single drive MZM. The MZM was biased at its null point (minimum transmission) in order to swing between its two transmission maxima. The rest of the setup remained unchanged.

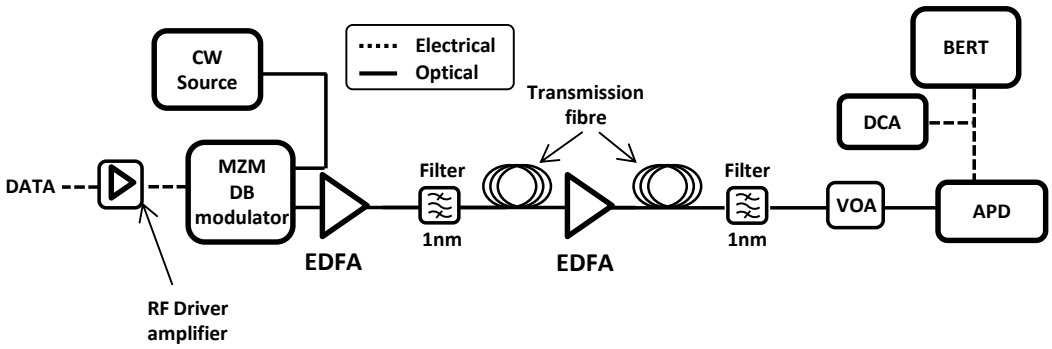

Figure 6.14. Experimental setup for 10Gb/s duobinary with commercially available duobinary optimised MZM.

The BER was then measured for DB signals generated by the MZM for transmission distances from B2B up to 215km. Figure 6.15 shows the combined results for the reflective DB modulator using the 2.5GHz (black line) and 2.8GHz (green line) LPFs, the NRZ results (blue line) and the DB results using the DB optimised MZM modulator (red line). For comparison purposes the results are plotted in the form of input power to the receiver required to achieve a BER of 10^{-10} versus transmission distance. First looking at the NRZ results, as expected the performance is excellent in B2B, achieving a receiver sensitivity of -27dBm at a BER of 10^{-10}.

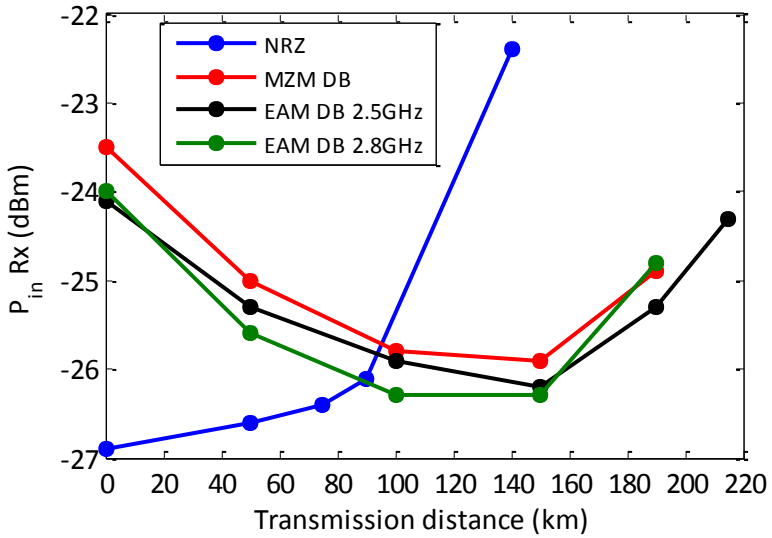

Figure 6.15. Input power to the receiver required to achieve a BER of 10^{-10} versus transmission distance for NRZ, DB modulation using the MZM and DB modulation using the reflective DB modulator for two different LPFs, 2.5GHz and 2.8GHz.

As the transmission distance increases a penalty begins to appear over the B2B case, at approximately 90km the penalty over B2B is approximately 1dB. After 90km however this penalty increases rapidly due to chromatic dispersion in the fibre. In contrast the results for DB using both the reflective DB modulator and MZM show a penalty over NRZ in B2B. The penalty over NRZ is approximately 2.8dB for both cases using the reflective DB modulator and approximately 3.3dB for the MZM. This penalty is consistent with what would be expected for DB [98]. The B2B penalty seen with DB over NRZ is due to a reduced extinction ratio. This is caused by ISI introduced by low pass filtering process which is used to generate the three-level drive signal. Concentrating on the DB results using the reflective modulator, a rapid improvement in sensitivity can be seen with increasing transmission distances for both filter configurations. The improvement continues up to approximately 150km, where the best case sensitivity is found in both cases at approximately -26.3dBm. At 150km DB has a penalty of approximately 0.7dB over NRZ in B2B. However it has already significantly surpassed the transmission distance possible with NRZ. As the transmission distance is further increased the received power required to achieve a BER of 10^{-10} begins to increase again. Using the 2.8GHz LPFs a transmission distance of 190km can be reached before error floors begin to appear at BERs higher than 10^{-10}. When configured with the 2.5GHz LPFs the reflective DB modulator can reach a transmission distance of 215km as previously seen in Figure 6.12.

The DB optimised MZM follows the same trend as the reflective DB modulator with an improvement in performance up to approximately 150km followed by an increase in required receiver input power to maintain a BER of 10^{-10}. The MZM can reach a transmission distance of 190km before error floors appear at BERs higher than 10^{-10}. These results demonstrate that the novel reflective DB modulator compares very favourably with a commercially available MZM optimised for DB and also the significant increase in transmission distances that can be achieved using DB modulation with only a small increase in transmitter complexity and no change in receiver configuration.

So far all results presented have been acquired at a wavelength of 1550nm, however the reflective DB modulator is required to operate across the C-band and therefore its colourless operation also needed to be demonstrated. To do this the

setup in Figure 6.10 was again used. In this case results were only obtained using the 2.5GHz LPFs and the transmission distance was fixed at 190km for all wavelengths. BER measurements were then carried out for wavelengths of 1530nm, 1540nm and 1560nm. Figure 6.16 shows the BER versus received power for the four representative C-band wavelengths which were tested. It can be seen in the plot that the device's performance is similar for the different wavelengths with just a small 1.3dB power penalty between the best and worst performing wavelengths, demonstrating the colourless performance of the reflective DB modulator. The penalty is attributed to the higher insertion loss of the R-EAMs at lower wavelength due to the proximity of the band edge which leads to a slight degradation in the available OSNR.

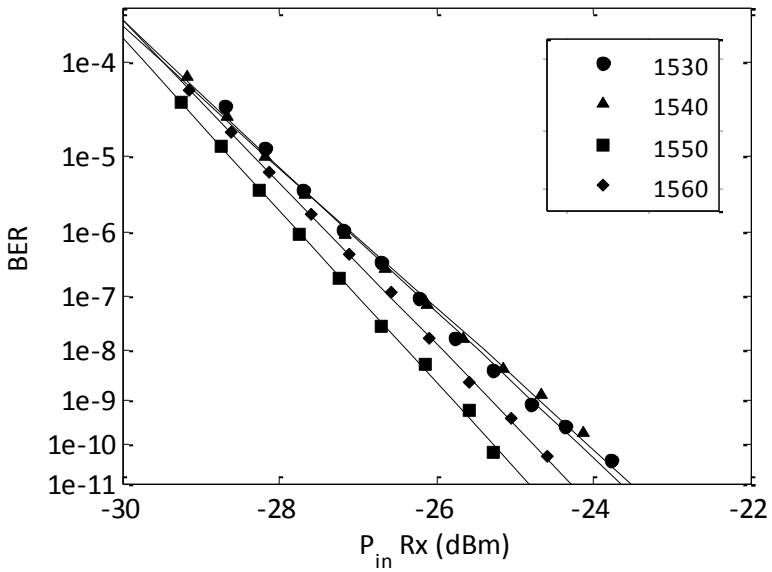

Figure 6.16. BER versus received power for a transmission distance of 190km for the reflective DB modulator operating at 10Gb/s (2.5GHz LPFs).

The device in its current configuration would allow a multichannel arrayed device to achieve 100Gb/s aggregate rates (10x10Gb/s) using an array of R-EAMs. However a more compact and wavelength efficient way of achieving a 100Gb/s aggregate rate is to use a 4x25Gb/s configuration and therefore the next step in this study was to generate 25Gb/s DB using the same reflective DB modulator.

6.6 25GB/S DUOBINARY EXPERIMENTAL SETUP

Figure 6.17 shows the experimental setup used to generate 25.3Gb/s DB modulated signals. The setup is considerably more complex than the one used to generate DB at a bit rate of 10Gb/s.

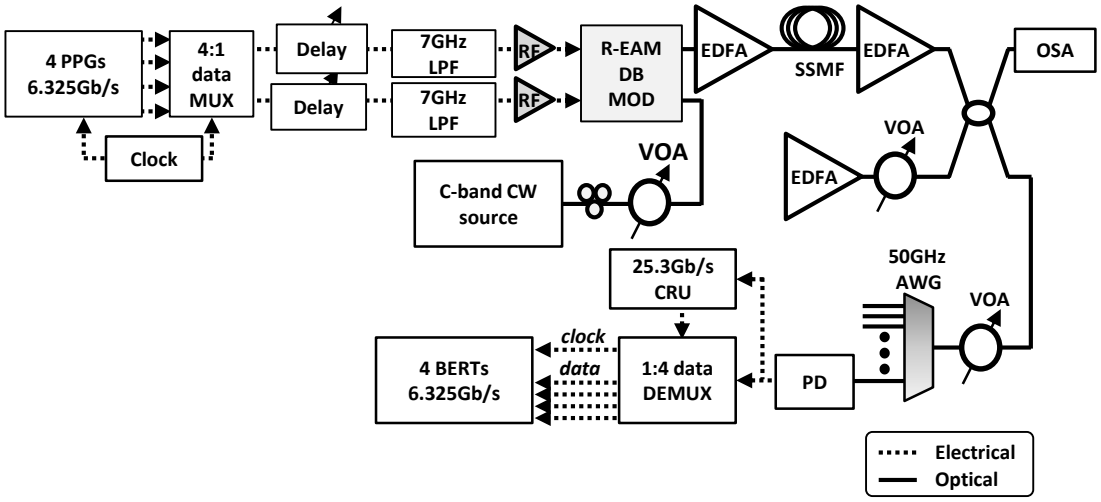

Figure 6.17. Experimental setup for 25Gb/s duobinary with reflective DB modulator.

Again the CW optical input power to the reflective DB modulator is maintained constant at +8dBm. Similar to the previous setup the heater element in one arm of the interferometer is biased to give an overall π phase shift to the signal in one arm of the device compared to the other after a double pass through the interferometer. The 25.3Gb/s drive signal is generated by electronically multiplexing four 6.325Gb/s NRZ signals (2^7-1 PRBS) from four pulse pattern generators (PPGs). The multiplexer (MUX) outputs both a 25.3Gb/s data signal and a logically inverted 25.3Gb/s data signal. Both data signals were then filtered using 4th-order Bessel-Thomson low-pass filters (LPFs) with a -3dB bandwidth of 7GHz. These filters had a frequency cut-off higher than one quarter of the bit rate but at the time of the experiment they were the closest available. The three-level waveforms generated by low-pass filtering drive the R-EAMs between their high, intermediate, and low reflecting states. One R-EAM was driven with the filtered 25.3Gb/s data signal while the second R-EAM was driven with the filtered and

inverted 25.3Gb/s from the MUX. Both driving signals had a swing of 3Vpp which was achieved using an RF amplifier for each of the data signals.

Again due to the relatively high insertion loss of the current prototype device, the DB modulated signal was amplified by an EDFA before being detected in the B2B case or being launched into standard single mode fibre (SSMF) of various lengths from 10km to 41km in the transmission case. A second EDFA is used after the transmission fibre as a pre-amplifier, the output of this EDFA is connected to one arm of a 2x2 coupler. A third EDFA is connected to the second input arm of the 2x2 coupler. This third EDFA acts as an ASE source to degrade the OSNR at the receiver. The OSNR is controlled in the setup by a variable optical attenuator (VOA) placed after this EDFA. One output arm of the 2x2 coupler is connected to an optical spectrum analyser (OSA) for OSNR measurements (with 0.1nm reference bandwidth), while the other arm is connected to an arrayed waveguide grating (AWG) with an average -3dB optical bandwidth of 22.1GHz per channel, and 50GHz channel spacing across the C-band. The chosen output channel from the AWG was then coupled to a PIN receiver with a bandwidth of 50GHz; while a considerably wider bandwidth than required this was the only receiver available with sufficient bandwidth to detect 25Gb/s signals. The wavelengths used in the experiment are chosen to match the fixed AWG channels which had a range from 1535.04nm to 1560.61nm.

The input power to the receiver was kept constant and sufficiently high above the thermal noise floor such that the OSNR degradation is the dominant impairment in the system. The receivers 25.3Gb/s electrical output signal is de-multiplexed using a 1:4 de-multiplexer (DEMUX) to return the signal to the four 6.325Gb/s tributary channels. These tributary channels were then connected to four BERTs to monitor the BER of the entire system simultaneously. The PPGs and MUX are synchronized using a common clock, while the DEMUX and BERTs use a 25.3Gb/s clock recovery unit (CRU) to extract the clock for BER analysis.

6.7 25GB/S DUOBINARY RESULTS

Using the above setup, the device first generated 25.3Gb/s DB modulated signals with the CW carrier set to a wavelength of 1542.54nm. Figure 6.18 shows the optical spectra of the CW carrier and of the 25.3Gb/s duobinary signal after the modulator, again the resolution of the spectra were bandwidth limited to 0.01nm. As in the 10Gb/s results the characteristic DB spectrum can be seen with no carrier component. The necessary hardware was not available at the time of the experiment to generate 25Gb/s NRZ for comparison.

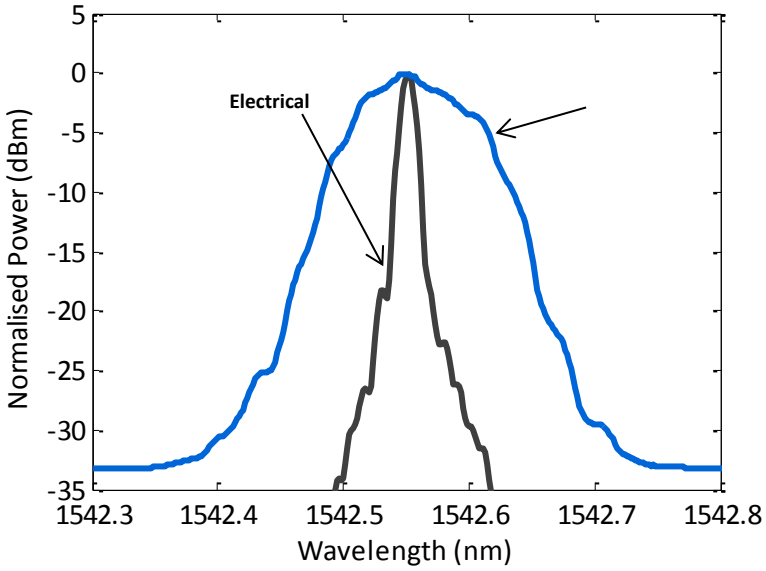

Figure 6.18. Optical spectra of the CW carrier and of the 25Gb/s duobinary modulated signal at a wavelength of 1542.54nm.

The laser was then tuned to generate a CW carrier at a wavelength of 1549.65nm, which was injected in the DB modulator. The OSNR was degraded by increasing the ASE power from the third EDFA, and the BER was measured with respect to the OSNR for a representative set of transmission lengths using several spans of SSMF. The measured OSNR penalty for the B2B case at a BER of 10^{-3} is within 2dB of the expected theoretical value for DB modulation assuming the use of a MZM and with similar receiver bandwidth [22]. This penalty was attributed to the non-optimised frequency response of the R-EAMs and RF package over this wide frequency range.

Figure 6.19 shows the BER versus OSNR for the reflective DB modulator operating at 25.3Gb/s for B2B up to a transmission distance of 41km. As expected, we observe the reduction in required OSNR associated with DB transmission as the distance increases from B2B which had a required OSNR of approximately 26.5dB up to 16km where the lowest required OSNR to achieve a BER of 10^{-12} is found at approximately 25dB.

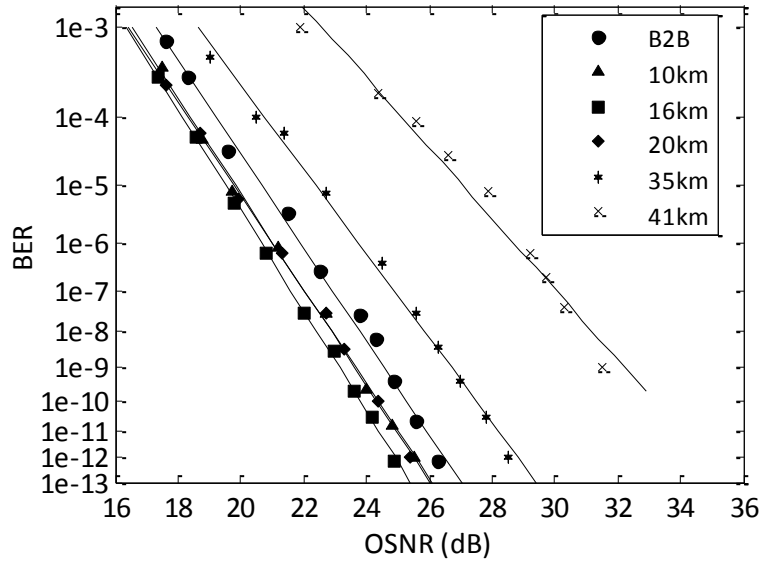

Figure 6.19. BER versus OSNR for the reflective DB modulator operating at 25.3Gb/s (wavelength = 1549.65nm).

This measurement was however limited by the maximum achievable OSNR in the experimental setup. This performance degradation arises from chromatic dispersion, which causes intersymbol interference and subsequent eye closure. This value is consistent with the results obtained at 10Gb/s using the same device in Section 6.4, since the dispersion-limited reach at 25.3Gb/s is reduced by approximately the square of the bit rate as expected.

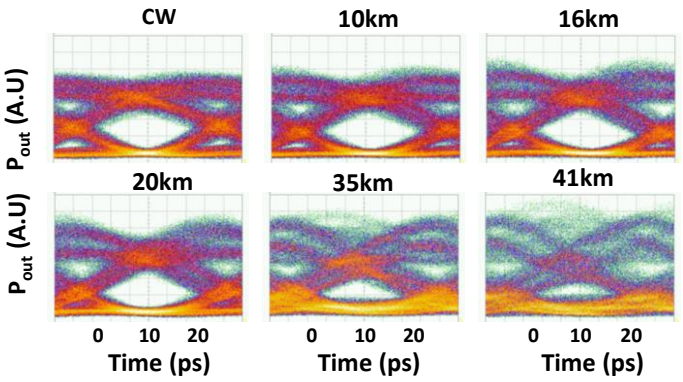

Figure 6.20. Optical eye diagrams for the reflective DB modulator operating at 25.3Gb/s and at a wavelength of 1549.65nm.

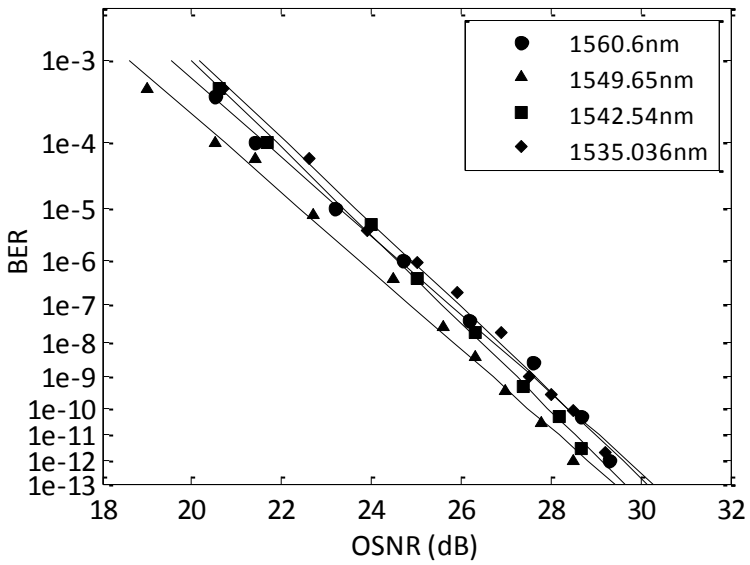

Figure 6.21. BER versus OSNR for a transmission distance of 35km for the reflective DB modulator operating at 25.3Gb/s. Four representative wavelength channels shown spanning the C-Band.

The optical eye diagrams of the 25.3Gb/s DB modulated signals for six of the transmission lengths of SSMF at a wavelength of 1549.65nm are shown in Figure 6.20. A substantial eye opening is achieved at all distances, with the exception of 41km, where the received eye is significantly degraded.

Similar to 10Gb/s operation, the reflective DB modulator's colourless nature is confirmed by measuring the BER, at 25.3Gb/s, as a function of the measured OSNR at the greatest error-free distance (35km). This was done for several C-band wavelengths on the 50GHz ITU grid. The BER curves for four representative wavelength channels between 1535.04nm and 1560.61nm are shown in Figure 6.21. Figure 6.22 shows the OSNR values required to obtain a BER of 10^{-10} for eight uniformly-spaced channels across the C-band. Again comparable performance is achieved within the device's anticipated operating wavelength range, with a small 1.2dB difference in required OSNR for this greater than 25nm span. Measurements at wavelengths shorter than 1535nm were not feasible in the case of the 25Gb/s DB study due to the vicinity of the band edge of the R-EAM. This resulted in an increased insertion loss which meant there was insufficient OSNR to carry out measurements below 1535nm.

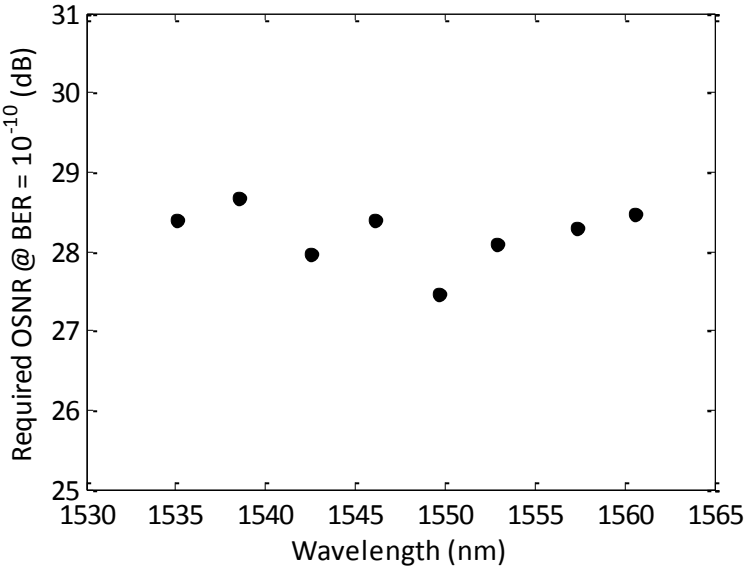

Figure 6.22. OSNR required to achieve a BER of 10^{-10} versus wavelength for a number of wavelengths across the C-band

6.8 CONCLUSION

In this chapter results have been presented for a novel reflective EAM based DB modulator. In Section 6.5 results have shown that the device is capable of

transmission up to 215km of standard single mode fibre at 10Gb/s with comparable performance to a commercially available MZM based DB modulator. In Section 6.7 it has been demonstrated that the device is also capable of operation at 25Gb/s, where it can achieve error free transmission over 35km of SSMF. It is important to note that for short-reach intra-data centre links low cost interfaces are used and hence forward error correction is not supported. Therefore, the error free transmission achieved here with no error floors present up to 35km is crucial for these applications. In longer reach metro transport applications FEC is generally supported and for these applications a BER of approximately 10^{-3} is generally required. Similar hybrid reflective devices have been shown to support differential quadrature phase shift keying (DQPSK) modulation formats [99]. However, to the best of our knowledge, this is the first demonstration of error-free 25Gb/s DB transmission using such a reflective component.

In the proposed metro node application, the ability of the device to work across a wide range of wavelengths within the C-band is essential. The colourless operation of the device was therefore also verified at both 10Gb/s and 25Gb/s. In both instances the device showed only a small wavelength dependant penalty of less than 1.5dB. The results attained with this prototype device pave the way for multichannel arrayed devices to achieve 100Gb/s aggregate rates, using either 10x10Gb/s or 4x25Gb/s R-EAM arrays. This work is the first step to realising energy-efficient, multi-lane, arrayed PICs for wavelength-dynamic, low cost-per-bit 100GbE services and applications in next-generation metro transport networks.

The results have shown that this reflective EAM approach offers a viable alternative to the traditional MZM based approach for generating DB. The R-EAM based modulator also has a number of advantages in comparison to a MZM DB modulator. The R-EAMs in the device require a lower drive voltage of approximately $3V_{pp}$ compared to an approximate 4.5V swing required for the arms of a dual-drive MZM or up to 8V swing for a single drive MZM. This reduced voltage requirement has the potential to offer significant savings in power consumption in a metro node incorporating large arrays of transmitters. Another advantage of this approach is the small size of the R-EAM chip (approximately 0.2mm in length). This small form factor will allow the integration of multiple DB transmitters on a single

compact motherboard. The Michelson interferometer also allows a more compact device to be designed compared to the travelling wave electrode design in a MZM.

There are also, however, a number of challenges which need to be overcome with the reflective DB modulator design. One of the most significant problems with the current device is a high insertion loss. There is potential to optimise the current design but ultimately, due to characteristics such as the insertion loss of the R-EAMs, there is a limit to how much device losses can be reduced. In the experimental setup the insertion loss was overcome by using an EDFA at the output of the device, however this is not a feasible in a real network scenario.

To overcome the insertion loss the reflective DB modulator can be redesigned to incorporate integrated R-EAM-SOAs instead of R-EAMs. R-EAM-SOAs have already been studied in detail in the previous Chapters of this thesis for applications in PONs. The same features of integrated R-EAM-SOAs which make them an attractive solution for PON applications can also be exploited in the reflective DB modulator. The net gain offered by the R-EAM-SOA has the potential to significantly reduce the insertion loss of the reflective DB modulator without significantly increasing the form factor of the device or preventing low-cost array integration. The addition of R-EAM-SOAs to the reflective DB modulator will result in a very attractive device for applications in future reflective architectures in metro transport networks and short reach high bit-rate inter-datacentre links.

7

CONCLUSIONS AND FUTURE WORK

In this thesis the behaviour of a novel reflective modulator was analysed in detail both experimentally and using a numerical model. The modulator, which consists of a semiconductor optical amplifier (SOA) and a reflective electroabsorption modulator (R-EAM) integrated together in a single compact device (R-EAM-SOA), has potential to act as the upstream transmitter in long reach carrier distributed PONs. Using an integrated R-EAM-SOA it is possible to achieve the required net gain and low chirp modulation needed for 10Gb/s operation over distances in the order of 100km. Devices of this type have also demonstrated unexpected behaviour when operated in a regime of gain saturation where the output power of the device is clamped to a maximum and the output signal is not affected by patterning as would be expected when using a gain saturated SOA.

As it was not possible to vary any of the important parameters in the integrated device an emulated R-EAM-SOA was built from discrete components where the device could be analysed in more detail by allowing the adjustment of the internal loss, in a way which was not possible with a fully integrated device. The experimental investigation using the emulated R-EAM-SOA indicated that the value of the internal loss was a crucial factor in order to achieve the output power clamping effect and also the highly desirable patterning suppression effect.

Using the numerical model it was possible to confirm for the first time that these effects are related to the amount of internal loss present after the SOA section and on the single pass gain of the SOA section. The experimental and modelling results compared here for different SOA single pass gain and internal loss show that, against intuition, a high gain and high internal loss allow these devices to operate in

a region of output power clamping and also with low patterning distortion. Under these conditions the low frequency noise suppression on the input carrier is also accessible at low input carrier power and in a region of operation with little patterning distortion.

A significant change in behaviour of the R-EAM-SOA was then demonstrated when moving from a low gain device with low internal loss to a high gain device with high internal loss. In particular a significant dynamic range compression, which this novel solution can achieve, while still mitigating patterning effects, was shown. BER simulations of the modelled devices operating in a carrier distributed long reach PON have shown that increasing the device gain and internal loss to very high levels is also not beneficial and an optimum configuration was found consisting of a high gain SOA in combination with high internal loss, for example an SOA with a length of 0.9mm (G_0≈24dB) and internal loss in the 21dB to 24dB range.

This configuration gives the best balance between patterning reduction, good output power levels (hence maximizing available OSNR) and dynamic range compression for an R-EAM-SOA when operating in a network scenario where the burst mode receiver (BMRx) can handle a dynamic range of approximately 20dB. We have also shown that the R-EAM-SOA can be designed to work with a BMRx which requires a smaller dynamic range by increasing the SOA gain and internal loss in order to reduce the dynamic range between upstream packets. However, this necessarily leads to an increased power penalty at the receiver.

The focus then moved from reflective configurations for PON applications to a proposed reflective architecture for metro nodes. Results were presented for a novel reflective EAM based duobinary (DB) modulator and it was shown that the device is capable of transmission up to 215km of standard single mode fibre at 10Gb/s with comparable performance to a commercially available MZM based DB modulator. It was also demonstrated that the device is capable of operation at 25Gb/s, where it can achieve error free transmission over 35km of single mode fibre. In the proposed metro node application the ability of the device to work across a wide range of wavelengths within the C-band is essential. The colourless operation of the device was therefore also verified at both 10Gb/s and 25Gb/s. In

both instances the device showed only a small wavelength dependant penalty of less than 1.5dB. The results attained with this prototype device pave the way for multichannel arrayed devices to achieve 100Gb/s aggregate rates, using either 10x10Gb/s or 4x25Gb/s R-EAM arrays. Similar hybrid reflective devices have been shown to support differential quadrature phase shift keying (DQPSK) modulation formats. However, to the best of our knowledge, this is the first demonstration of error-free 25Gb/s DB transmission using such a reflective component. This work is the first step in realising energy-efficient, multi-lane, arrayed PICs for wavelength-dynamic, low cost-per-bit 100GbE services and applications in next-generation metro transport networks.

The results have shown that this reflective EAM approach offers a viable alternative to the traditional MZM based approach for generating DB. The R-EAM based modulator also has a number of advantages in comparison to a MZM DB modulator. The R-EAMs in the device require a lower drive voltage of approximately $3V_{pp}$ compared to an approximate 4.5V swing required for the arms of a dual-drive MZM or up to 8V swing for a single drive MZM. This reduced voltage requirement has the potential to offer significant savings in power consumption in a metro node incorporating large arrays of transmitters. Another advantage of this approach is the small size of the R-EAM chip (approximately 0.2mm in length). This small form factor will allow the integration of multiple DB transmitters on a single compact motherboard. The Michelson interferometer also allows a more compact device to be designed compared to the travelling wave electrode design in a MZM.

7.1 FUTURE WORK

Optimised integrated R-EAM-SOA:

The analysis carried out in Chapters 4 and 5 used discrete components to experimentally demonstrate the importance of the internal loss in an R-EAM-SOA. Modelling was then used to determine the optimum balance of SOA gain and internal loss for an R-EAM-SOA which is operating as the upstream transmitter. The next step in the analysis would be to have an integrated device fabricated with the optimum configuration outlined in Chapter 5. A possible approach would be to have an integrated R-EAM-SOA fabricated with a variable internal loss in order to

experimentally demonstrate the change in behaviour which was seen in Chapter 4 but with a fully integrated device rather than discrete components.

One way to realise this would be the fabrication of a split contact SOA section, where altering the drive current to the second contact would alter the transmission properties of that SOA section. Another possibility is the addition of a second (unmodulated) EAM section between the SOA and R-EAM. Here changes in the bias voltage would allow changes to absorption properties of the EAM and thus provide a controllable loss. Ultimately, it would be desirable to experimentally demonstrate an optimised integrated R-EAM-SOA operating in a carrier distributed long reach PON test-bed.

Reflective DB modulator incorporating SOAs:

The results presented in Chapter 6 have shown that the reflective DB modulator can offer a viable alternative to more traditional MZM based DB modulators. There are, however, a number of challenges which need to be overcome with the reflective DB modulator design. One of the most significant problems with the current device is a high insertion loss. There is potential to optimise the current design but ultimately there is a limit to how much device losses can be reduced. To overcome the insertion loss the reflective DB modulator can be redesigned to incorporate integrated R-EAM-SOAs instead of R-EAMs.

An important analysis which could be carried on a reflective DB modulator which incorporated R-EAM-SOAs is the effect of frequency chirp. A traditional DB transmitter uses a chirp free MZM, however both EAMs and SOAs can add chirp to a signal. The impact of this chirp on the performance of the DB transmitter would be an important consideration.

Another important study would be the investigation of 25Gb/s DB channels transmission on a 25GHz grid and the associated filtering penalties. This would be very attractive as it would give an improved spectral efficiency of 1b/s/Hz compared to e.g. 0.2 bits/s/Hz which would be the widely deployed last generation standard for 10Gb/s on 50GHz grids. This would still not offer the spectral efficiency possible with coherent systems but it would offer a simpler and cheaper solution.

APPENDIX

ANALYTICAL MODEL

The analytical model used in Chapter 4 of this thesis is based on the double pass SOA model presented in [77]. It should be noted that the intensity I used in in [77] is replaced with power P.

Starting from the Maxwell and Schrödinger equations, a semiclassical model for the propagation of optical signals in a semiconductor optical amplifier (SOA) can be developed.

A double pass amplifier is necessarily bi-directional and for simplicity the known form for the plane-wave field equations in a bidirectional homogeneously broadened SOA are adopted [77]. These equations are written as

$$\frac{dA^{+}(z)}{dz} = -\eta\left[A^{+}(z) - \frac{(1+iy)D_0(z)A^{+}(z)}{1+iy+[|A^{+}(z)|^2+|A^{-}(z)|^2+2|A^{+}(z)A^{-}(z)|\cos(2kz)]}\right] \quad \text{A.1}$$

$$\frac{dA^{-}(z)}{dz} = -\eta\left[A^{-}(z) - \frac{(1+iy)D_0(z)A^{-}(z)}{1+iy+[|A^{+}(z)|^2+|A^{-}(z)|^2+2|A^{+}(z)A^{-}(z)|\cos(2kz)]}\right] \quad \text{A.2}$$

where $A^{+}(z)$ and $A^{-}(z)$ are the normalised complex amplitudes of the right and left travelling waves at a point z inside the amplifer, η corresponds to a loss rate per unit of propagation distance, $D_0(z)$ is the normalised unsaturated population difference and the normalised optical frequency is $y = (\omega - \omega_0)/\gamma$ with ω_0 the centre frequency of the transition and γ the decay rate for the off-diagonal elements of the density matrix [77]. The field amplitudes have been normalised in such a way that in a one dimensional amplifier $[A^{+}(z) \neq 0, A^{-}(z) = 0]$ tuned to a line centre $(y = 0)$ the field gain is reduced to half of its unsaturated value $[nD_0(z)]$ when the magnitude of the field is equal to unity $[|A^{+}(Z) = 1|]$. The cosine term in

the saturation denominator results from interference between the right and left travelling wave held components. The relative phases of the right and left waves have been assumed to be unimportant, but they could be included by shifting the arguments of the cosine functions. These equations account for the effects of line centre detuning and longitudinal hole burning. The earlier equations govern the spatial evolution of the electromagnetic fields. It is also useful to convert them to an equivalent set of equations for the right and left travelling powers. By defining normalised powers $sP^+(z) = |A^+(z)|^2$ and $sP^-(z) = |A^-(z)|^2$ the following can be obtained from Equation 3.14 and Equation A.2

$$\frac{dP^+(z)}{dz} = -2\eta\left[P^+(z) - \frac{D_0(z)P^+(z)}{1 + y^2 + s\{P^+(z) + P^-(z) + 2[P^+(z)P^-(z)]^{1/2}\cos(2kz)}\right] \quad \text{A.3}$$

$$\frac{dP^-(z)}{dz} = +2\eta\left[P^-(z) - \frac{D_0(z)P^-(z)}{1 + y^2 + s\{P^+(z) + P^-(z) + 2[P^+(z)P^-(z)]^{1/2}\cos(2kz)}\right] \quad \text{A.4}$$

In this notation $P^+$and P^- are the actual powers and s is a saturation parameter. Equations A.3 and A.4 are similar to Equations 3.14 and A.2 but the information on the phase of the wave has been lost in Equations A.3 and A.4. $A^+A^- = constant \equiv sa$ and $|A^+|^2|A^-|^2 = s^2|a|^2$, where the constant a has been introduced. The complex electric field amplitudes can now be written in terms of only one variable

$$A^+(z) = s^{1/2}a^{1/2}\exp[(1 + iy)\alpha(z) + iynz + i\Phi], \quad \text{A.5}$$

$$A^-(z) = s^{1/2}a^{1/2}\exp[-(1 + iy)\alpha(z) - iynz - i\Phi], \quad \text{A.6}$$

where Φ is an integration constant and $\alpha(z)$ is a real gain coefficient for the field governed by

$$\frac{d\alpha(z)}{dz} = -\eta\left[1 - \frac{D_0(z)}{1 + y^2 + s|a|\{\exp[2\alpha(z)] + \exp[-2\alpha(z)] + 2\cos(2kz)\}}\right], \quad \text{A.7}$$

The original coupled complex differential equations have therefore been reduced to a single real equation. Since the absolute phase of the reflected wave would usually

not be of interest, it is convenient to work initially with the power equations rather than with Equation A.7. From Equations A.5 and A.6 the powers can be written as

$$sP^{+}(z) = |A^{+}(z)|^2 = s|a| \exp[2\alpha(z)], \quad \text{A.8}$$

$$sP^{-}(z) = |A^{-}(z)|^2 = s|a| \exp[-2\alpha(z)]. \quad \text{A.9}$$

The function $\alpha(z)$ need in Equations A.5 and A.6 can therefore be obtained from the powers. By neglecting the $\cos(2kz)$ term as it is only significant in short distance in a high gain amplifier and the distributed loss term Equation A.3 can be written as

$$\frac{dP^{+}(z)}{dz} = \eta \frac{2D_0(z)P^{+}(z)}{1 + y^2 + s[P^{-}(z) + |a|^2/P^{+}(z)]}, \quad \text{A.10}$$

It is assumed that the unsaturated population difference D_0 is independent of position z and therefore Equation A.10 can now be integrated. The corresponding phase can be obtained from by application of Equations A.5 and A.6. The new gain and saturation parameters are

$$g = \eta \frac{2D_0}{1 + y^2}, \quad \text{A.11}$$

$$s' = \frac{s}{1 + y^2}, \quad \text{A.12}$$

Equation A.10 can be written as

$$\frac{dP^{+}(z)}{dz} = \eta \frac{gP^{+}(z)}{1 + s[P^{+}(z) + |a|^2/P^{+}(z)]}. \quad \text{A.13}$$

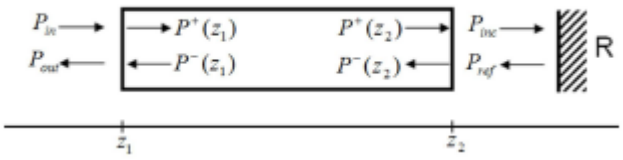

Figure A.1. Definitions of powers in a double pass amplifier.

Integrating Equation A.13 results in the following

$$s'[P^+(z_2) - P^+(z_1)] + \ln\left[\frac{P^+(z_2)}{P^+(z_1)}\right] - \frac{s'|a|^2}{P^+(z_2)} + \frac{s'|a|^2}{P^+(z_1)} = gL \qquad \text{A.14}$$

The position and direction notation is indicated in Figure A.1 where R is the reflection coefficient. As the product of the right and left powers is independent of position in the amplifier and the two ends of the SOA this implies

$$P^+(z_1)P^-(z_1) = P + (z_2)P^-(z_2) = |a|^2. \qquad \text{A.15}$$

The power on the right side are related to R according to

$$P^-(z_2) = RP^+(z_2). \qquad \text{A.16}$$

The constant $|a|^2$ is given by

$$|a|^2 = \mathrm{R}[P^+(z_2)]^2 \qquad \text{A.17}$$

Equation A.14 can then be written as

$$s'[(1-R)P^+(z_2) - P^+(z_1) - P^+(z_1)] + \ln\left[\frac{P^+(z_2)}{P^+(z_1)}\right] = gL \qquad \text{A.18}$$

The power $P^+(z_2)$ can be eliminated from Equation A.18 by means of the boundary conditions. Combining Equations A.15 and A.16 we get the following

$$P^{+}(z_2) = \left[\frac{P^{+}(z_1)P^{-}(z_1)}{R}\right]^{1/2} . \quad \text{A.19}$$

Inserting Equation A.19 into A.18

$$s'\left\{(1-R)\left[\frac{P^{+}(z_1)P^{1}(z_1)}{R}\right]^{1/2} + P^{-}(z_1) - P^{+(z_1)}\right\} + \left\{\frac{P^{-}(z_1)}{RP^{+}(z_1)}\right\} = 2gL \quad \text{A.20}$$

In a double pass amplifier having one mirror the powers $P^{+}(z_1)$ and $P^{-}(z_1)$ can be replaced with the input powerP_{in} and the output power P_{out}. Equation A.20 can then be written as

$$2\left(\frac{1}{P_s}\right)\left[(1-R)\left(\frac{P_{in}P_{out}}{R}\right)^{\frac{1}{2}} + P_{out} - P_{in}\right] + \ln\left[\frac{P_{out}}{RP_{in}}\right] = 2gL \quad \text{A.21}$$

Where $1/P_s$ represents the saturation parameter s' and gL is the single pass gain-length product. Equation A.21 is the key part of the analytical model used in Chapter 4. Although the above equation must be solved numerically it is much simpler than the numerical model which was also used in Chapter 4.

NUMERICAL MODEL

The key part of the R-EAM-SOA model used to analyse the experimental results in this thesis is the SOA model, which is described in detail in [70]. The SOA model accounts for the saturation caused by the bidirectional ASE propagation in the device, which is an important phenomenon to understand and to obtain accurate behaviour regarding the carrier saturation and recovery in SOAs [71]. In the model, the ASE is described by its total power, neglecting its spectral dependence. By using effective parameters for the total spontaneous emission (SE) coupled into the waveguide, β_{eff}, and for the modal gain of the ASE, g_{ase}, we account for the spectral dependence of the ASE. In this way, the information on the ASE spectrum is lost, but on the other hand the equations for the propagation of the ASE are reduced to only two, one for each direction of propagation. The computational complexity, which is a key factor in time domain simulations, is thus reduced considerably compared with models where the whole ASE spectrum is propagated.

The internal parameters, such as modal gain, waveguide losses, injection efficiency and SE spectral density coupled into the waveguide, are extracted from the CW characterization of the devices small signal gain and gain saturation. The propagation equations for the signal can be written as

$$\frac{dP^{\pm}{}_{sig}}{dz} = \pm(g(n) - \alpha)P^{\pm}{}_{sig} \tag{A.22}$$

where P^{+}_{sig} is the power of the forward propagating signal and P^{-}_{sig} is the power of the backward propagating signal and g is the modal gain.

The propagation equations for the ASE power will be

$$\frac{dP^{\pm}_{ase}}{dz} = \pm(g_{ase}(n) - \alpha)P^{\pm}_{ase} \pm \beta_{eff}(n)R_{sp}(n)\frac{hc}{\lambda_{ase}}\sigma \tag{A.23}$$

where P^{+}_{ase} and P^{-}_{ase} are the power of the forward and backward propagating ASE beams, σ is the cross-section of the active region, g_{ase} and β_{eff} are the effective values, λ_{ase} is a parameter introduced to have the correct unites of measure.

The rate equation can be written in the same way as the propagation equation

$$\frac{dn}{dt} = \eta_I \frac{I}{qV} - R(n) - g(\lambda_{sig}, n)\frac{P_{sig}}{\sigma}\frac{\lambda_{sig}}{hc} - g_{ase}(n)\frac{P^{+}_{ase} + P^{-}_{ase}}{\sigma}\frac{\lambda_{ase}}{hc} \tag{A.24}$$

where I is the bias current, η_I is the injection efficiency of the carriers into the active region, V is the volume of the active region, $R(n)$ is the total recombination rate, q is the electron charge, g is the modal gain, P_{sig} is the sum of the signal powers at a specific position along the length of the SOA given by the propagation equation and λ_{sig} is the signal wavelength. In contrast to [70], the total recombination is modelled using a two-term expression [86]

$$R(n) = r_1 n^2 + r_2 n^3 \tag{A.25}$$

where the first term on the right side accounts for bimolecular radiative recombination and the last term is due to Auger recombination. Both the introduction of the Auger term and the ASE-induced saturation are crucial to obtain

good agreement between experiments and modelling over a wide range of SOA bias currents [71].

β_{eff} is defined as the ratio of spontaneous emission coupled into the waveguide in one direction to the total spontaneous emission. β_{eff} is derived as follows

$$\beta_{eff}(n) = \frac{\int_{\lambda_0}^{\lambda_{gap}} 2\rho_{sp}(\lambda, n)\frac{hc^2}{\lambda^3}d\lambda}{R_{sp}(n)\frac{hc}{\lambda_{ase}}\sigma} \quad \text{A.26}$$

where ρ_{sp} is the radiative recombination spectral density coupled into the waveguide and the numerical evaluation of the integral is from a wavelength λ_0 where spontaneous emission is negligible to the wavelength of the bandgap λ_{gap}. As highlighted in [70] the variation of β_{eff} with the carrier concentration is small and thus in the model it is approximated by a constant. The effective gain g_{ase} is defined as

$$g_{ase}(n) = \frac{\int_{\lambda_0}^{\lambda_{gap}} g(\lambda, n)(\overline{W_{ase}^{+}} + \overline{W_{ase}^{-}})d\lambda}{\int_{\lambda_0}^{\lambda_{gap}} (\overline{W_{ase}^{+}} + \overline{W_{ase}^{-}})d\lambda} \quad \text{A.27}$$

where $\overline{W_{ase}^{+}}$ and $\overline{W_{ase}^{-}}$ are the average power density of the forward and backward propagating ASE under the assumption of constant carrier concentration inside the device. The integral in Equation A.27 is evaluated from λ_0 to λ_{gap} as in the calculation of β_{eff}.

The modal gain of the device is modelled using the following expression [70]

$$g(\lambda, n) = a_1(n - n_0)\left\{1 - \left[\frac{\frac{c}{\lambda} - \frac{c}{\lambda_{gap}}}{C_v(n - n_0)} - 1\right]^2\right\} \quad \text{A.28}$$

where n_0 is the model transparency density, λ_{gap} is the model bandgap wavelength, a_1 is the gain coefficient and C_v is a parameter related to the bandwidth of the modal gain. Because of the linear dependence of the carrier concentration shown by g_{ase}, in the simulation we modelled it using the relation

$$g_{ase}(n) = a_{ase}(n - n_{0,ase}) \quad \text{A.29}$$

with the parameters a_{ase} and $n_{0,ase}$ fitted to the gain calculated from Equation A.27

The EAM is assumed to be linear in the operation region of interest and it is modelled as a loss, dependent on the driving voltage. The wavelength dependence of the absorption is also neglected for simplicity. Despite these simplifications the overall R-EAM-SOA model provides results in extremely good agreement with the characteristics derived experimentally over a wide range of conditions, proving that the assumptions made are valid. The internal loss between SOA and R-EAM is modelled as a constant loss with no power or wavelength dependence. For ease of numerical realisation the loss is lumped together with the EAM insertion loss.

The SOA coupling losses are also taken into account both for the input/output port and the internal port in the case of R-EAM-SOA emulated with discrete components. The numerical realisation also takes into account the time delay that could be introduced between SOA and R-EAM section, for example by the fibre pigtails of the discrete components as described Chapter 4. In the numerical implementation the SOA has been partitioned into seven sections, which is a good compromise between accuracy and simulation speed. Details of parameter values used in the numerical model for both R-EAM-SOA analysed are given in Chapter 4 (Table 4.1). It is important to note that the parameters used in the modelling of the discrete R-EAM-SOA were all derived from the characterization of the discrete components. In the case of the integrated device, on the other hand, most of the parameters could not be measured directly and were either derived from scaling of parameters of discrete devices with similar design or by fitting with the experimental measurements.

LIST OF ACRONYMS

ADSL	Asymmetric digital subscriber line
AE	Active Ethernet
APD	Avalanche photodiode
ASE	Amplified spontaneous emission
AWG	Arrayed wave-guide grating
BERT	Bit error rate tester
BMRx	Burst mode receiver
CB	Carrier backscattering
CW	Continuous wave
CWDM	Coarse wavelength division multiplexing
DB	Duobinary
DFB	Distributed feedback laser
DML	Directly modulated laser
DSL	Digital subscriber line
DWDM	Dense wavelength division multiplexing
EAM	Electroabsorption modulator
EDFA	Erbium doped fibre amplifier
FP	Fabry-Perot
FTTB	Fibre to the building
FTTC	Fibre to the curb
FTTH	Fibre to the home
ISI	Inter-symbol-interference

LPF	Low pass filter
MFL	Multi-frequency laser
MZM	Mach-Zehnder modulator
NRZ	Non-return to zero
O/E/O	Optical/electrical/optical
ODN	Optical distribution network
OLT	Optical line termination
ONU	Optical network unit
OSNR	Optical signal to noise ratio
PIC	Photonic integrated circuit
PON	Passive optical network
PPG	Pulse pattern generator
PRBS	Pseudo-random binary sequence
RB	Rayleigh backscattering
R-EAM	Reflective electroabsorption modulator
ROADM	Reconfigurable optical add and drop multiplexer
R-SOA	Reflective semiconductor optical amplifier
SB	Signal backscattering
SBS	Stimulated Brillion scattering
SN	Service node
SNR	Signal to noise ratio
SOA	Semiconductor optical amplifier
SRS	Stimulated Raman scattering
SSMF	Standard single mode fibre
TDM	Time division multeplexing

TDMA	Time division multiple access
VDSL	Very high speed digital subscriber line
VOA	Variable optical attenuator
WDM	Wavelength division multiplexing

LIST OF PUBLICATIONS

JOURNAL PUBLICATIONS

[J1] P. Ossieur, C. Antony, A. M. Clarke, **A. Naughton**, H. G. Krimmel, Y. Chang*, et al.*, "A 135-km 8192-Split Carrier Distributed DWDM-TDMA PON With With 2 x 32 x 10 Gb/s Capacity," *Lightwave Technology, Journal of,* vol. 29, pp. 463-474, 2011.

[J2] P. Ossieur, C. Antony, **A. Naughton**, A. M. Clarke, H.-G. Krimmel, X. Yin*, et al.*, "Demonstration of a 32 × 512 Split, 100 km Reach, 2 × 32 × 10 Gb/s Hybrid DWDM-TDMA PON Using Tunable External Cavity Lasers in the ONUs," *Journal of Lightwave Technology,* vol. 29, pp. 3705-3718, 2011/12/15 2011.

[J3] **A. Naughton**, C. Antony, P. Ossieur, S. Porto, G. Talli, and P. D. Townsend, "Optimisation of SOA-REAMs for Hybrid DWDM-TDMA PON Applications," *Optics Express,* vol. 19, pp. B722-B727, 2011/12/12 2011.

[J4] C. P. Lai, **A. Naughton**, P. Ossieur, C. Antony, D. W. Smith, A. Borghesani*, et al.*, "Demonstration of error-free 25Gb/s duobinary transmission using a colourless reflective integrated modulator," *Optics Express,* vol. 21, pp. 500-507, 2013/01/14 2013.

[J5] G. Talli, **A. Naughton**, S. Porto, C. Antony, P. Ossieur, and P. D. Townsend, "Advantageous Effects of Gain Saturation in Semiconductor Optical Amplifier-Based Integrated Reflective Modulators," *Lightwave Technology, Journal of,* vol. 32, pp. 392-401, 2014.

[J6] **A. Naughton**, G. Talli, S. Porto, C. Antony, P. Ossieur, and P. D. Townsend, "Design Optimization of R-EAM-SOA for Long-Reach Carrier-Distributed Passive Optical Networks," Submitted to Journal of Lightwave Technology Feb 2014.

CONFERENCE PUBLICATIONS

[C1] P. Townsend, P. Ossieur, C. Antony, **A. Naughton**, A. M. Clarke, R. P. Davey, *et al.*, "European Research Project PIEMAN," in *Advanced Photonics & Renewable Energy*, Karlsruhe, 2010, p. AWA1.

[C2] P. Ossieur, C. Antony, **A. Naughton**, A. Clarke, P. D. Townsend, H.-G. Krimmel, *et al.*, "A Symmetric 320Gb/s Capable, 100km Extended Reach Hybrid DWDM-TDMA PON," in *National Fiber Optic Engineers Conference*, San Diego, California, 2010, p. NWB1.

[C3] **A. Naughton**, C. Antony, P. Ossieur, S. Porto, G. Talli, and P. D. Townsend, "Optimisation of SOA-REAMs for Hybrid DWDM-TDMA PON Applications," in *Photonics Ireland,* Dublin, Ireland, 2011.

[C4] **A. Naughton**, C. Antony, P. Ossieur, S. Porto, G. Talli, and P. D. Townsend, "Optimisation of SOA-REAMs for Hybrid DWDM-TDMA PON Applications," in *37th European Conference and Exposition on Optical Communications*, Geneva, 2011, p. Mo.1.C.4.

[C5] P. Ossieur, C. Antony, **A. Naughton**, S. Porto, N. A. Quadir, A. Clarke, *et al.*, "Hybrid DWDM-TDMA PONs for Next Generation Access," in *Optical Fiber Communication Conference*, Los Angeles, California, 2012, p. OW1B.7.

[C6] I. Cano, S. Porto, **A. Naughton**, P. Ossieur, P. D. Townsend, J. A. Lazaro, *et al.*, "Upstream performance improvement of low cost 10Gb/s ONUs with centralized OLT equalizer and FEC," in *Transparent Optical Networks (ICTON), 2012 14th International Conference on*, 2012, pp. 1-3.

[C7] C. P. Lai, **A. Naughton**, P. Ossieur, D. W. Smith, A. Borghesani, D. G. Moodie, *et al.*, "Low-power colourless reflective components for energy-efficient optical networks," in *Transparent Optical Networks (ICTON), 2012 14th International Conference on*, 2012, pp. 1-4.

[C8] **A. Naughton**, P. Ossieur, C. Antony, D. W. Smith, A. Borghesani, D. G. Moodie*, et al.*, "Error-free 10Gb/s duobinary transmission over 215km of SSMF using a hybrid photonic integrated reflective modulator," in *Optical Fiber Communication Conference and Exposition (OFC/NFOEC), 2012 and the National Fiber Optic Engineers Conference*, 2012, pp. 1-3.

[C9] **A. Naughton**, P. Ossieur, C. Antony, D. W. Smith, A. Borghesani, D. G. Moodie*, et al.*, "Error-free 10Gb/s duobinary transmission over 215km of SSMF using a hybrid photonic integrated reflective modulator," in *Optical Fiber Communication Conference and Exposition (OFC/NFOEC), 2012 and the National Fiber Optic Engineers Conference*, 2012, pp. 1-3.

[C10] C. P. Lai, **A. Naughton**, P. Ossieur, C. Antony, D. Smith, A. Borghesani*, et al.*, "Demonstration of Error-Free 25Gb/s Duobinary Transmission using a Colourless Reflective Integrated Modulator," in *European Conference and Exhibition on Optical Communication*, Amsterdam, 2012, p. We.1.E.4.

[C11] C. P. Lai, R. Vaernewyck, **A. Naughton**, J. Bauwelinck, X. Yin, X. Z. Qiu*, et al.*, "Multi-channel 11.3-Gb/s integrated reflective transmitter for WDM-PON," in *Optical Communication (ECOC 2013), 39th European Conference and Exhibition on*, 2013, pp. 1-3.

POSTERS

[P1] **A. Naughton**, P. Ossieur, D. Smith, L. Lealman, X. Chen, C. Ford, R. Cronin, A. Borghesani, R. Wyatt, A. Poustie and P. D. Townsend, "10Gb/s Transmission using a Novel Colourless Reflective Modulator," in *Photonics Ireland,* Kinsale, Cork, Ireland, 2009.

[P2] **A. Naughton**, G. Talli, P. Ossieur, C. Antony, S. Porto, and P. D. Townsend, "R-EAM-SOA Modelling for Carrier Distributed PON," in *Photonics Ireland,* Belfast, Ireland, 2013.

BIBLIOGRAPHY

[1] "http://www.itu.int/en/ITU-D/Statistics/Pages/stat/default.aspx."

[2] K. C. Kao and G. A. Hockham, "Dielectric-fibre surface waveguides for optical frequencies," *Optoelectronics, IEE Proceedings J,* vol. 133, pp. 191-198, 1986.

[3] "www.youtube.com."

[4] "www.netflix.com."

[5] "Gigabit - capable passive optical networks (GPON)," *ITU-T G984,* Mar, 2003.

[6] R. Davey, D. Payne, P. Barker, K. Smith, M. Wilkinson, and P. Gunning, "Designing a 21st and 22nd century fibre broadband access network," *BT Technology Journal,* vol. 24, pp. 57-64, 2006/04/01 2006.

[7] Nicholas J. Frigo, Patrick P. Iannone, and K. C. Reichmann, "A View of Fiber to the Home Economics," *Communications Magazine, IEEE, ,* vol. vol. 42,.

[8] D. B. Payne and R. P. Davey, "The future of fibre access systems?," *BT Technology Journal,* vol. 20, pp. 104-114, 2002/10/01 2002.

[9] R. P. Davey, D. B. Grossman, M. Rasztovits-Wiech, D. Payne, D. Nesset, A. E. Kelly, A. Rafel, S. Appathurai, and Y. Sheng-Hui, "Long-Reach Passive Optical Networks," *Lightwave Technology, Journal of,* vol. 27, pp. 273-291, 2009.

[10] G. Talli and P. D. Townsend, "Hybrid DWDM-TDM long-reach PON for next-generation optical access," *Lightwave Technology, Journal of,* vol. 24, pp. 2827-2834, 2006.

[11] P. Ossieur, C. Antony, A. Naughton, A. M. Clarke, H.-G. Krimmel, X. Yin, X.-Z. Qiu, C. Ford, A. Borghesani, D. Moodie, A. Poustie, R. Wyatt, B. Harmon, I. Lealman, G. Maxwell, D. Rogers, D. W. Smith, S. Smolorz, H. Rohde, D.

Nesset, R. P. Davey, and P. D. Townsend, "Demonstration of a 32 × 512 Split, 100 km Reach, 2 × 32 × 10 Gb/s Hybrid DWDM-TDMA PON Using Tunable External Cavity Lasers in the ONUs," *Journal of Lightwave Technology,* vol. 29, pp. 3705-3718, 2011/12/15 2011.

[12] E. K. MacHale, G. Talli, P. D. Townsend, A. Borghesani, I. Lealman, D. G. Moodie, and D. W. Smith, "Extended-reach PON employing 10Gb/s integrated reflective EAM-SOA," in *Optical Communication, 2008. ECOC 2008. 34th European Conference on*, 2008, pp. 1-1.

[13] P. Ossieur, C. Antony, A. M. Clarke, A. Naughton, H. G. Krimmel, Y. Chang, C. Ford, A. Borghesani, D. Moodie, A. Poustie, R. Wyatt, B. Harmon, I. Lealman, G. Maxwell, D. Rogers, D. W. Smith, D. Nesset, R. P. Davey, and P. D. Townsend, "A 135-km 8192-Split Carrier Distributed DWDM-TDMA PON With With 2 x 32 x 10 Gb/s Capacity," *Lightwave Technology, Journal of,* vol. 29, pp. 463-474, 2011.

[14] D. Smith, I. Lealman, X. Chen, D. Moodie, P. Cannard, J. Dosanjh, L. Rivers, C. Ford, R. Cronin, T. Kerr, L. Johnston, R. Waller, R. Firth, A. Borghesani, R. Wyatt, and A. Poustie, "Colourless 10Gb/s reflective SOA-EAM with low polarization sensitivity for long-reach DWDM-PON networks," in *Optical Communication, 2009. ECOC '09. 35th European Conference on*, 2009, pp. 1-2.

[15] I. T. Monroy, F. Ohman, K. Yvind, R. Kjaer, C. Peucheret, A. M. J. Koonen, and P. Jeppesen, "85 km Long Reach PON System Using a Reflective SOA-EA Modulator and Distributed Raman Fiber Amplification," in *Lasers and Electro-Optics Society, 2006. LEOS 2006. 19th Annual Meeting of the IEEE*, 2006, pp. 705-706.

[16] C. Antony, P. Ossieur, A. M. Clarke, A. Naughton, H. G. Krimmel, Y. Chang, A. Borghesani, D. Moodie, A. Poustie, R. Wyatt, B. Harmon, I. Lealman, G. Maxwell, D. Rogers, D. W. Smith, D. Nesset, R. P. Davey, and P. D. Townsend, "Demonstration of a carrier distributed, 8192-split hybrid DWDM-TDMA PON over 124km field-installed fibers," in *Optical Fiber Communication (OFC), collocated National Fiber Optic Engineers Conference, 2010 Conference on (OFC/NFOEC)*, 2010, pp. 1-3.

[17] A. Naughton, C. Antony, P. Ossieur, S. Porto, G. Talli, and P. D. Townsend, "Optimisation of SOA-REAMs for Hybrid DWDM-TDMA PON Applications," *Optics Express,* vol. 19, pp. B722-B727, 2011/12/12 2011.

[18] G. Talli, A. Naughton, S. Porto, C. Antony, P. Ossieur, and P. D. Townsend, "Advantageous Effects of Gain Saturation in Semiconductor Optical Amplifier-Based Integrated Reflective Modulators," *Lightwave Technology, Journal of,* vol. 32, pp. 392-401, 2014.

[19] "http://www.greenc3po.eu/."

[20] A. Naughton, P. Ossieur, C. Antony, D. W. Smith, A. Borghesani, D. G. Moodie, G. Maxwell, P. Healey, and P. D. Townsend, "Error-free 10Gb/s duobinary transmission over 215km of SSMF using a hybrid photonic integrated reflective modulator," in *Optical Fiber Communication Conference and Exposition (OFC/NFOEC), 2012 and the National Fiber Optic Engineers Conference*, 2012, pp. 1-3.

[21] C. P. Lai, A. Naughton, P. Ossieur, C. Antony, D. W. Smith, A. Borghesani, D. G. Moodie, G. Maxwell, P. Healey, A. Poustie, and P. D. Townsend, "Demonstration of error-free 25Gb/s duobinary transmission using a colourless reflective integrated modulator," *Optics Express,* vol. 21, pp. 500-507, 2013/01/14 2013.

[22] P. J. Winzer and R. Essiambre, "Advanced Optical Modulation Formats," *Proceedings of the IEEE,* vol. 94, pp. 952-985, 2006.

[23] R. Davey, J. Kani, F. Bourgart, and K. McCammon, "Options for future optical access networks," *Communications Magazine, IEEE,* vol. 44, pp. 50-56, 2006.

[24] "Gigabit Ethernet Passive Optical Networks (GE-PON)," *IEEE P802.3ah,* 2004.

[25] "10-Gigabit-capable passive optical networks (XG-PON)," *ITU-T G.987,* 2010.

[26] "10 Gigabit Ethernet Passive Optical Networks (10G-EPON)," *IEEE P802.3av,* 2009.

[27] "Broadband optical access systems based on Passive Optical Networks (PON)," *ITU-T G.983 1998*

[28] "Spectral grids for WDM applications: CWDM wavelength grid," *ITU-T G.694.2*

[29] A. Banerjee, Y. Park, F. Clarke, H. Song, S. Yang, G. Kramer, K. Kim, and B. Mukherjee, "Wavelength-division-multiplexed passive optical network (WDM-PON) technologies for broadband access: a review [Invited]," *Journal of Optical Networking,* vol. 4, pp. 737-758, 2005/11/01 2005.

[30] "Spectral grids for WDM applications: DWDM frequency grid " *ITU-T G.694.1*.

[31] F.-T. An, K. Kyeong Soo, D. Gutierrez, S. Yam, E. Hu, K. Shrikhande, and L. G. Kazovsky, "SUCCESS: a next-generation hybrid WDM/TDM optical access network architecture," *Lightwave Technology, Journal of,* vol. 22, pp. 2557-2569, 2004.

[32] C. Bock, J. Prat, and S. D. Walker, "Hybrid WDM/TDM PON using the AWG FSR and featuring centralized light generation and dynamic bandwidth allocation," *Lightwave Technology, Journal of,* vol. 23, pp. 3981-3988, 2005.

[33] "http://www.ist-pieman.org/about.htm."

[34] G. Talli and P. D. Townsend, "Feasibility Demonstration of 100km Reach DWDM SuperPON with Upstream Bit Rates of 2.5Gb/s and 10Gb/s," in *Optical Fiber Communication Conference and Exposition and The National Fiber Optic Engineers Conference*, Anaheim, California, 2005, p. OFI1.

[35] "GPON reach extension " *ITU-T G.984.6,* 2008.

[36] G. Talli and P. D. Townsend, "Hybrid DWDM-TDM Long-Reach PON for Next-Generation Optical Access," *Journal of Lightwave Technology,* vol. 24, p. 2827, 2006/07/01 2006.

[37] R. D. Feldman, "Crosstalk and loss in wavelength division multiplexed systems employing spectral slicing," *Lightwave Technology, Journal of,* vol. 15, pp. 1823-1831, 1997.

[38] K. H. Han, E. S. Son, H. Y. Choi, K. W. Lim, and Y. C. Chung, "Bidirectional WDM PON using light-emitting diodes spectrum-sliced with cyclic arrayed-waveguide grating," *Photonics Technology Letters, IEEE,* vol. 16, pp. 2380-2382, 2004.

[39] P. Healey, P. Townsend, C. Ford, L. Johnston, P. Townley, I. Lealman, L. Rivers, S. Perrin, and R. Moore, "Spectral slicing WDM-PON using wavelength-seeded reflective SOAs," *Electronics Letters,* vol. 37, pp. 1181-1182, 2001.

[40] S. B. Park, D. K. Jung, D. J. Shin, H. S. Shin, I. K. Yun, J. S. Lee, Y. K. Oh, and Y. J. Oh, "Demonstration of WDM-PON with 50 GHz channel spacing employing spectrum-sliced reflective semiconductor optical amplifiers," *Electronics Letters,* vol. 42, pp. 1172-1173, 2006.

[41] P. Soo-Jin, L. Chang-Hee, J. Ki-Tae, P. Hyung-Jin, A. Jeong-Gyun, and S. Kil-Ho, "Fiber-to-the-home services based on wavelength-division-multiplexing passive optical network," *Lightwave Technology, Journal of,* vol. 22, pp. 2582-2591, 2004.

[42] S. Dong-Jae, J. Dae Kwang, S. Hong Seok, K. Jin Wook, H. Seongtaek, O. Yunje, and C. Shim, "Hybrid WDM/TDM-PON with wavelength-selection-free transmitters," *Lightwave Technology, Journal of,* vol. 23, pp. 187-195, 2005.

[43] L. Y. Chan, C. K. Chan, T. K. Tong, F. Tong, and L. K. Chen, "Upstream traffic transmitter using injection-locked Fabry-Perot laser diode as modulator for WDM access networks," *Electronics Letters,* vol. 38, pp. 43-45, 2002.

[44] K. Iwatsuki, K. Jun-ichi, H. Suzuki, and M. Fujiwara, "Access and metro networks based on WDM technologies," *Lightwave Technology, Journal of,* vol. 22, pp. 2623-2630, 2004.

[45] C. W. Chow, C. H. Yeh, C. H. Wang, F. Y. Shih, and S. Chi, "Signal remodulation high split-ratio hybrid WDM-TDM PONs using RSOA-based ONUs," *Electronics Letters,* vol. 45, pp. 903-905, 2009.

[46] A. Garreau, C. Kazmierski, D. Chiaroni, M. Le Pallec, J. Decobert, J. Landreau, D. Carpentier, and J. Provost, "10 Gbit/s drop and continue colorless operation of a 1.5µm AlGaInAs reflective amplified electroabsorption modulator," in *Optical Communications, 2006. ECOC 2006. European Conference on*, 2006, pp. 1-2.

[47] G. P. Agrawal, "Fiber-optic communication systems," Third Edition, 2002.

[48] R. K. Staubli and P. Gysel, "Crosstalk penalities due to coherent Rayleigh noise in bidirectional optical communication systems," *Lightwave Technology, Journal of,* vol. 9, pp. 375-380, 1991.

[49] G. Talli, D. Cotter, and P. D. Townsend, "Rayleigh backscattering impairments in access networks with centralised light source," *Electronics Letters,* vol. 42, pp. 877-878, 2006.

[50] E. K. MacHale, G. Talli, C. W. Chow, and P. D. Townsend, "Reduction of Signal-Induced Rayleigh Noise in a 10Gb/s WDM-PON using a Gain-Saturated SOA," in *Optical Communication (ECOC), 2007 33rd European Conference and Ehxibition of*, 2007, pp. 1-2.

[51] C. W. Chow, G. Talli, and P. D. Townsend, "Rayleigh Noise Reduction in 10-Gb/s DWDM-PONs by Wavelength Detuning and Phase-Modulation-Induced Spectral Broadening," *Photonics Technology Letters, IEEE,* vol. 19, pp. 423-425, 2007.

[52] C. W. Chow, G. Talli, A. D. Ellis, and P. D. Townsend, "Rayleigh noise mitigation in DWDM LR-PONs using carrier suppressed subcarrier-amplitude modulated phase shift keying," *Optics Express,* vol. 16, pp. 1860-1866, 2008/02/04 2008.

[53] G. P. Agrawal, "Nonlinear Fiber Optics," *USA: Elsevier Inc,* 2007.

[54] D. Cotter, "Transient stimulated Brillouin scattering in long single-mode fibres," *Electronics Letters,* vol. 18, pp. 504-506, 1982.

[55] J. M. Senior, "Optical Fiber Communications Principals and Practice," Third Edition, 2009.

[56] I. P. Kaminov, T. Li, and A. E. Willner, "Optical Fiber Telecommunications," Fifth Edition, 2008.

[57] P. C. Becker, "Erbium-Doped Fiber Amplifiers, Fundamentals and Technology," *New York: Academic Press,* 1999.

[58] S. B. Poole, D. N. Payne, R. J. Mears, M. E. Fermann, and R. Laming, "Fabrication and characterization of low-loss optical fibers containing rare-earth ions," *Lightwave Technology, Journal of,* vol. 4, pp. 870-876, 1986.

[59] B. J. Ainslie, "A review of the fabrication and properties of erbium-doped fibers for optical amplifiers," *Lightwave Technology, Journal of,* vol. 9, pp. 220-227, 1991.

[60] G. P. Agrawal, "Lightwave Technologies: Telecommunication Systems," 2005.

[61] H. Nyquist, "Thermal Agitation of Electric Charge in Conductors," *Physical Review,* vol. 32, pp. 110-113, 07/01/ 1928.

[62] Y. Yamamoto and K. Inoue, "Noise in amplifiers," *Lightwave Technology, Journal of,* vol. 21, pp. 2895-2915, 2003.

[63] N. A. Olsson, "Lightwave systems with optical amplifiers," *Lightwave Technology, Journal of,* vol. 7, pp. 1071-1082, 1989.

[64] P. J. Winzer, M. Pfennigbauer, M. M. Strasser, and W. R. Leeb, "Optimum filter bandwidths for optically preamplified NRZ receivers," *Lightwave Technology, Journal of,* vol. 19, pp. 1263-1273, 2001.

[65] N. S. Bergano, F. W. Kerfoot, and C. R. Davidsion, "Margin measurements in optical amplifier system," *Photonics Technology Letters, IEEE,* vol. 5, pp. 304-306, 1993.

[66] R.-J. Essiambre, P. J. Winzer, and D. F. Grosz, "Impact of DCF properties on system design," *Journal of Optical and Fiber Communications Reports,* vol. 3, pp. 221-291, 2006/08/01 2006.

[67] M. J. Connelly, "Semiconductor optical Amplifiers," 2002.

[68] R. Bonk, "Linear and Nonlinear Semiconductor Optical Amplifiers for Next-Generation Optical Networks."

[69] W. G. Driscoll, "Handbook of Optics," Third Edition, 1978.

[70] G. Talli and M. J. Adams, "Gain dynamics of semiconductor optical amplifiers and three-wavelength devices," *Quantum Electronics, IEEE Journal of,* vol. 39, pp. 1305-1313, 2003.

[71] R. Giller, R. J. Manning, G. Talli, R. P. Webb, and M. J. Adams, "Analysis of the dimensional dependence of semiconductor optical amplifier recovery speeds," *Optics Express,* vol. 15, pp. 1773-1782, 2007/02/19 2007.

[72] F. Koyama, T. Yamatoya, and K. Iga, "Noise suppression and intensity modulation using gain-saturated semiconductor optical amplifier," in *Optical Amplifiers and Their Applications*, Québec, Canada, 2000, p. OMD12.

[73] K. Sato and H. Toba, "Reduction of mode partition noise by using semiconductor optical amplifiers," in *Semiconductor Laser Conference, 2000. Conference Digest. 2000 IEEE 17th International*, 2000, pp. 73-74.

[74] A. Mecozzi, "Small-signal theory of wavelength converters based on cross-gain modulation in semiconductor optical amplifiers," *Photonics Technology Letters, IEEE,* vol. 8, pp. 1471-1473, 1996.

[75] G. L. Li and P. K. L. Yu, "Optical intensity modulators for digital and analog applications," *Lightwave Technology, Journal of,* vol. 21, pp. 2010-2030, 2003.

[76] S. Ó. Dúill, L. Marazzi, P. Parolari, R. Brenot, C. Koos, W. Freude, and J. Leuthold, "Efficient modulation cancellation using reflective SOAs," *Optics Express,* vol. 20, pp. B587-B594, 2012/12/10 2012.

[77] J. M. Casperson, F. G. Moore, and L. W. Casperson, "Double-pass high-gain laser amplifiers," *Journal of Applied Physics,* vol. 86, pp. 2967-2973, 1999.

[78] L. W. Casperson and J. M. Casperson, "Power self-regulation in double-pass high-gain laser amplifiers," *Journal of Applied Physics,* vol. 87, pp. 2079-2083, 2000.

[79] Y. Boucher and A. Sharaiha, "Spectral properties of amplified spontaneous emission in semiconductor optical amplifiers," *Quantum Electronics, IEEE Journal of,* vol. 36, pp. 708-720, 2000.

[80] M. J. Adams, J. V. Collins, and I. D. Henning, "Analysis of semiconductor laser optical amplifiers," *Optoelectronics, IEE Proceedings J,* vol. 132, pp. 58-63, 1985.

[81] R. Gutierrez-Castrejon, L. Schares, L. Occhi, and G. Guekos, "Modeling and measurement of longitudinal gain dynamics in saturated semiconductor optical amplifiers of different length," *Quantum Electronics, IEEE Journal of,* vol. 36, pp. 1476-1484, 2000.

[82] J. L. Pleumeekers, M. A. Dupertuis, T. Hessler, P. E. Selbmann, S. Haacke, and B. Deveaud, "Longitudinal spatial hole burning and associated nonlinear gain in gain-clamped semiconductor optical amplifiers," *Quantum Electronics, IEEE Journal of,* vol. 34, pp. 879-886, 1998.

[83] F. Ginovart, J. C. Simon, and I. Valiente, "Gain recovery dynamics in semiconductor optical amplifier," *Optics Communications,* vol. 199, pp. 111-115, 11/15/ 2001.

[84] A. Reale, A. Di Carlo, and P. Lugli, "Gain dynamics in traveling-wave semiconductor optical amplifiers," *Selected Topics in Quantum Electronics, IEEE Journal of,* vol. 7, pp. 293-299, 2001.

[85] E. K. MacHale, G. Talli, P. D. Townsend, A. Borghesani, I. Lealman, D. G. Moodie, and D. W. Smith, "Signal-induced rayleigh noise reduction using gain saturation in an integrated R-EAM-SOA," in *Optical Fiber Communication - incudes post deadline papers, 2009. OFC 2009. Conference on*, 2009, pp. 1-3.

[86] G. Talli and M. J. Adams, "Amplified spontaneous emission in semiconductor optical amplifiers: modelling and experiments," *Optics Communications,* vol. 218, pp. 161-166, 3/15/ 2003.

[87] V. Photonics, "http://www.vpiphotonics.com/TMOpticalSystems.php."

[88] C. J. Anderson and J. A. Lyle, "Technique for evaluating system performance using Q in numerical simulations exhibiting intersymbol interference," *Electronics Letters,* vol. 30, pp. 71-72, 1994.

[89] P. Ossieur, N. A. Quadir, S. Porto, M. Rensing, C. Antony, W. Han, P. O?Brien, Y. Chang, and P. D. Townsend, "A 10G linear burst-mode receiver supporting electronic dispersion compensation for extended-reach optical links," *Optics Express,* vol. 19, pp. B604-B610, 2011/12/12 2011.

[90] P. D. Townsend, A. Clarke, P. Ossieur, D. W. Smith, A. Borghesani, D. G. Moodie, I. F. Lealman, X. Z. Qiu, J. Bauwelinck, X. Yin, K. Grobe, B. T. Teipen, R. Jensen, N. Parsons, and E. Kehayas, "Towards colourless coolerless components for low power optical networks," in *Optical Communication (ECOC), 2011 37th European Conference and Exhibition on*, 2011, pp. 1-3.

[91] A. M. Clarke, A. Borghesani, D. W. Smith, P. Ossieur, P. D. Townsend, R. Jensen, and N. Parsons, "Demonstration of wavelength agile metro node using reflective colorless components," in *Optical Fiber Communication Conference and Exposition (OFC/NFOEC), 2011 and the National Fiber Optic Engineers Conference*, 2011, pp. 1-3.

[92] R. Jensen, A. Lord, and N. Parsons, "Colourless, directionless, contentionless ROADM architecture using low-loss optical matrix switches," in *Optical Communication (ECOC), 2010 36th European Conference and Exhibition on*, 2010, pp. 1-3.

[93] D. G. Moodie, D. C. Rogers, P. J. Cannard, A. Borghesani, C. W. Ford, R. Firth, R. Cronin, M. J. Robertson, D. W. Smith, L. Ponnampalam, C. Renaud, A. J. Seeds, M. Thakur, T. Quinlan, and S. Walker, "Photodiodes and reflective electroabsorption modulators for mm-wave and UWB applications," *in Proc. European Workshop on Photonic Solutions for Wireless, Access, and in-House Networks, Duisburg, Germany, May 2009*.

[94] J. Prokais, "Digital Communications," Fifth Edition, 2007.

[95] W. Kaiser, T. Wuth, M. Wichers, and W. Rosenkranz, "Reduced complexity optical duobinary 10-Gb/s transmitter setup resulting in an increased transmission distance," *Photonics Technology Letters, IEEE,* vol. 13, pp. 884-886, 2001.

[96] D. Penninckx, M. Chbat, L. Pierre, and J. P. Thiery, "The phase-shaped binary transmission (PSBT): a new technique to transmit far beyond the chromatic dispersion limit," *Photonics Technology Letters, IEEE,* vol. 9, pp. 259-261, 1997.

[97] K. Hoon and C. X. Yu, "Optical duobinary transmission system featuring improved receiver sensitivity and reduced optical bandwidth," *Photonics Technology Letters, IEEE,* vol. 14, pp. 1205-1207, 2002.

[98] S. Walklin and J. Conradi, "On the relationship between chromatic dispersion and transmitter filter response in duobinary optical communication systems," *Photonics Technology Letters, IEEE,* vol. 9, pp. 1005-1007, 1997.

[99] I. Kang, S. Chandrasekhar, C. Kazmierski, M. Rasras, and N. Dupuis, "1650-km Transmission of 50-Gb/s NRZ and RZ-DQPSK Signals Generated Using an Electroabsorption Modulators-Silica Planar Lightwave Circuit Hybrid Integrated Device," in *Optical Fiber Communication Conference*, San Diego, California, 2010, p. OMJ4.